

BIO-INSPIRED WINGS IN HIGH FRESTREAM TURBULENCE:
A NUMERICAL AND EXPERIMENTAL STUDY

A Thesis

by

ALEXIA MARTINEZ IBARRA

Submitted to the Graduate College of
The University of Texas Rio Grande Valley
In partial fulfillment of the requirements for the degree of

MASTER OF SCIENCE IN ENGINEERING

May 2020

Major Subject: Mechanical Engineering

BIO-INSPIRED WINGS IN HIGH FRESTREAM TURBULENCE:
A NUMERICAL AND EXPERIMENTAL STUDY

A Thesis
by
ALEXIA MARTINEZ IBARRA

COMMITTEE MEMBERS

Dr. Isaac Choutapalli
Chair of Committee

Dr. Robert Freeman
Committee Member

Dr. Horacio Vasquez
Committee Member

Dr. Stephen Crown
Committee Member

Mr. Gregorio Acosta
Committee Member

May 2020

Copyright 2020 Alexia Martinez Ibarra
All Rights Reserved

ABSTRACT

Martinez Ibarra, Alexia, Bio-inspired Wings in High Freestream Turbulence: A Numerical and Experimental Study. Master of Science in Engineering (MSE), May, 2020, 131 pp., 5 tables, 73 figures, references, 38 titles.

The aerodynamic and flow field characteristics of a NACA 0010 airfoil with leading-edge modifications were investigated in flow with freestream turbulence intensity of 4%. A set of 4 airfoils, each of them with different wavelengths (4, 8, 10, and 12 tubercles along the spanwise direction) was experimentally studied. An unmodified NACA 0010 airfoil was used as baseline. The Reynolds number was varied from 201,200 to 351,600. The angle of attack was varied within the range of -6 to 20 degrees. Several techniques were used to investigate the characteristics of airfoils such as wake profile surveys, 6-axis force measurements, and Particle Image Velocimetry (PIV). From the results, it was shown that increasing the freestream turbulence intensity changed primarily the drag behavior reported for leading-edge tubercles at lower turbulence intensity.

DEDICATION

I dedicate this work to God, my father, Luis R. Martinez Zapata, my mother, Rosa A. Ibarra Marquez, my sister, Andrea K., my brother, Luis R., and my husband, Miguel N. Saenz, for always cheering on my side even when far away, for believing I was capable of accomplishing the goals I set for myself, and for the endless demonstrations of support.

Without their patience and unconditional love, this work wouldn't have been possible.

ACKNOWLEDGEMENTS

I would like to acknowledge the never-ending support of Dr. Isaac M. Choutapalli, my committee chair. Thank you for the opportunity of being a part of your team and guiding me through this journey. I will always be grateful for all that I learned while being under your advice. I would also like to acknowledge the members of my committee. Thank you, not only for your support in this project but for all that you taught me and the opportunities you gave me throughout the years.

I would also like to acknowledge every member of the Aerodynamics and Propulsion Laboratory research group, for their participation and contribution to this work.

TABLE OF CONTENTS

	Page
ABSTRACT.....	iii
DEDICATION.....	iv
ACKNOWLEDGEMENTS.....	v
TABLE OF CONTENTS.....	vi
LIST OF TABLES.....	x
LIST OF FIGURES.....	xi
CHAPTER I. INTRODUCTION.....	1
Introduction.....	1
Background.....	1
Flow Control.....	1
Biomimetics.....	2
Humpback Whale and Tubercles as a PFC Device.....	5
Literature Review.....	8
Effects of Tubercles on the Aerodynamic Characteristics.....	9
Effects of Tubercle Configuration on the Aerodynamic Characteristics.....	13
Effects of Reynolds Number on the Aerodynamic Characteristics.....	18
Effects of Tubercles on Flow Field Characteristics of a Wing.....	20
Summary and Discussion.....	23
Motivation for the Thesis.....	25

Organization of Thesis	26
CHAPTER II. EXPERIMENTAL SETUP AND METHODOLOGY	27
Introduction.....	27
Wind Tunnel Facility	28
Airfoil Geometry.....	28
Airfoil Setup	30
Experimental Parameters	31
Experimental Instrumentation.....	31
Force Measurements	31
Calibration.....	32
Data Outlier Elimination.....	33
Hysteresis Error	34
Uncertainty in Force Measurements	35
Pressure Measurements.....	39
Uncertainty in Pressure Measurements.....	42
Temperature Measurements.....	43
Angle of Attack Variation.....	44
Particle Image Velocimetry	44
PIV Measurement Data.....	45
Data Acquisition	46
Experimental Setup.....	46
Data Analysis	49
Lift Coefficient.....	49
Drag Coefficient.....	50

Pressure Drag	51
Total Drag	52
CHAPTER III. SOURCE – VORTEX PANEL METHOD	57
Introduction.....	57
Procedure	59
Source Panel Method	59
Source – Vortex Panel Method	63
Implementation of Source – Vortex Panel Method Using MATLAB.....	69
Discretization of Geometry and Grid Generation	69
Influence Coefficients in Matrix Form	71
Establishing Right-Hand-Side of Equations in Vector Form	73
Solve Linear Algebraic Equations of the Form $Ma=b$	73
Calculations of Pressure and Loads	74
Sources and Vortex Strength	75
Surface Pressure Distribution	77
Lift Prediction	81
Conclusion	83
CHAPTER IV. RESULTS AND DISCUSSION.....	85
Introduction.....	85
Lift Measurements	85
Rake Measurements and Total Drag Calculations.....	92
Particle Image Velocimetry	109
Instantaneous PIV Images.....	110

Time-Averaged Velocity Fields.....	110
Time-Averaged Vorticity Fields	114
Turbulence Measurements	114
CHAPTER V. CONCLUSION AND FUTURE WORK	115
Drag Measurements	115
Lift Measurements	117
PIV Measurements.....	118
REFERENCES	120
APPENDIX A.....	123
APPENDIX B	128
BIOGRAPHICAL SKETCH	131

LIST OF TABLES

	Page
Table 1. Summary of effect of tubercle configuration on aerodynamic performance.....	24
Table 2. Summary of CAD models with leading-edge tubercles and identification label	
For airfoils with 6%c amplitude	29
Table 3. Stall angle and maximum lift coefficient due to variation in number of tubercles along the spanwise direction for a Reynolds number of 201,200.....	89
Table 4. State-of-the-art equipment	129
Table 5. State-of-the-art software	130

LIST OF FIGURES

	Page
Figure 1. Overview of various species and objects from living nature and their selected functions. Image via Bhushan, 2016.....	3
Figure 2. Humpback whale. Image via Tom Collins/Wildlife conservation	6
Figure 3. (a)Lift and (b)drag coefficient vs angle of attack for NACA 65-021.....	11
Figure 4. (a)Lift and (b)drag coefficient vs angle of attack for NACA 63-021.....	11
Figure 5. (a)Lift and (b)drag coefficient vs angle of attack for NACA 63-021.....	11
Figure 6. (a)Lift and (b)drag coefficient vs angle of attack for NACA 0020.....	12
Figure 7. Effect of amplitude variation on (a)lift and (b)drag coefficient for NACA 63-021 with 25% c wavelength. Image via Johari, 2007	14
Figure 8. Effect of amplitude variation on (a)lift and (b)drag coefficient for on NACA 0021 with 43% c wavelength. Image via Hansen, 2011	14
Figure 9. Effect of amplitude variation on (a)lift and(b) drag coefficient for NACA 63-021 with 25% c wavelength. Image via Custodio, 2015.....	14
Figure 10. Effect of λ variation on (a)lift and (b)drag coefficient for NACA 63-021 with 5% c A. Image via Johari, 2007	15
Figure 11. Effect of λ variation on (a)lift and (b)drag coefficient for NACA 0021 with various A. Image via Hansen, 2011	15
Figure 12. Effect of amplitude variation on (a)lift and (b)drag coefficient for NACA 63-021 with 50% c wavelength. Image via Custodio, 2015.....	15

Figure 13. Effect of Reynolds number on (a)lift and (b)drag coefficient for NACA 63-021 with 5%c A and 50%c λ	19
Figure 14. Normalized instantaneous streamwise vorticity for angle of attack.....	22
Figure 15. Wind tunnel facility at UTRGV – Edinburg	27
Figure 16. Continuation of wind tunnel facility at UTRGV – Edinburg.....	28
Figure 17. CAD models of (a)baseline airfoil and (b)leading-edge tubercles airfoil.	29
Figure 18. (a)Airfoil body and (b)interchangeable leading-edge	30
Figure 19. (1 of 2) Six-axis force/torque transducer.....	31
Figure 20. Force transducer calibration	32
Figure 21. Data outlier elimination performed on data set	33
Figure 22. Upscale and downscale sequential test – Hysteresis error	34
Figure 23. Data set with error bars for critical points	36
Figure 24. FFT results for force transducer (a) A and (b) B.....	37
Figure 25. (a) (1 of 2) OMEGA differential pressure transducer (b) OMEGA absolute pressure transducer and (c) 9116 pressure scanner.....	39
Figure 26. Stanford Research SR640 filter	40
Figure 27. (a) Pitot rake with capacity of six pitot tubes along the width of wind tunnel test section driven by (b) VELMEX bi-slide.....	40
Figure 28. (a) Display of test section conditions and (b) linear power supply (LPS) 304.....	41
Figure 29. OMEGA K-type thermocouple	41
Figure 30. Data set with error bars for critical points	42
Figure 31. (a) Rotary table and (b) ball bearing fixtures	43

Figure 32. Particle Image Velocimetry setup showing Nd:YAG laser, beam combiner and articulating arm	44
Figure 33. Particle Image Velocimetry setup showing laser sheet and CMOS cameras.....	45
Figure 34. Data acquisition using LabVIEW – (a)Pressure measurements and (b)force/torque measurements	47
Figure 35. Schematic of (a) pressure, force, and temperature and (b).....	48
Figure 36. Schematic with local and global axes utilized for force transducers.....	51
Figure 37. Control volume bounding an airfoil immersed in a fluid flow.....	52
Figure 38. Resultant force on control surface	53
Figure 39. Coordinate system in terms of Q	59
Figure 40. (a)Discretization of airfoil surface into panels and (b)tangent and normal unit vectors.....	60
Figure 41. Velocities on the upper and lower surface at the trailing edge	63
Figure 42. Coordinate system in terms of Q	64
Figure 43. Discretization of NACA 0010 airfoil with (a) 26 and (b) 100 panels	71
Figure 44. Vortex strength variation with angle of attack	75
Figure 45. Source strength distribution for NACA 0010 airfoil at various angles of attack	76
Figure 46. Pressure coefficient distribution on the upper and lower surface for a NACA 0010 airfoil at 0 degrees – Panel method	77
Figure 47. Effect of panel number on accuracy of results	78
Figure 48. Pressure coefficient distribution for NACA 0010 airfoil at various angles of attack.....	79

Figure 49. Pressure coefficient distribution for a NACA 0010 airfoil for all angles of attack.....	80
Figure 50. Variation of lift coefficient with angle of attack for a NACA 0010 airfoil – Panel method.....	81
Figure 51. Comparison between calculated and experimental results for NACA 0010 airfoil.....	82
Figure 52. Variation of lift coefficient with angle of attack for 8T and baseline at a Reynolds number of 201,200.....	86
Figure 53. Variation of lift coefficient with angle of attack for all models in comparison with the baseline at a Reynolds number of 201,200	88
Figure 54. Comparison in the variation of lift coefficient with angle of attack between 8T and the baseline for Reynolds number of (a)201,200, (b)246,100, (c)296,200, and (d)315,600.....	90
Figure 55. Comparison in the variation of (a)lift coefficient slope, (b)stall angle, and (c)maximum lift coefficient between 8T and the baseline for all Reynolds numbers tested	91
Figure 56. Baseline and 8T comparison of normalized wake velocity profiles for all angles of attack at a Reynolds number of 201,200	94
Figure 57. Variation of drag coefficient with angle of attack for 8T and baseline at a Reynolds number of 201,200.....	95
Figure 58. Variation of induced to total drag coefficient ratio with angle of attack for 8T and baseline at a Reynolds number of 201,200	96

Figure 59. Variation of lift to drag ratio with angle of attack for 8T and baseline at a Reynolds number of 201,200	98
Figure 60. Drag polar for 8T and baseline at a Reynolds number of 201,200.....	99
Figure 61. Normalized wake velocity profiles for all models in comparison with the baseline at 10 degrees at a Reynolds number of 201,200	101
Figure 62. Normalized wake velocity profiles for all models in comparison with the baseline at 18 degrees at a Reynolds number of 201,200	102
Figure 63. Variation of drag coefficient with angle of attack for all models in comparison with the baseline at a Reynolds number of 201,200	104
Figure 64. Variation of induced to total drag coefficient ratio with angle of attack for all models in comparison with the baseline at a Reynolds number of 201,200.....	104
Figure 65. Variation of lift-to-drag ratio with angle of attack for all models in comparison with the baseline at a Reynolds number of 201,200	105
Figure 66. Drag polar for all models at a Reynolds number of 201,200	106
Figure 67. Comparison in the variation of drag coefficient with angle of attack between 8T and the baseline for Reynolds number of (a)201,200, (b)246,100, (c)296,200, and (d)351,600	107
Figure 68. Comparison in the variation of minimum drag coefficient between 8T and the baseline for all Reynolds numbers tested.....	108
Figure 69. Comparison in the variation of lift-to-drag ratio with angle of attack between 8T and the baseline for Reynolds number of (a)201,200, (b)246,100, (c)296,200, and (d)315,600	108

Figure 70. Drag polar comparison between 8T and baseline for Reynolds number of (a)201,200, (b)246,100, (c)296,200, and (d)315,600.....	109
Figure 71. Instantaneous (a)axial velocity and (b)azimuthal vorticity at a Reynolds number of 296,200, 18 degrees angle of attack for the baseline and 8T at two instants	111
Figure 72. Mean (a)axial and (b)transverse velocity contours at a Reynolds number of 296,200, 18 degrees angle of attack for the baseline and 8T	112
Figure 73. Mean (a)azimuthal vorticity and (b)turbulent kinetic energy contours at a Reynolds number of 296,200, 18 degrees angle of attack for the baseline and 8T.....	113

CHAPTER I

INTRODUCTION

Introduction

Seeking to reduce drag penalties during flight is of major importance when it comes to aircraft performance since it can directly translate to increased fuel efficiency. As a result, active research is performed to find a solution to prevent drag increase due to the development of the boundary layer and increase of momentum loss over the surface of the aircraft.

In this chapter, the concepts of biomimetics and flow control are explained, as well as different techniques used to prevent several issues that arise during flight which are detrimental to aircraft performance. Furthermore, the role of the humpback whale and its characteristic tubercles is explained as a drag reduction technique directly from nature and its implementations on engineering applications. Literature review is also presented on previous studies that have been performed on models with leading-edge modifications.

Background

Flow Control

Flow control consists of any modification in configuration or process that influences the development of a flow. For this study, flow control is applied to flows that are bounded to a wall by purposely prompting the boundary layer of the fluid flow to behave differently than it normally and naturally would if it were not modified in any way (Flatt, 1961). Among the several tasks flow control can affect positively the following can be mentioned: diminish the

boundary layer growth, delay or induce separation in flow, minimization of drag, enhancement of lift and reduction of flow-induced noise (Yagiz *et al.*, 2012; Gad-el-Hak, 1998).

Several flow control techniques that have been developed are commonly classified in two categories depending on energy expenditure: active flow control (AFC) and passive flow control (PFC). In the literature a third category is also mentioned: hybrid flow control, which is a combination of both active and passive techniques (Aftab *et al.*, 2016).

Active flow control techniques require the input of energy through mechanisms such as actuators. These techniques can be controlled using a feedback control system to obtain specific and desired conditions (Zhang *et al.*, 2013). On the other hand, passive flow control techniques consist of modifications or addition of fixed elements on the suction surface of an airfoil (Hansen, 2012).

In contrast with AFC techniques, PFC results in a gain of energy from the consequent controlled flow. PFC techniques are simple, cheap, minimally complex, and result in wide applications and implementations (Zhang *et al.*, 2013). PFC includes adding roughness, riblets, vortex generators, membranes, or modifications to airfoil geometry. These techniques result in enhancement of performance and stall characteristics and have therefore been applied in several applications (Mwenegoha *et al.*, 2013).

Biomimetics

The study of structures, formations or functions of biological processes with the objective of utilizing similar processes in artificial mechanisms is known as biomimetics (Aftab *et al.*, 2016). In other words, biomimetics imitate nature as a mean of developing or improving mechanical systems and solving contemporary challenges.

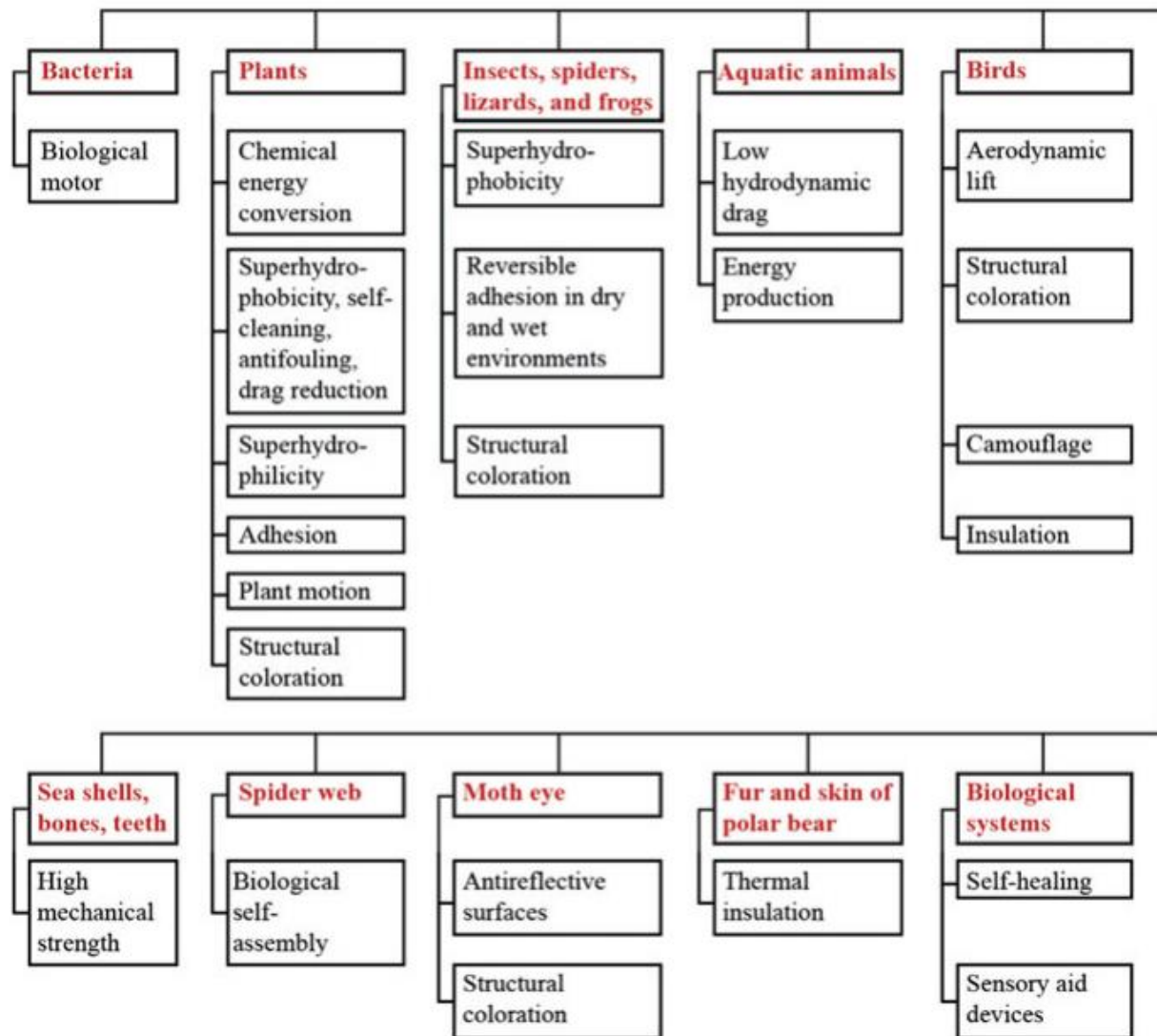


Figure 1. Overview of various species and objects from living nature and their selected functions. Image via Bhushan, 2016

Nowadays, engineers are using the investigations performed by biologists as inspiration for technological development (Fish *et al.*, 2011). By observing the evolution of species throughout the years, the importance of studying nature to solve technological purposes arises. Organisms have interacted within each other and the environment in which they live in, which has prompted the evolution of multifunctional elements within species (Bhushan, 2016).

Biomimetics is expressed to be highly interdisciplinary since it requires the understanding of biological principles that compose nature and engineering principles to comprehend their functions (Fish *et al.*, 2011). Hence, it can be implemented by engineers, biologist, physicists, chemists, material scientists, artists, and architects in their area (Bhushan, 2016). Figure 1 shows several species and the properties of interest of each of them. For example, birds have wings that are flexible, which are composed of several rows of feathers. Birds are capable of generating the aerodynamic lift necessary to rise in flight (Bhushan, 2016). Another example is the properties of aquatic animals, which is the basis of this experimental study. There are several elements in aquatic animals that serve a function in their performance: scales in the shortfin mako shark prevent flow separation and, at moderate and high angles of attack (AoA), grooves of scallops increase the lift-to-drag (L/D) ratio (Kim *et al.*, 2018).

Even though biomimetics can be highly useful to tackle mechanical problems, challenges can arise when finding a solution through biological means. Biological processes operate under different principles to technological processes since there is a difference in the materials available, the size of structure, and the speed of operation. Therefore, it is important to use processes in which there is an available overlap between the biological process and the engineering application. For this, engineers can explore the three strands of development identified in biomimetics. For example, the first strand of development, which is the functional

morphology, form and function, is favored when the material properties are not essential to the function. In this strand, it is of major importance that the function is a consequence of the form and structure of the biological process being studied and not the material properties of such. Hence, the material can be readily replaced by an artificial one. This strand is highly successful when applied to fluid dynamics (Gleich *et al.*, 2009; Helfman Cohen *et al.*, 2016).

The tubercles of the humpback whale flipper, which functions at the same Reynolds number range as several engineering applications, is an example of a functional morphology, form and function strand of development. For a couple decades, the tubercles of the humpback whale flipper have been studied to determine the effects of their configuration on aerodynamic performance when used as a passive flow control device (Fish *et al.*, 2011).

Humpback Whale and Tubercles as a PFC Device

The humpback whale (*Megaptera novaeangliae*) is one of the largest animals. Depicted in Figure 2, they approximately measure 15.6 m in length and weigh 34 tons. Even though their bodies are inflexible for the most part, these baleen whales require the ability to perform complex acrobatic maneuvers, like loops, rolls, and tight turning due to their unique feeding behavior known as bubble netting (Miklosovic *et al.*, 2004; Wei *et al.*, 2015; Kim *et al.*, 2018; Aftab *et al.*, 2016). Bubble netting consists in “creating a zone around the prey and then sudden lunging towards it” (Aftab *et al.*, 2016). Therefore, humpback whales have gained the ability to perform underwater somersaults and swim at particularly high angles of attack (Aftab *et al.*, 2016; Bolzon *et al.*, 2016). The agility of the humpback whales has been attributed to a special feature found on their pectoral fins: the presence of bumps along the leading-edge, named tubercles. Tubercles have been observed to modify the performance characteristics of the flipper when turning, characterizing them as rather agile creatures (Miklosovic *et al.*, 2004).



Figure 2. Humpback whale. Image via Tom Collins/Wildlife conservation

The pectoral fin has a symmetric profile, with a rounded leading-edge and semi-sharp trailing-edge, similar to that of the NACA 634-021 airfoil; the maximum thickness is found to vary from 20% at the midspan to 40% of the chord length near the tip of the fin (Post *et al.*, 2018; Aftab *et al.*, 2016). On average, the flipper size has a span of 5 meters and chord of 0.50 meters, which results in an aspect ratio of about 10 (Post *et al.*, 2018; Wei *et al.*, 2015). The humpback whale's pectoral fin has in average 10 to 11 bumps on the leading edge (Fish *et al.*, 2011). These tubercles can be characterized by their amplitude and wavelength. The amplitude is the distance from the trough of the tubercle to the immediate peak. The wavelength is the distance from the tubercle or peak to the next tubercle or peak, respectively.

Considering that the average speed at which a humpback whale swims is about 1.3 to 4 m/s and the viscosity of seawater is $1.35 \times 10^{-6} \text{ m}^2/\text{s}$, the Reynolds number at which these mammals swim is to the order of 10^6 , around 960,000 (Post *et al.*, 2018; Wei *et al.*, 2015). Reynolds numbers in the range of $10^4 - 10^6$ are considered low Reynolds number flow. Wind turbine

blades, unmanned aerial vehicles, sailboat centerboards, and boat rudders are among the various applications that operate at low Reynolds number like the humpback whale (Hansen *et al.*, 2011). At this range of Reynolds number, complex phenomena are present in the boundary layer. For example, for a lifting surface, increasing the angle of attack can lead to separation of laminar flow very close to the leading-edge, hence causing stall, and a laminar bubble commonly forms (Aftab *et al.*, 2016; Guerreiro *et al.*, 2012). These characteristics have a significant effect on the aerodynamic performance of the lifting surface.

Consequently, tubercles have been implemented as a passive flow control device of increasing research interest by modifying the conventional straight leading-edge of an airfoil (Fish *et al.*, 2011). From experimental and numerical studies, it has been found that the presence of tubercles creates pairs of counter-rotating streamwise vortices, which are responsible for the enhancement in the performance of airfoils (Bolzon *et al.*, 2016; Hansen *et al.*, 2011). In the literature, tubercles have been compared to vortex generators due to the increase in momentum that is injected into the boundary layer; however, other studies have contradicted this conclusion by pointing out that the amplitude and wavelength of the tubercles is larger than the boundary layer thickness which doesn't make it possible to compare vortex generators with the addition of leading-edge tubercles (van Nierop *et al.*, 2004).

In the past decade, numerous studies have been performed to characterize the performance of tubercles with various tubercle configurations on different airfoil profiles. In these studies, airfoils have been tested in different conditions, such as varying of the Reynolds numbers, freestream turbulence intensity, and angles of attack. The following section gives an extensive review of the studies that have built up on the importance of leading-edge tubercles and the effect it has on the aerodynamic performance of airfoils in particular.

Literature Review

The effects of leading-edge tubercles on airfoil performance has been studied in multiple occasions. In this section, previous studies performed on several airfoil profiles at freestream turbulence intensities of 1% or less are presented. Such studies were performed under different flow field conditions to understand the effect of leading-edge tubercles under these particular circumstances.

First, the general effects of tubercles on the aerodynamic performance is presented by studying the aerodynamic characteristics and comparing them to a baseline. The effect of leading-edge tubercles on drag coefficient, lift coefficient, and stall behavior is reviewed. There are several parameters varied in these studies that will affect the exact level of performance enhancement; however, the main effect of the addition of tubercles on the leading-edge of the model is summarized. Since the leading-edge tubercles can be represented using a sinusoidal function, the amplitude and wavelength of such can be varied with the purpose of finding the optimal configuration that would present most beneficial to the performance of the model. In the literature, this change in amplitude (A) and wavelength (λ) is shown as a percentage of the chord length ($\%c$). For this section, mostly the aerodynamic characteristics are used to determine the optimal tubercle configuration. Continuing with the effect of Reynolds number on aerodynamic performance, several studies in which the Reynolds number was varied from low to moderate, in order to simulate that of MAVs, UAVs, wind turbine blades, sailboat centerboards, and boat rudders, is presented. Also, flow visualization techniques are used to study the effect of leading-edge tubercles on the flow field characteristics.

On a final note, the end of this section is devoted to summarizing the findings that have been reported up to date for low freestream turbulence intensities in order to understand fully the motivation and intent behind this project.

Effects of Tubercles on the Aerodynamic Characteristics

Among the several studies that have been performed on leading-edge tubercles in recent years, the research of Hansen *et al.* has been of great contribution to the characterization of this passive flow control device. In 2011, Hansen *et al.* performed an experimental study on two full-span models, NACA 0021 and NACA 65-021 airfoil, at freestream Reynolds number of 120,000 and freestream turbulence intensity of approximately 0.8%. For the NACA 0021 airfoil with leading-edge tubercles, it was reported that lift significantly increased; however, the stall behavior is more abrupt at lower angles of attack. Figure 3(a) shows the lift coefficient results for the NACA 65-021 airfoil. In the prestall regime, the results show that the models with leading-edge tubercles (A4 λ 30 and A8 λ 30) show no significant performance enhanced, similar behavior is recorded for the model with NACA 0021 profile not depicted. However, there is performance enhancement observed in the poststall regime, meaning greater lift produced and more gradual stall in comparison with the baseline (65021 unmod). Such response is evident in the elimination of the sudden dip of the lift coefficient at 15 degrees. In terms of drag coefficient, Hansen *et al.* (2011) reported that for both airfoil profiles, a lower drag was recorded at high angles of attack in comparison with the baseline. Figure 3(b) shows the effects on drag coefficient for the NACA 65-021 airfoil.

In another experimental study, Zhang *et al.* (2013) studied the effects of tubercles on a full-span NACA 63-021 at freestream Reynolds number of 50,000 and freestream turbulence intensity of 0.5%. The study reported that performance characteristics of the airfoil declined within the stall region, which is the opposite of the results obtained by Hansen *et al.* (2011). However, in the poststall regime, Figure 4(a) shows there was an increase in lift coefficient and lift-to-drag ratio, 25% and 39.2%, respectively, and decrease in drag coefficient by 20% recorded

by the leading-edge tubercle airfoil (5.0×10^4 , Wavy airfoil) in comparison with the baseline (5.0×10^4 , Baseline airfoil), in agreement with the results from Hansen *et al.* (2011).

Afterward, Zhang *et al.* (2014) performed an experimental study on the same airfoil profile as the previous study, NACA 63-021. The full-span airfoil was studied at a higher freestream Reynolds number of 200,000 and lower freestream turbulence intensity of $<0.2\%$. Zhang *et al.* (2014) observed that leading-edge tubercles delayed stall. However, it was reported, in agreement with Zhang *et al.* (2013) and Hansen *et al.* (2011), there was a slight impairment in the performance of the airfoil in the prestall regime. As depicted in Figure 5(a), in the poststall regime, an increase of 54.5% in C_l , increase of 67.7% in L/D ratio, and decrease of 6.7% in C_d for the modified model ($Re=2.0 \times 10^6$, Baseline Airfoil, Present) in comparison with the baseline (2.0×10^6 , Wavy Airfoil, Present), showing performance enhancement (Zhang *et al.*, 2014).

Two years later, an experimental study was performed by Bolzon *et al.* (2016) on two swept NACA 0021 airfoils at freestream Reynolds number of 225, 000 and freestream turbulence intensity of $0.6 \sim 0.8\%$. Regarding drag coefficient distributions, for angles of attack at and below 6 degrees, the leading-edge tubercles reduced the profile drag coefficient; the effect on induced drag was negligible. For higher angles of attack, 9 degrees and higher, the leading-edge tubercles increased the profile drag coefficient and reduced induced drag coefficient. It is reported that the latter result is due to the flow separation at the region of the wingtips. Continuing with drag coefficient results, for the leading-edge tubercle airfoil, profile and induced drag coefficients were modulated by the tubercles along the span of the airfoil. Profile drag coefficient was reported “with local maxima and minima [...] forming in the troughs and over the peaks, respectively,” and induced drag coefficient was reported with “local maxima and minima [...] over the peaks and in the troughs, respectively” (Bolzon *et al.*, 2016).

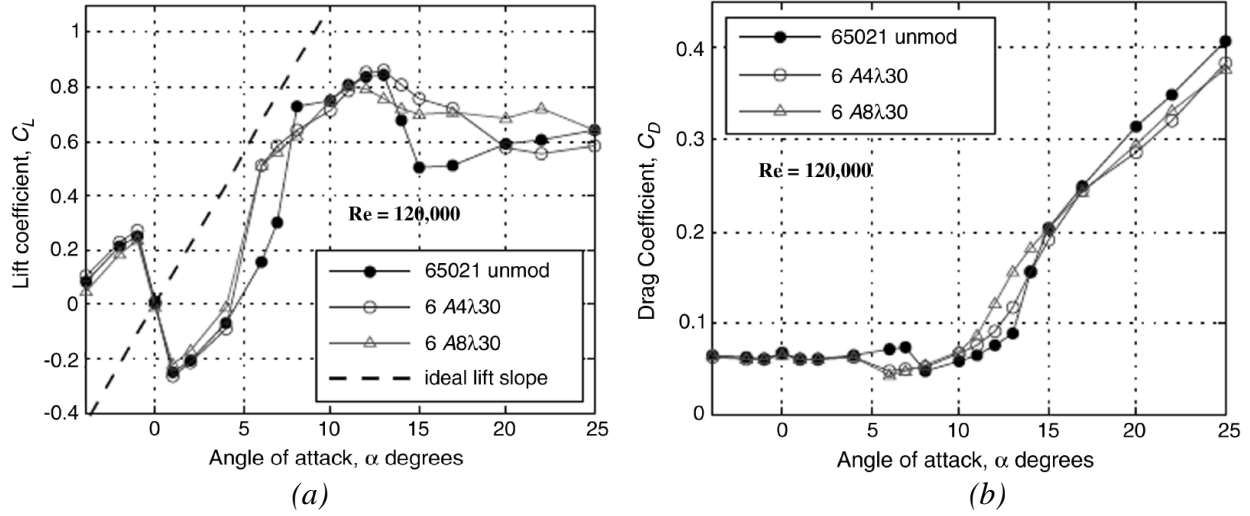


Figure 3. (a)Lift and (b)drag coefficient vs angle of attack for NACA 65-021.
Image via Hansen, 2011

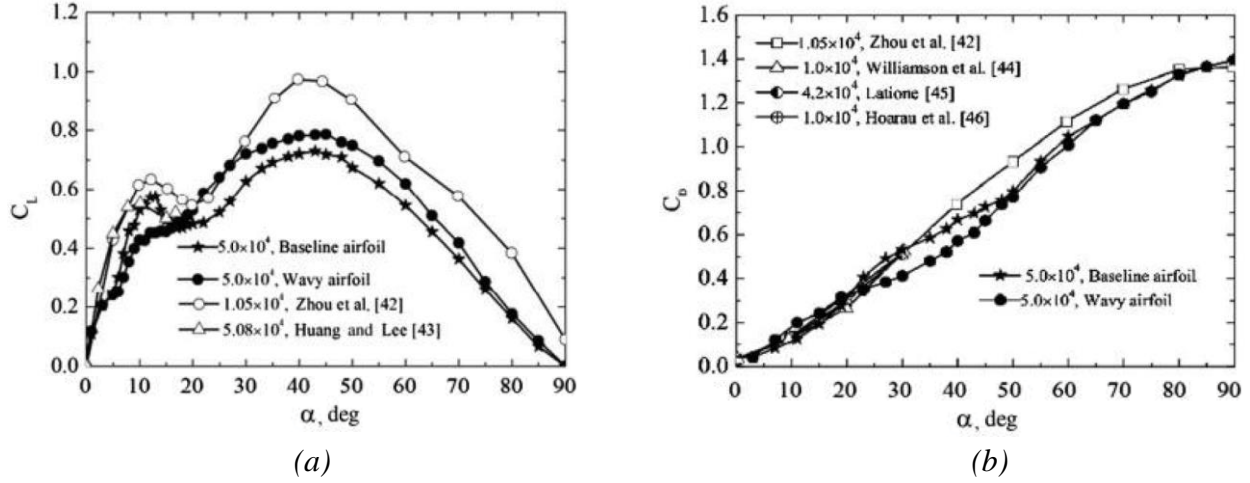


Figure 4. (a)Lift and (b)drag coefficient vs angle of attack for NACA 63-021.
Image via Zhang, 2013

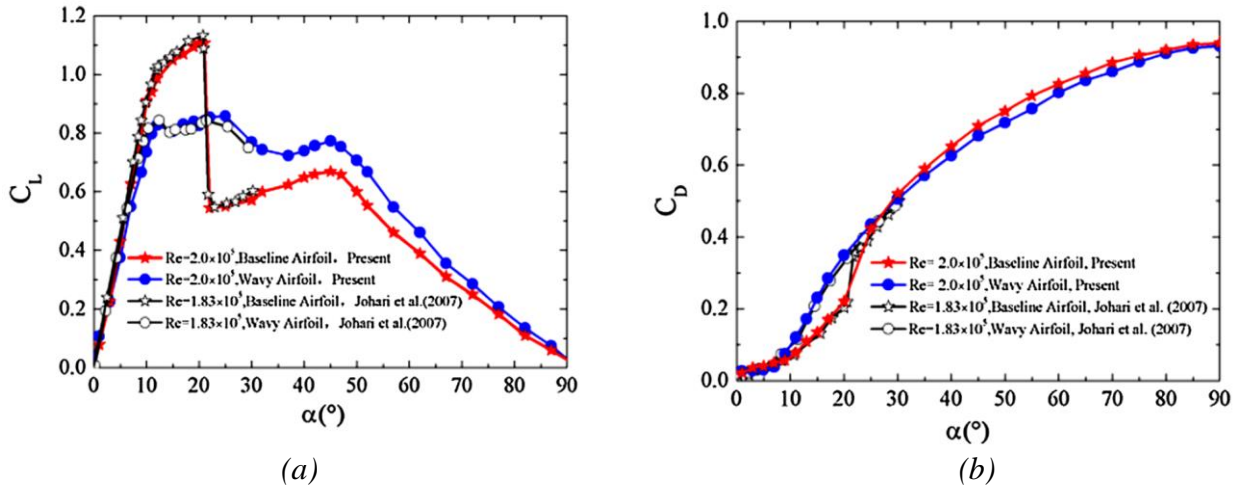


Figure 5. (a)Lift and (b)drag coefficient vs angle of attack for NACA 63-021.
Image via Zhang, 2014

More recently, Kim *et al.* (2018) studied the effect of leading-edge tubercles on an airfoil with a NACA 0020 profile at freestream Reynolds number of 180,000 and freestream turbulence intensity of 0.3%. Figure 6(a) shows the lift coefficient results obtained. It was noted by the authors that the lift coefficient for both airfoils increased linearly up to an angle of attack of 7 degrees; however, there was a difference in the slope of 4.87 and 4.58 for the baseline (Base (Re=180,000; present)) and the airfoil with leading-edge tubercles (Tubercle (Re=180,000; present)), respectively, which wasn't noted by other authors. In this study, the lift coefficient for the leading-edge tubercles remains constant for about 5 degrees before stalling. This behavior wasn't noted for the baseline. In agreement with previous studies, Kim *et al.* (2018) reported an increase in the stall angle of 7 degrees and an increase in the maximum lift coefficient of about 22%. After reaching 25 degrees, both airfoils behave similarly, concluding that the tubercles produce a negligible advantage for high angles of attack. Figure 6(b) shows the drag coefficient results. From the results, Kim *et al.* (2018) concluded that the tubercles showed a significantly lower drag coefficient in the range of 9 to 15 degrees, which also coincides with the range of angles of attack where the lift coefficient remained constant.

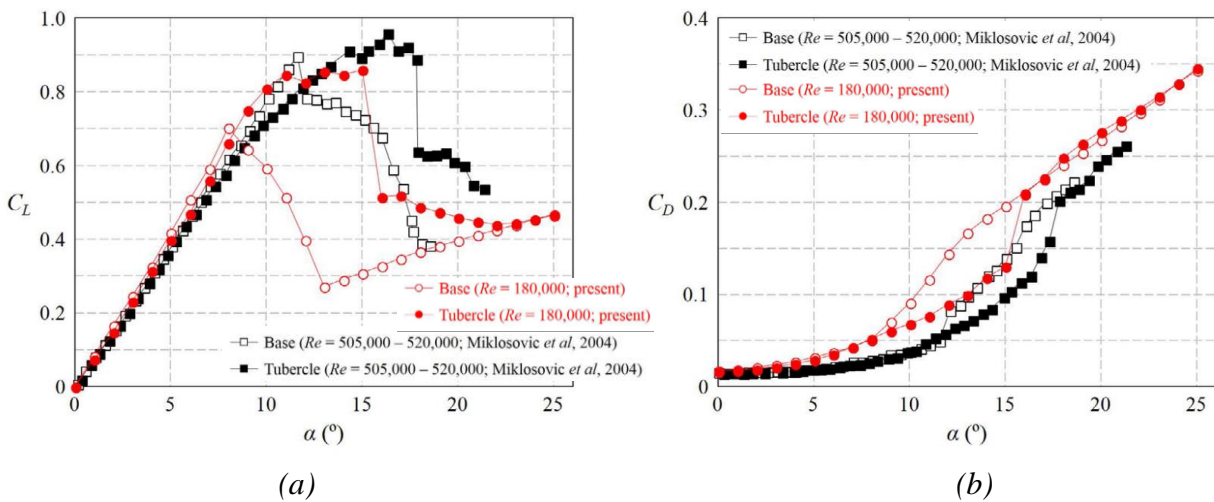
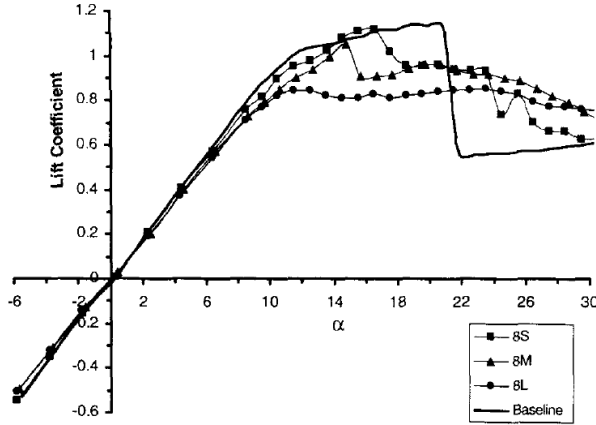


Figure 6. (a) Lift and (b) drag coefficient vs angle of attack for NACA 0020.
Image via Kim, 2018

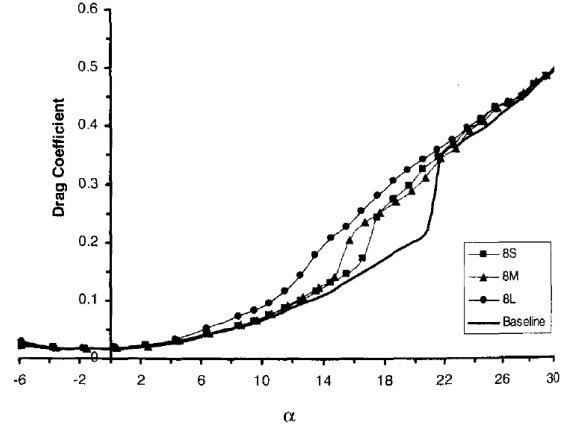
Effects of Tubercle Configuration on the Aerodynamic Characteristics

The purpose of finding the optimal tubercle configuration led Johari *et al.* (2007) to perform an experimental study on a NACA 63-021 at freestream Reynolds number of 183,000 and at freestream turbulence intensity of 0.6%. The amplitude of the leading-edge tubercles was varied from 2.5 to 12% of the mean chord length. The wavelengths studied were 25 and 50% of the mean chord length. Johari *et al.* (2007) reported that for the airfoil with greater amplitude, in the poststall regime, the lift coefficient C_l was smaller by 28% than the baseline's maximum lift coefficient $C_{L\max}$; however, C_l for the leading-edge tubercle airfoil was 40% greater than that of the baseline in the poststall regime. Regarding drag coefficient, higher C_d values were observed for the airfoil with greater amplitude at any angle of attack; however, at significantly higher angles of attack, C_d appears to be independent of tubercle configuration, as observed in Figure 7(b) and Figure 10(b). The effect of variation in wavelength was also studied in Johari's study. It was reported that there was minimal difference between the two wavelengths studied. There was no more than 10% difference between the airfoil with greater amplitude in the lift coefficient at different wavelengths; similarly, the drag coefficient experienced similar behavior within the same amplitude (Johari *et al.*, 2007). However, the airfoils with shorter wavelength generate slightly less drag than its counterpart for the angles of attack studied.

Hansen *et al.* (2011) studied the effects of varying the amplitude (A) and wavelength (λ) of the sinusoidal function. It was reported that for the airfoil profiles studied, NACA 0021 and NACA 65-021, the increase in amplitude results in smoother stall characteristics. However, the maximum lift coefficient $C_{L\max}$, and stall angle α_{stall} decreased in comparison with the baseline. On the contrary, the airfoil profiles with the smallest-amplitude tubercles resulted in performance enhancement in the poststall regime, higher value of $C_{L\max}$ and α_{stall} .

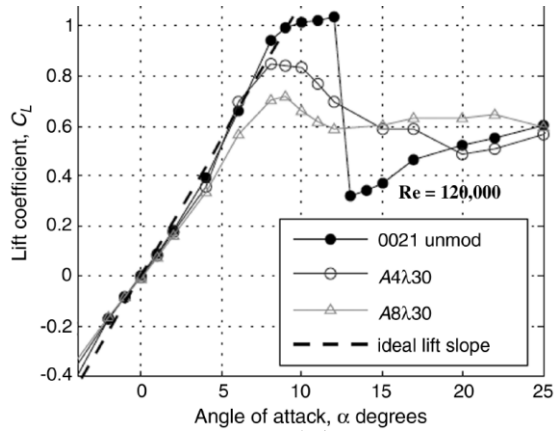


(a)

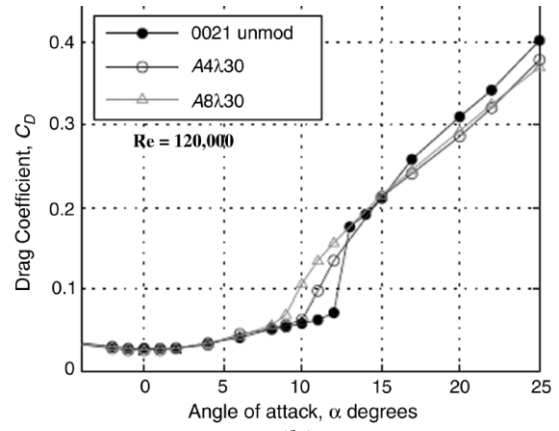


(b)

Figure 7. Effect of amplitude variation on (a) lift and (b) drag coefficient for NACA 63-021 with 25% c wavelength. Image via Johari, 2007

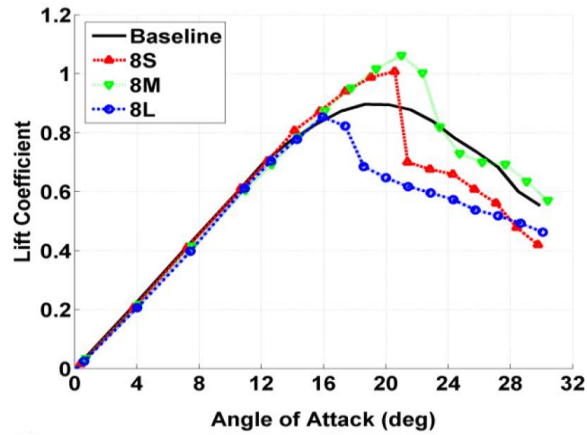


(a)

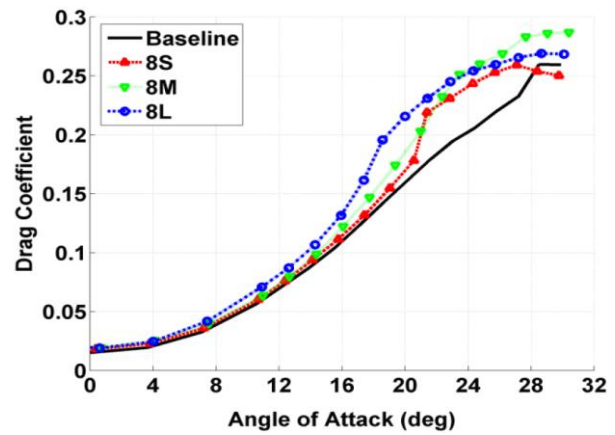


(b)

Figure 8. Effect of amplitude variation on (a) lift and (b) drag coefficient for on NACA 0021 with 43% c wavelength. Image via Hansen, 2011

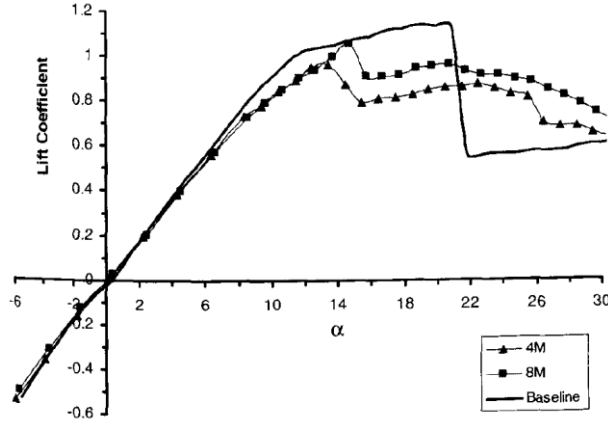


(a)

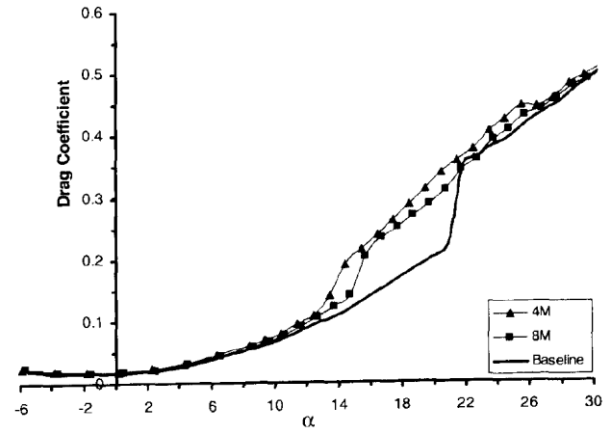


(b)

Figure 9. Effect of amplitude variation on (a) lift and (b) drag coefficient for NACA 63-021 with 25% c wavelength. Image via Custodio, 2015

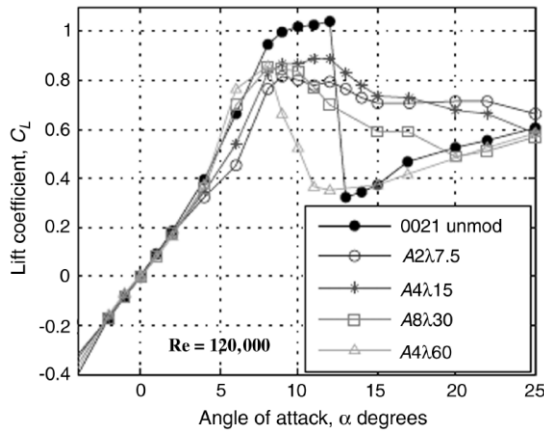


(a)

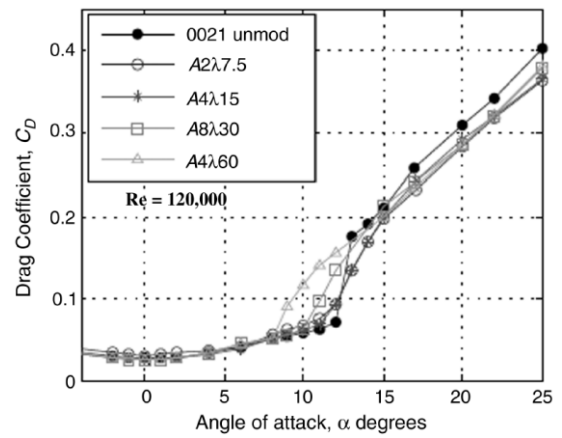


(b)

Figure 10. Effect of λ variation on (a) lift and (b) drag coefficient for NACA 63-021 with 5% c_a . Image via Johari, 2007

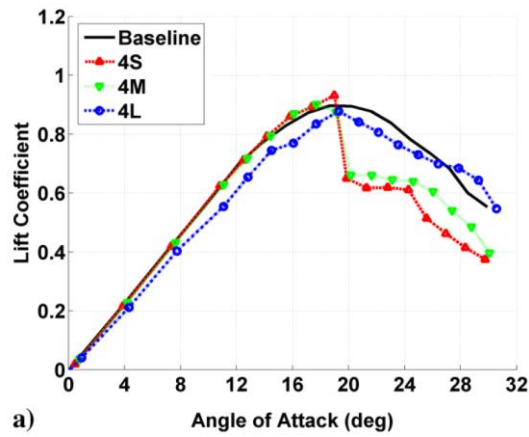


(a)

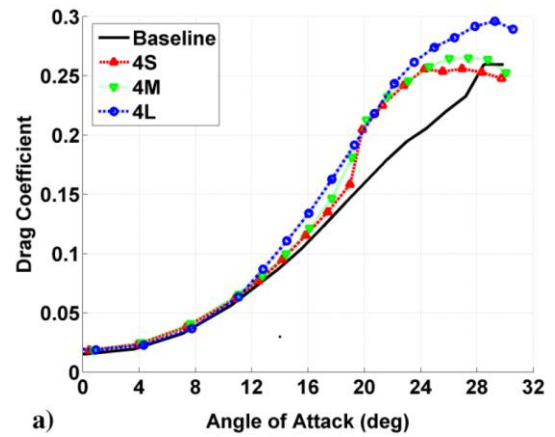


(b)

Figure 11. Effect of λ variation on (a) lift and (b) drag coefficient for NACA 0021 with various A . Image via Hansen, 2011



(a)



(b)

Figure 12. Effect of amplitude variation on (a) lift and (b) drag coefficient for NACA 63-021 with 50% c_a wavelength. Image via Custodio, 2015

However, reducing tubercle amplitude resulted in characteristics similar to the baseline in the prestall regime. Regarding drag characteristics, the effect of tubercle amplitude was reported to be negligible at low angles of attack. Figure 8 shows the effect of amplitude on drag and lift coefficient. Hansen *et al.* (2011) reported the effects of wavelength variation on a NACA 0021 airfoil. As shown on Figure 11, the decrease of wavelength resulted in improvements in the performance characteristics of the modified model (A4 λ 15 and A4 λ 60) in comparison with the baseline (0021 unmod). However, Hansen *et al.* (2011) reported that there are limitations in the improvements for certain tubercle amplitudes.

Among the studies that have studied the effect of tubercle configuration on airfoil performance, Guerreiro *et al.* (2012) studied various models with NASA LS(1)-0417 airfoil profile at Reynolds numbers of 70,000 and 140,000 and freestream turbulence intensity of 0.2%. In Guerreiro's study, the aspect ratio of the airfoils was varied from 1 to 1.5. For airfoils with an aspect ratio of 1, Re of 140,000, and amplitude of 0.012c, decreasing the wavelength from 0.50c to 0.25c resulted in $C_{L\ max}$ decreasing from 0.142 to 0.136; however, the angle of attack at which $C_{L\ max}$ was achieved remained unchanged. In comparison with sinusoidal airfoil with 0.50c wavelength, which did not stall for angles of attack tested, the stall angle was found to be 20° for sinusoidal airfoil with 0.25c wavelength, lower than the α_{stall} of the baseline. In airfoils with a wavelength of 0.50c, decreasing the amplitude from 0.12c to 0.06c resulted in $C_{L\ max}$ slightly increasing from 0.142 to 0.143 and its corresponding $\alpha_{C_{L\ max}}$ decreasing to 27°. The α_{stall} increased significantly to 27°. From the results, it was reported that the sinusoidal model with smaller amplitude and higher wavelength had better performance enhancement than the other models, even though all models tested experienced more favorable stall characteristics in comparison with the baseline however slightly (2012).

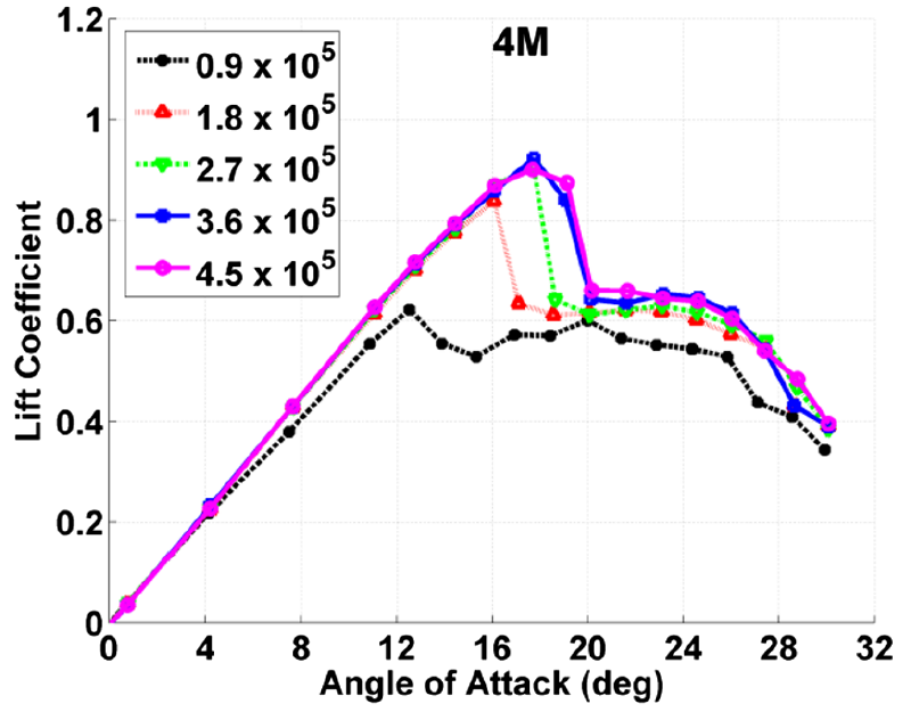
Custodio *et al.* (2015) performed an experimental study on several models with a NACA 63-021 airfoil profile at freestream Reynolds number ranging from 90,000 to 450,000 and freestream turbulence intensity of 0.6 ~ 1.0%. The profile chosen in this study is the same as that of Johari *et al.* (2007). In the study, six different rectangular-planform models were tested. The amplitude was varied from 0.025c to 0.12c. The wavelengths examined were 0.50c and 0.25c. For all rectangular-planform models tested, the results showed that the lift slope was very similar to that of the baseline; however, the model with 0.50c wavelength and 0.12c amplitude had a 10% smaller lift slope, as observed when comparing Figure 9(a) and Figure 12(a). Kim *et al.* (2018) also pointed out a difference in the lift slope for a symmetrical airfoil, NACA 0020, at a Reynolds number of 180,000.

For models with 0.50c wavelength, models with 0.025c and 0.050c amplitude were observed to stall abruptly, resulting in a rapid loss lift at the stall angle; however, when increasing the amplitude to 0.12c, the stall characteristics resembled those of the baseline (Custodio *et al.*, 2015). For models with 0.25c wavelength, models with 0.025c and 0.050c amplitude showed higher lift coefficients than the baseline for approximately a range of angle of attack from 15 to 21 degrees. It was reported by Custodio *et al.* (2015) that for models with a wavelength of 0.50c, a higher amplitude was observed to experience lift enhancement in comparison with smaller amplitude models. However, for models with a wavelength of 0.25c, a smaller amplitude of 0.050c and 0.12c resulted in better lift characteristics. Regarding drag calculations, Custodio *et al.* (2015) reported that for wavelengths of 0.25c and 0.50c, increasing the amplitude resulted in higher drag coefficient.

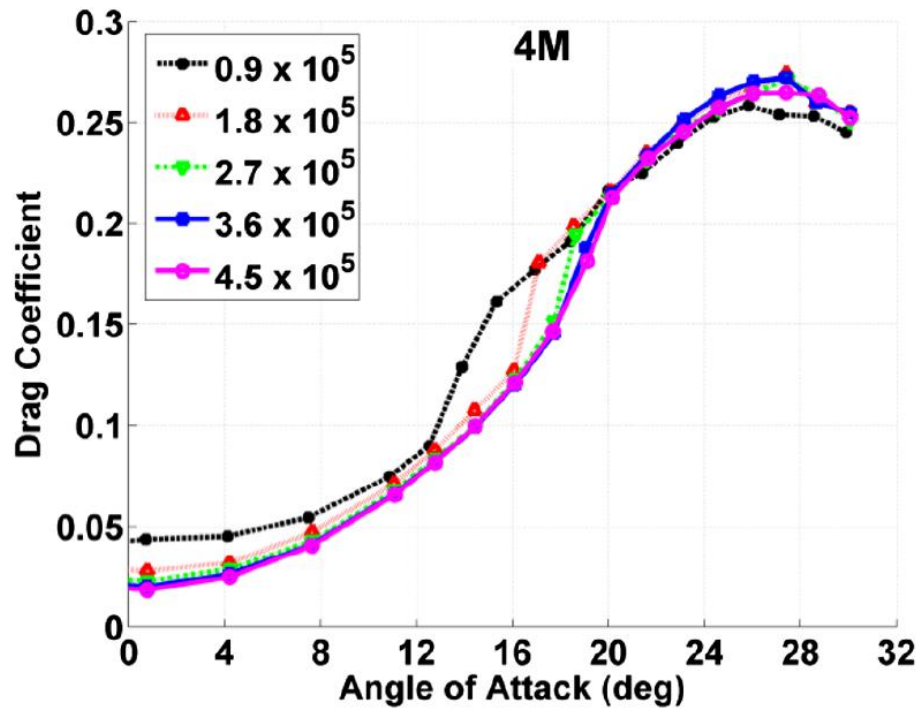
Effects of Reynolds Number on the Aerodynamic Characteristics

Among the various experimental studies that have been performed, the variation of Reynolds number is present in its majority. The effect of low to moderate Reynolds number is important due to the range of applications that have been linked to the application of leading-edge tubercles. As part of this purpose, an experimental study was performed by Guerreiro *et al.* (2012) compared the effects of Reynolds number on the performance characteristics of an airfoil by performing experiments for Reynolds numbers of 70,000 and 140,000. For airfoils with an aspect ratio of 1, Reynolds number was decreased to 70,000. The effects, on one hand, seemed to be negligible; however, it was noted that for the baseline at this Reynolds number, the model was not capable to produce lift at zero angle of attack. For the sinusoidal models, the change in Reynolds number seemed to be very similar to results obtained for higher Reynolds number, if not slightly detrimental to the performance (2012).

Custodio *et al.* (2015) reported the effects of Reynolds number by varying Reynolds number ranging from 90,000 to 450,000 on six rectangular-planform models. It was reported that for Reynolds number up to 360,000, excluding the linear regime of the lift coefficient curve, there was a dependency on the Reynolds number for all models tested. Custodio *et al.* (2015) observed that as the Reynolds number increased, the $C_{L\max}$ and α_{stall} increased as well. In Figure 13(a), it can be seen however that for Reynolds numbers higher than 360,000, there was little change in the lift, meaning that at this point, lift and drag coefficient are independent of Reynolds number. Regarding drag coefficient, the effect of Reynolds number was also studied. It was reported that drag coefficient of the rectangular-planform models was also affected by the variation of Reynolds number.



(a)



(b)

Figure 13. Effect of Reynolds number on (a) lift and (b) drag coefficient for NACA 63-021 with 5% c A and 50% c λ .

Image via Custodio, 2015

Custodio *et al.* (2015) reported that the minimum drag coefficient was reduced as the Reynolds number increased. However, it was reported that at poststall angles of attack, the Reynolds number had little effect on the drag characteristics. Similarly, Figure 13(b) shows that the drag coefficient appeared to be nearly independent of Reynolds number above 360,000.

A more recent experimental study was performed by Post *et al.* (2018) on six wing geometries modeled as a NACA 0020 airfoil at freestream Reynolds number ranging from 100,000 to 500,000 and freestream turbulence intensity of $<0.2\%$. It was observed that for the sinusoidal-channeled leading-edge airfoil, based on whale geometry, the stall characteristics were similar between the different Reynolds numbers tested, which was softer stall in comparison than the baseline. For Reynolds number ranging from 200,000 to 500,000, a similar lift coefficient is recorded in the poststall regime (Post *et al.*, 2018).

In the same year, Kim *et al.* (2018) reported a decrease in the lift slope of the tubercles in comparison with the baseline for a Reynolds number of 180,000. In comparison with another experimental study performed by Miklosovi *et al.* (2004) where the same airfoil model was utilized at higher Reynolds number, this change in lift slope was not evident. It was concluded by Kim *et al.* (2008) that the decrease of the lift slope resulted due to lower Reynolds numbers.

Effects of Tubercles on Flow Field Characteristics of a Wing

Streamwise vortices have been reported throughout the years in the literature. Flow visualization is a given tool that can be utilized to observe the behavior on the surface of the airfoils, confirming the generation of such streamwise vortices. Hansen *et al.* (2011) reported that, using hydrogen-bubble visualization, streamwise vortices are formed specifically in the troughs. An apparent increase in turbulence was reported by Hansen *et al.* (2011) in smaller tubercle wavelength. It was noted that such behavior may cause an increase in momentum

exchange and attachment to the airfoil surface. Hence, the performance enhancement reported in the poststall regime for airfoils with leading-edge tubercles.

Zhang *et al.* (2013) reported, by data measured using Particle Image Velocimetry (PIV), that there was an earlier separation of the flow in the trough-plane; as shown in Figure 14(a) and (b), whereas, the flow in the peak-plane remains attached to the surface longer. As reported by Hansen *et al.* (2011), generation of vortices were attributed to the addition of leading-edge tubercles, which become stronger with increasing angle of attack; furthermore, such vortices were observed to be responsible for the noted behavior of the flow in the peak-plane and trough-plane (Zhang *et al.*, 2013). Zhang *et al.* (2013) concluded that the flow over the trough section was responsible for the “earlier laminar separation, and more laminar/turbulence transition, turbulent reattachment, and turbulent boundary-layer detachment.” The flow over the peak sections, on the other hand, was attributed the performance characteristics of the airfoil during poststall regime (Zhang *et al.*, 2013).

In agreement with Zhang *et al.* (2013), Zhang *et al.* (2014), through oil-flow visualization, reported that flow separation occurred earlier for the trough-plane, than the peak-plane. In the poststall regime, the flow separates from the surface almost at the leading-edge of the baseline; on the contrary, even though there is a stronger flow separation in the trough-plane, the flow remains attached for a longer period for the peak-plane (Zhang *et al.*, 2014). The generated streamwise vortices observed during this experimental study within the stall and in the poststall regime were associated with the transformation from an earlier laminar separation, which resulted in a turbulent near the bump within the stall regime, and an otherwise strong laminar flow attachment near the bump in the poststall regime (Zhang *et al.*, 2014).

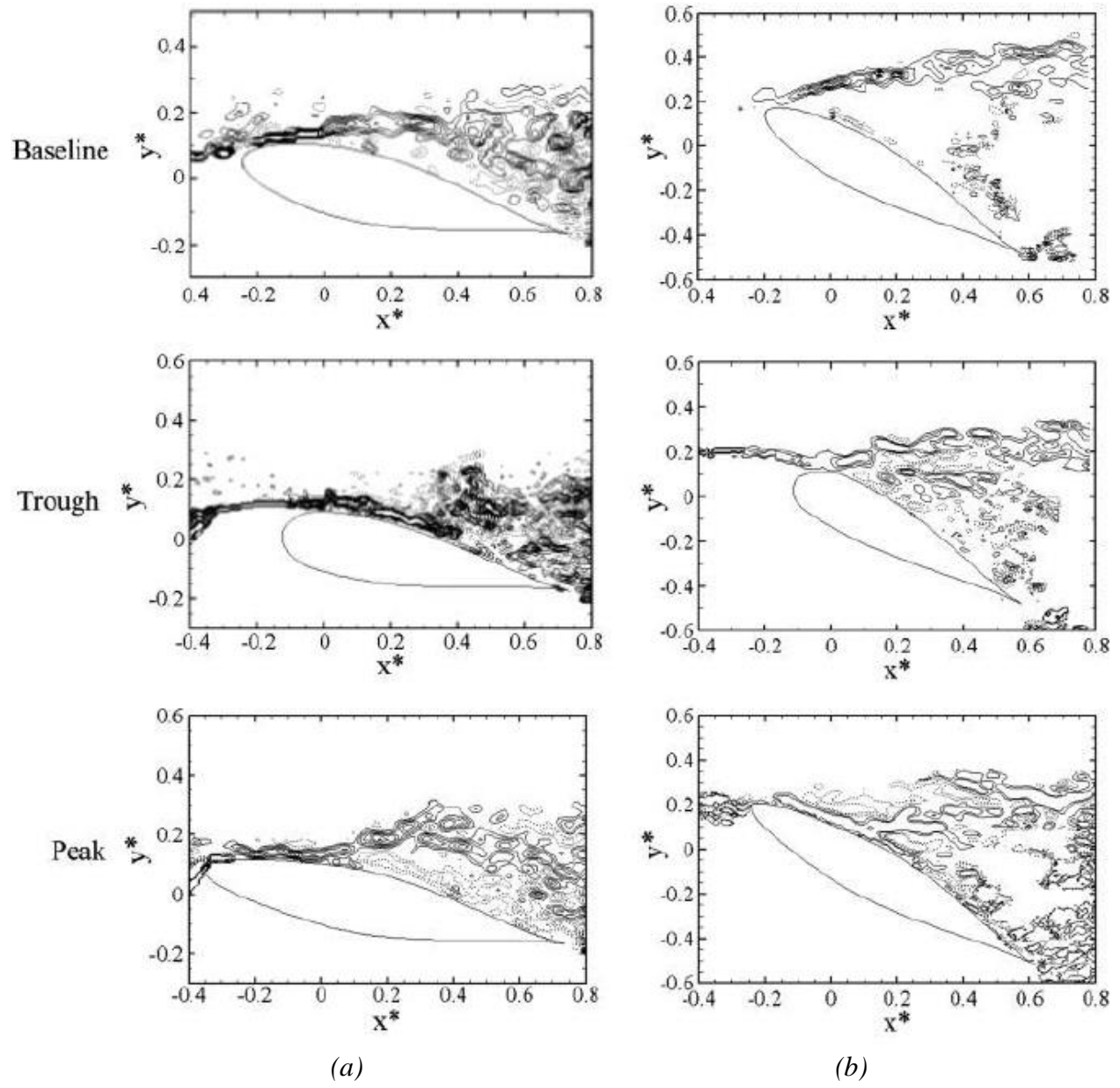


Figure 14. Normalized instantaneous streamwise vorticity for angle of attack of (a) 13 deg and (b) 40 deg.
Image via Zhang, 2013

Another experimental study was performed by Wei *et al.* (2015) on a full span NACA 63-021 airfoil at freestream Reynolds number of 14,000 and freestream turbulence intensity of 1.1%. Wei *et al.* (2015) determined, using particle-streak photography and Particle Image Velocimetry (PIV), that the usage of leading-edge tubercles introduces a more unstable three-dimensional flow. For the trough-plane, the separation regions were reported to be smaller in comparison with the baseline and no recirculation region was observed. For all angles of attack tested, the flow separates at the leading-edge. Wei *et al.* (2015) reported, for the mid-plane, that for lower angles of attack, the flow remains attached for the entire surface; additionally, for higher angles of attack, the flow remains attached for almost $1/3c$. A weak shear layer is observed. Wei *et al.* (2015) observed similar behavior to Zhang *et al.* (2014) for the peak-plane; leading-edge tubercles lead to better flow separation control for the peak-plane. For angles of attack up to 20 degrees, the flow remains attached to the surface of the airfoil in its entirety. For angles of attack of 20 degrees, the flow remains attached until about $1/3 c$. On the contrary from Zhang *et al.* (2014) results, no shear layer is observed for the peak-plane. Wei *et al.* (2015) explore the generation of streamwise counter-rotating vortex pairs (CVPs) due to leading-edge tubercles. It was reported that CVPs interact with each other, causing an unstable flow behavior.

Summary and Discussion

As of this chapter, the importance of flow control and biomimetics has been stated. The utilization of devices to modify the natural behavior of a flow can be beneficial in several cases. As well, biomimetics has been widely used as innovative flow control techniques. As an example, the humpback whale's pectoral fin has been researched for over a decade as a passive flow control technique for applications with low to moderate Reynolds number.

As it is discussed in the literature, the addition of leading-edge tubercles on airfoils enhances the aerodynamic performance of in the poststall regime. Specifically, leading-edge

tubercles are reported to increase the maximum lift coefficient and the stall angle due to the presence of streamwise vortices due to the tubercles, which enhance the momentum exchange with the boundary layer (Hansen *et al.*, 2011). However, the addition of leading-edge tubercles can also appear to be detrimental for drag coefficient results in the prestall regime.

As part of the continuous studies on leading-edge tubercles, it has been postulated that the performance of tubercles is directly related to their configuration. It has been reported that the proper selection of amplitude and wavelength will result in greater performance enhancement for the airfoils. However, the results have not been in complete agreement as in the optimal amplitude and wavelength and their actual effect on the aerodynamic performance, as shown in Table 1.

Table 1. Summary of effect of tubercle configuration on aerodynamic performance

Year	Author(s)	Airfoil Profile	Re	Amplitude (A)	Wavelength (λ)
2007	Johari <i>et al.</i>	NACA 63 ₄ -021	183,000	Shorter amplitude (2.5%c) generate higher $dC_l/d\alpha$ and $C_{l\max}$ in comparison with greater A	Minimal effect. Shorter wavelength (25%c) generate less C_D
2011	Hansen <i>et al.</i>	NACA 65-021 and 0021	120,000	Shorter amplitude (3%c) achieves $C_{l\max}$	Noticeable effect. Shorter wavelength (11%c) improves lift performance up to a point
2012	Guerreiro <i>et al.</i>	LS(1)-0417	70,000 and 140,000	Larger amplitude (12%c) produces greater C_l	Noticeable effect. Larger wavelength (50%c) produces greater C_l
2015	Custodio <i>et al.</i>	NACA 63 ₄ -021	90,000 to 450,000	Larger amplitude (12%c) produces a more gradual loss in lift	Minimal effect. Larger wavelength (50%c) increases stall angle

Various studies mention that smaller amplitudes have a more positive effect and that wavelength has little effect on the performance in comparison with the amplitude. It has also

been recorded that, on the contrary, greater amplitudes have more positive effect and that wavelength does play an important role. It can be concluded that the amplitude and wavelength selection in leading-edge tubercles is dependent on airfoil profile configuration and cannot be generalized (Hansen *et al.*, 2011; Aftab *et al.*, 2016).

When it comes to the role that the Reynolds number plays on the aerodynamic performance of the airfoils, it has been reported that Reynolds number does play a part in the aerodynamic characteristics, however minimum. It has been stated that as the Reynolds number is increased, the maximum lift coefficient and stall angle of attack also increased. Nevertheless, it has been found that at a certain point, as the Reynolds number is increased, the effect of such becomes negligible.

Different flow visualization techniques have been used to directly observe the behavior of the flow with the addition of leading-edge tubercles. Airfoils with smooth leading-edges are reported to undergo flow separation almost at the leading-edge. With the addition of tubercles, it has been observed that separation no longer occurs at the leading-edge. There is flow attachment to the surface for longer chord lengths. From flow visualization at the peaks and troughs, it has been observed that flow remains attached longer for the peaks than the trough section.

Motivation for the Thesis

Airplanes regularly operate switching between various flight modes, such as take-off, climb, cruise, descend and landing. During these flight conditions, the freestream approaching the wings undergoes fundamental changes. For example, during take-off and landing, the freestream turbulence intensities can reach up to 10% (Watkins *et al.*, 2010).

In the numerous studies that have been performed up until now to characterize the performance of airfoils with various turbulence configuration the turbulence intensities have

been low ($\leq 1\%$). In other words, the performance characteristics of leading-edge tubercles in high freestream turbulence intensities, which occur during take-off and landing, have not been completely investigated yet.

The motivation for this study is to investigate the performance characteristics of leading-edge tubercles when the freestream turbulence intensity is significant ($>4\%$) with the use of velocity and force measurement and flow visualization.

Organization of Thesis

In the following chapters, the experimental setup and methodology used to perform this experimental study is explained. The facility is equipped with a vast array of instruments capable of performing force and momentum measurements, pressure and temperature measurements, and Particle Image Velocimetry studies. The appropriate analysis to obtain the accuracy of the instrumentation is also performed.

After concluding with the experimental setup and methodology, results from the numerical and experimental studies are presented. Finalizing with concluding thoughts on what was learned and proposed future work.

CHAPTER II

EXPERIMENTAL SETUP AND METHODOLOGY

Introduction

The experiments performed for this study were conducted at the University of Texas – Rio Grande at the Aerodynamics and Propulsion Laboratory. The wind tunnel facility located at UTRGV is equipped with instrumentation capable of performing force, pressure, temperature, and flow visualization measurements. In this chapter, specifications and descriptions of the wind tunnel facility are provided.



Figure 15. Wind tunnel facility at UTRGV – Edinburg



Figure 16. Continuation of wind tunnel facility at UTRGV – Edinburg

Wind Tunnel Facility

The wind tunnel facility, pictured in Figure 15 and Figure 16 is located at the Aerodynamics and Propulsion Laboratory at the University of Texas – Rio Grande Valley, Edinburg Campus. The low-speed facility is equipped with an open-circuit subsonic wind tunnel. The maximum freestream velocity achievable is 40 m/s, which correspond to a Mach number of 0.12. The tunnel is driven by a 60HP motor. At the inlet of the wind tunnel, a honeycomb network is found with a 9:1 contraction. The wind tunnel has a test section of two feet high by two feet wide by four feet long. The freestream turbulence intensity is found to be 4%.

Airfoil Geometry

For this experimental study, a NACA 0010 airfoil profile has been chosen with a chord length (c) of 6 inches and a span (s) of 12 inches. The airfoils with a sinusoidal leading-edge have an amplitude of $6\%c$ and variation in wavelength (4, 8, 10, and 12 tubercles along the spanwise direction). Figure 17 shows two renderings of airfoils tested, baseline and modified leading-edge airfoil.

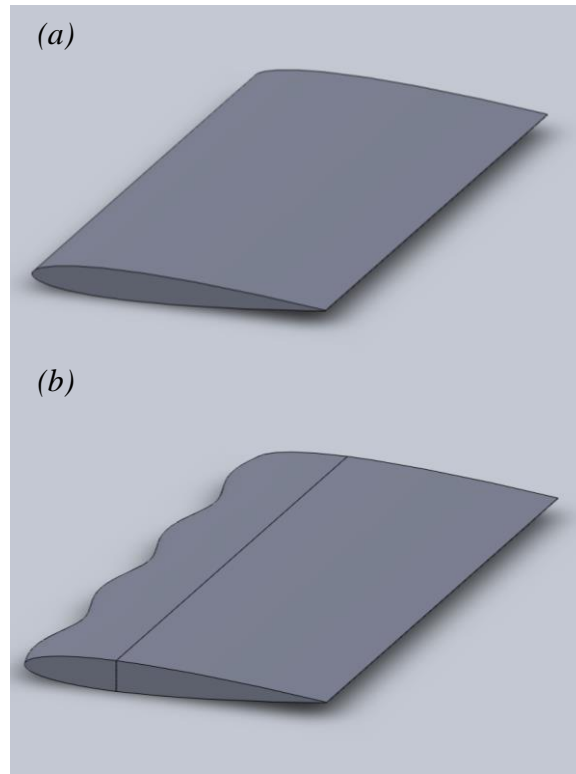


Figure 17. CAD models of (a)baseline airfoil and (b)leading-edge tubercles airfoil.

Table 2. Summary of CAD models with leading-edge tubercles and identification label for airfoils with 6%c amplitude





Amplitude \ # of Tubercles				
	4	8	10	12
6%c	 4T	 8T	 10T	 12T

Table 2 shows a summary of the airfoils tested with the identification label and CAD design of sinusoidal leading-edge.

Airfoil Setup

In order to make the experimental process more efficient, it was desired to have a mounting system that would facilitate the rapid change of airfoil models into the test section due to accessibility concerns. The solution resulted in creating a set of interchangeable leading-edges with a single, “fixed” body. Previously, a dovetail had been added to the leading-edge and body of the airfoil, with a simple slide motion in mind. However, the manufacturing complications that arose from this path resulted detrimental to the problem’s solution. Next, it was decided that a “pin and holes” approach would be a better fit for the issues at hand. The body of the airfoil, which was sectioned at the maximum airfoil thickness, has two pins at each end Figure 18(a). Each leading-edge has two corresponding pin holes (Figure 18(b)). A set screw on the side of the body was also required to fix the position of the body and leading-edge.



Figure 18. (a)Airfoil body and (b)interchangeable leading-edge

Experimental Parameters

For this experimental study, different parameters were varied in order to understand their influence on the aerodynamic performance of the NACA 0010 airfoil with and without leading-edge tubercles. The freestream velocities were varied from 20 m/s to 40 m/s, with their corresponding Reynolds numbers ranging from 201,200 to 351,600. The angle of attack was varied from -6 to 20 degrees.

Experimental Instrumentation

Force Measurements

The wind tunnel facility at UTRGV is equipped with two 9105-TIF-DELTA ATI six-axis force/torque transducers, pictured in Figure 19. These force transducers use silicon strain gages to sense forces with a resolution of 0.0625 N for force measurements and 0.000375N-m for torque measurements. The transducers are positioned on each side of the wind tunnel test section in order to measure the forces being experienced by the airfoil.



Figure 19. (1 of 2) Six-axis force/torque transducer

Calibration. Calibration, by definition, is the act of checking the accuracy and reliability of the instruments being used. In order to calibrate an instrument, the output is compared to a reference measurement, often referred to as the standard. In other words, it is the purpose of the calibration to reduce inaccuracy or bias in the readings output by an instrument over a certain range, using known measurements (Figliola, 2011).

The instruments used for this experimental study were calibrated as follows: Using static calibration process, the two ATI six-axis force/torque transducers were calibrated by subjecting them to known forces. A set of weights ranging from 0 to 20 pounds (0 to 88.964 N) was selected as the standard values.

From the data collected, the direct calibration curve was obtained using MATLAB. Figure 20 shows the force measured by the transducers vs. the standard. From the calibration equation obtained, it can be concluded that there's a small difference between both values. Equation (1) will be used to analyze the results obtained in this experimental study.

$$L = 0.9972F_L - 0.2745 \quad (1)$$

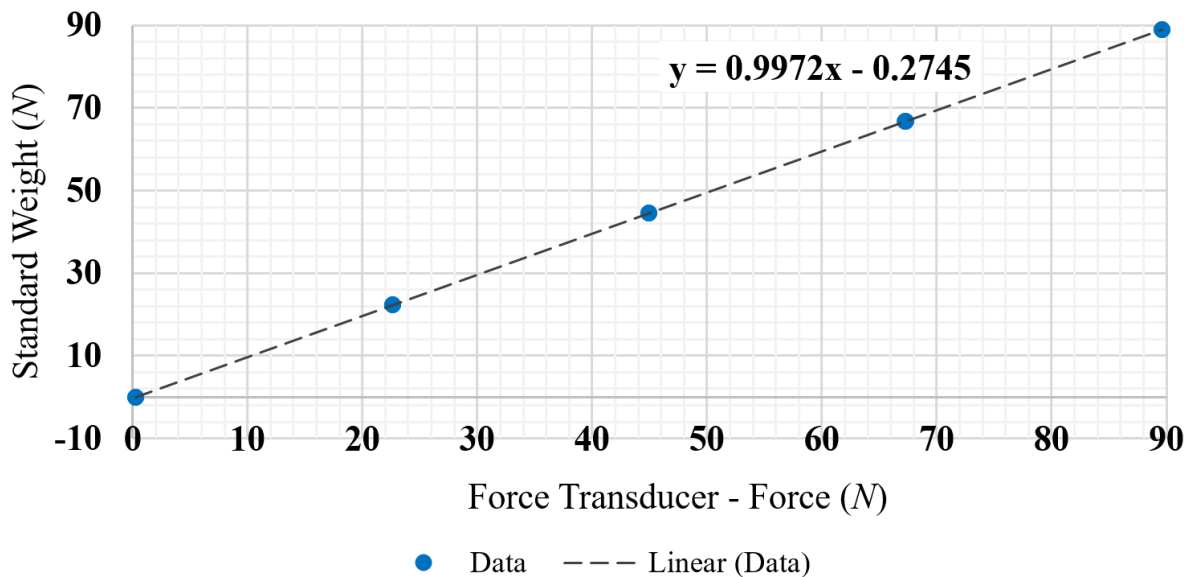


Figure 20. Force transducer calibration

Data Outlier Elimination. Outliers are the points known lie outside of the probability of normal variation (Figliola, 2011). Outliers tend to influence various estimates resulting in fundamental problems. To eliminate outliers, it is possible to use several methods. For this study, Chauvenet's criterion for outlier elimination is used. This approach eliminates those outliers falling outside of the $\frac{1}{2N}$ probability of occurrence.

Using Chauvenet's criterion, a potential outlier is given by

$$(1 - 2 \times P(z_o)) < \frac{1}{2N} \quad (2)$$

where N is the number of values in the data set and $P(z_o)$ is probability value used for the normal error function. The variable $z_o = \left| \frac{x_i - \bar{x}}{s_x} \right|$ where x_i is a potential outlier and s_x is standard deviation of the data set.

Figure 21 shows the analysis performed on one data set of the force transducer measurements. As it can be appreciated, the outliers detected were not significant. The mean of the data after the outlier elimination remained equal up until 5 significant figures.

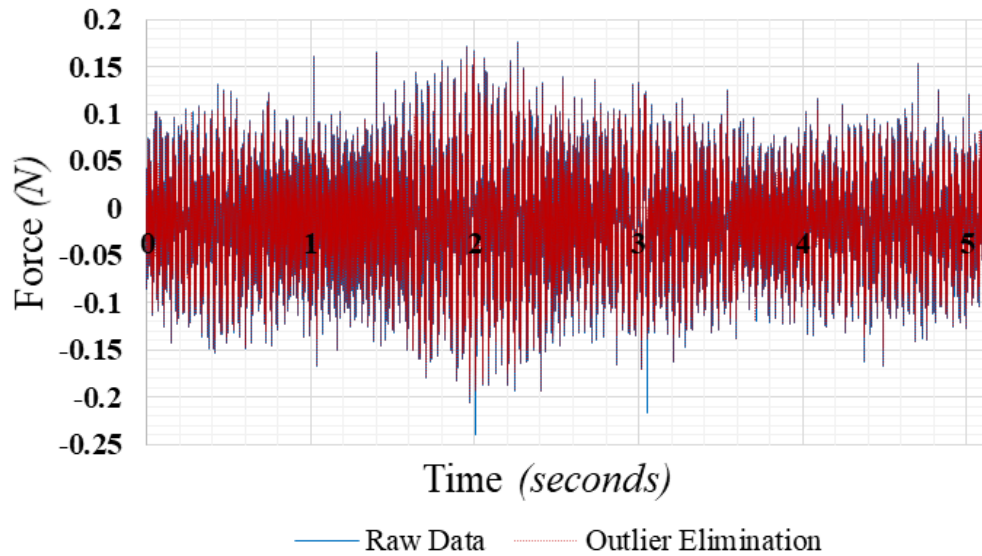


Figure 21. Data outlier elimination performed on data set

Hysteresis Error. The hysteresis error is the difference in the output measurement values when performing an upscale sequential test and a downscale sequential test (Figliola, 2011). That is, for the force transducer, the error in the output data when loading and then unloading the set of weights chosen for the calibration. Figure 22 shows the data obtained. The upscale data is marked with red circle symbols and downscale data with blue star symbols.

The following equation is used to calculate the hysteresis error,

$$\%u_{h_{\max}} = \frac{u_{h_{\max}}}{r_o} * 100 \quad (3)$$

where $u_{h_{\max}}$ is the maximum uncertainty, and r_o is the full-scale output range. The difference in upscale and downscale is given by

$$u_h = (y)_{\text{upscale}} - (y)_{\text{downscale}} \quad (4)$$

From the data obtained, the hysteresis error results in

$$\%u_{h_{\max}} = 1.20\%$$

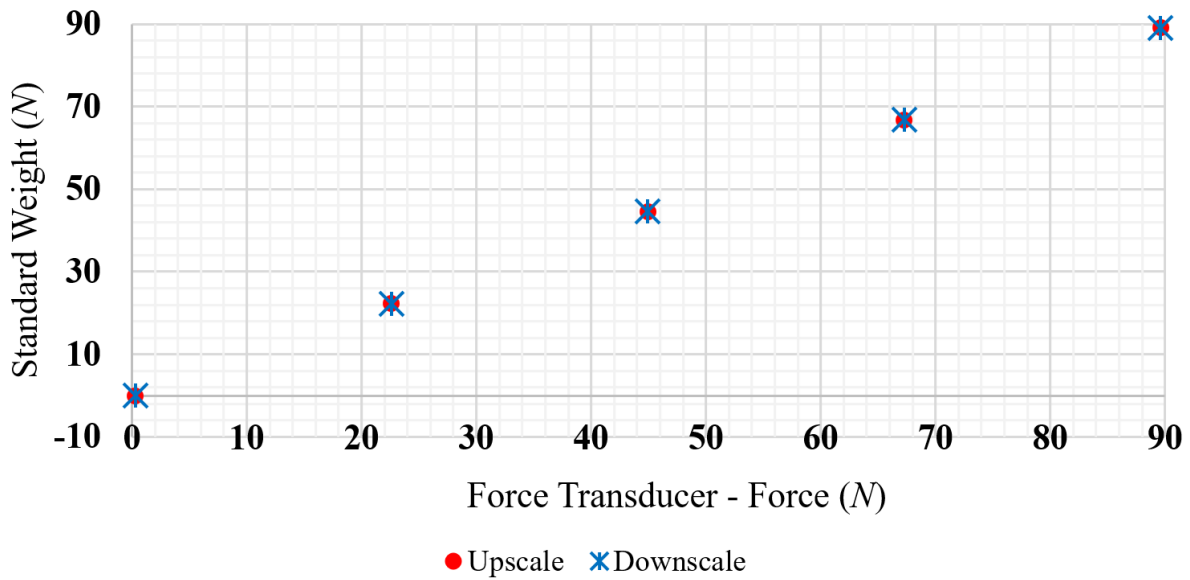


Figure 22. Upscale and downscale sequential test – Hysteresis error

Uncertainty in Force Measurements. Uncertainty analysis is required to obtain the range of error in the measurements obtained for a particular case. The uncertainty of a data set is given within a plus or minus range of the reading, which makes it possible to distinguish the variability of the results when, and if, the experiments were to be repeated (Figliola, 2011). For this study, force measurements obtained by the force transducers are studied to obtain the variability in the data. Four sets of experiments labeled as RUN 1, RUN 2, RUN 3, and RUN 4, respectively, repeated on different days and at different times were used for the purpose of obtaining a better estimate of the variability through pooled statistics. Each of the four repetitions has a total of 102,400 samples. Critical points were selected within the range of angles of attack studied.

The variability calculated from these measurements was obtained as follows: First, the pooled mean is given by

$$\langle \bar{x} \rangle = \frac{\sum_{j=1}^M N_j \bar{x}_j}{\sum_{j=1}^M N_j} \quad (5)$$

where M is number of repetitions, N is number of samples in the j th repetition, and \bar{x}_j is the mean of the j th repetition

Then, the variability between the tests is obtained by the pooled standard deviation,

$$\langle s_x \rangle = \sqrt{\frac{1}{m-1} \sum_{j=1}^M (\bar{x}_j - \langle \bar{x} \rangle)^2} \quad (6)$$

where m is number of repetitions.

Finally, the true mean range is given by,

$$\langle \bar{x} \rangle \pm t_{v,95} \langle s_{\bar{x}} \rangle \quad (7)$$

where $t_{v,95}$ is Student's variable, v are the degrees of freedom ($v = N - 1$), and $\langle s_{\bar{x}} \rangle$ is the pooled standard deviation of the means $\left(\langle s_{\bar{x}} \rangle = \frac{\langle s_x \rangle}{\sqrt{N}} \right)$.

The critical points chosen are three points in the prestall regime (-6, 0, 6 degrees) and one point in the stall (12 degrees) and poststall regime (18 degrees). Figure 23 shows the data sets corresponding to all four runs. When observing all runs performed, there's a significant variation; however, the trend observed in all sets is very similar. This is confirmed by results obtained. Also in Figure 23, the pooled mean with the error bars obtained with Equation (5) for each critical point are presented. From this results, it is possible to observe the variation of the true mean range at 95% confidence level. The possible reasons for this behavior can be further explored by analyzing the frequency domain of the data by means of Fast Fourier Transform Analysis.

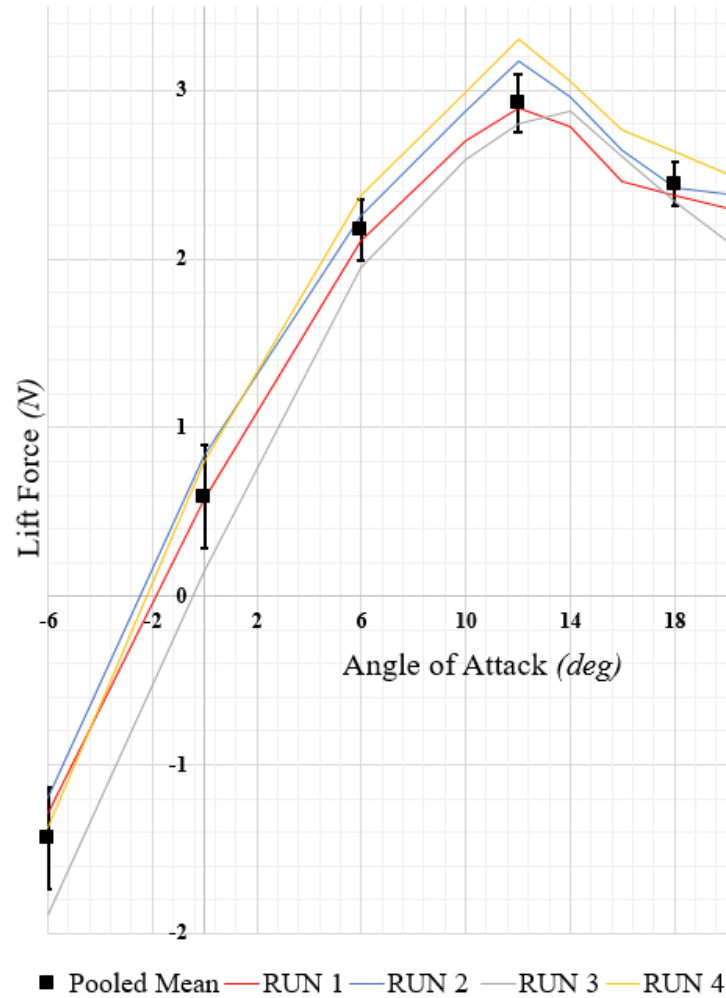


Figure 23. Data set with error bars for critical points

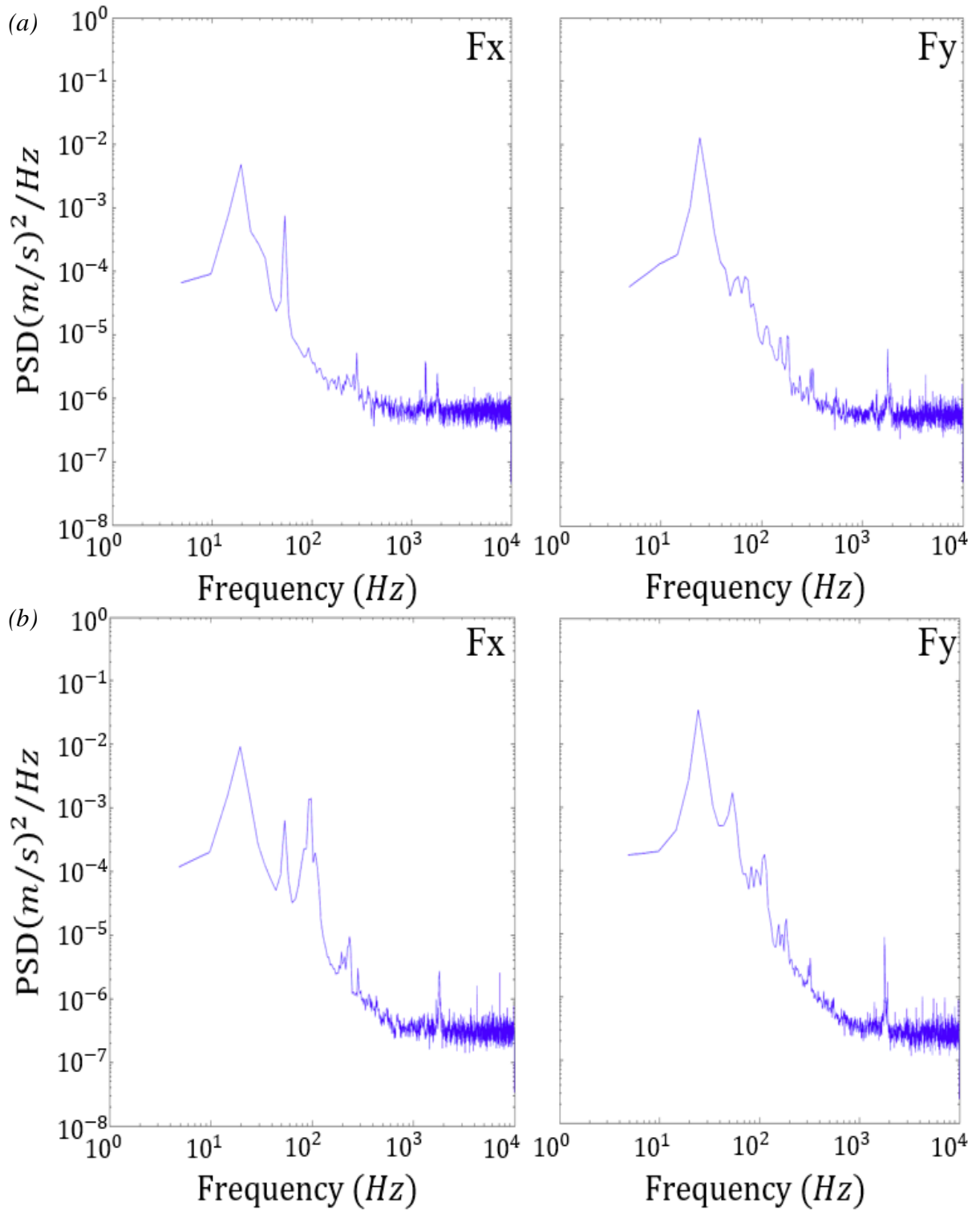


Figure 24. FFT results for force transducer (a) A and (b) B

The fast Fourier transform (FFT) is an algorithm used to compute the Fourier transform, especially when the data set is large. Developed by Cooley and Tukey, this algorithm is widely used (Figliola, 2011). In this section, the FFT is computed with the objective to examine the data obtained by the force transducers in the frequency domain since there's an evident error observed in the repeatability of the experiments.

Figure 24 shows the results obtained for both force transducers, A and B. In later sections, the methodology used to calculate lift with the contributions of both force transducers is explained. At the moment, the only aspect necessary to understand is that each force transducer records three forces (F_x , F_y , and F_z axis) and three moments (M_x , M_y , and M_z). Forces F_x and F_y obtained by both transducers contribute to the lift force, force perpendicular to the freestream flow. For this analysis, only F_x and F_y analyzed.

Through the FFT results, it is possible to show a dominant frequency at 20 Hz, which can be attributed to the wall vibration of the wind tunnel. This frequency is expected since wall vibration is inevitable. However, when observing the FFT performed on the x-component of force transducer A and B, it is possible to identify a difference between both, which could suggest a misalignment issue.

Due to the difficulty in the alignment of the setup currently used at the wind tunnel facility at UTRGV, the proper way to deal with this issue is to use a filter that would eliminate the unwanted frequencies. After doing such, the signal in the frequency domain can be inversed to the time domain. However, with the time restrictions at the time this issue was identified, the approach given at this moment is to understand the uncertainties in the results of the experimental data. For future work, the implementation of a filter should be explored in order to solve any misalignment issues that might concur in future experimentation.

Pressure Measurements

The wind tunnel facility at UTRGV is equipped with two OMEGA PX459-2.5DDU10V high stability, low drift differential pressure transducers (Figure 25(a)) with a voltage output of 0-10 Vdc with an accuracy value is of $\pm 0.05\%$ FS inside the test section. The data output is filtered using a Stanford Research SR640 programmable two-channel low pass filter (Figure 26) with a 200Hz cut-off. A 9116 pneumatic intelligent pressure scanner is also used for pressure measurements with an accuracy of $\pm 0.05\%$ FS. A unique OMEGA-PX319-050A5V absolute pressure transducer (Figure 25(b)) with a voltage output of 0-5 Vdc with an accuracy value of $\pm 0.25\%$ FS is positioned at the inlet of the wind tunnel.

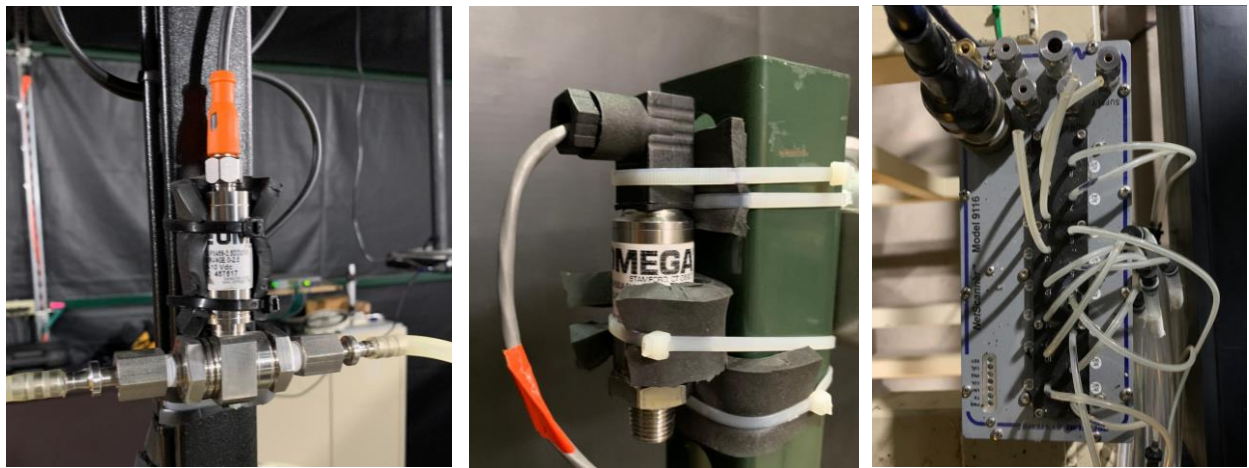


Figure 25. (a) (1 of 2) OMEGA differential pressure transducer (b) OMEGA absolute pressure transducer and (c) 9116 pressure scanner

The facility is equipped with seven pitot tubes and a pitot rake with a transverse motion. Figure 27(a) shows the pitot rake, which holds six pitot tubes. The center probe is connected to the OMEGA PX459 pressure transducer and all outer probes are connected to the pressure scanner (Figure 25). A single pitot tube inside the test section is connected to the second OMEGA PX459, measuring freestream conditions.

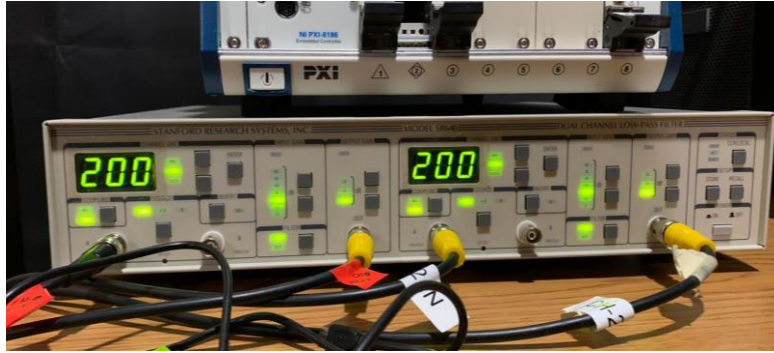


Figure 26. Stanford Research SR640 filter

Pitot tubes measure both the stagnation, or total pressure, through a front hole, and the static pressure, side holes on the probe. By measuring the difference between these two measurements, it is possible to obtain the dynamic pressure. Furthermore, Bernoulli's equation can be used to obtain velocity from pressure measurements in desired positions.

The pitot rake's traverse motion is accomplished by using a VELMEX bi-slide with a 30 inch traverse (Figure 27(b)). By utilizing the bi-slide model, it is possible to perform pressure measurements behind the airfoil in vertical increments. Hence, the wake behind the airfoil can be captured through this method.

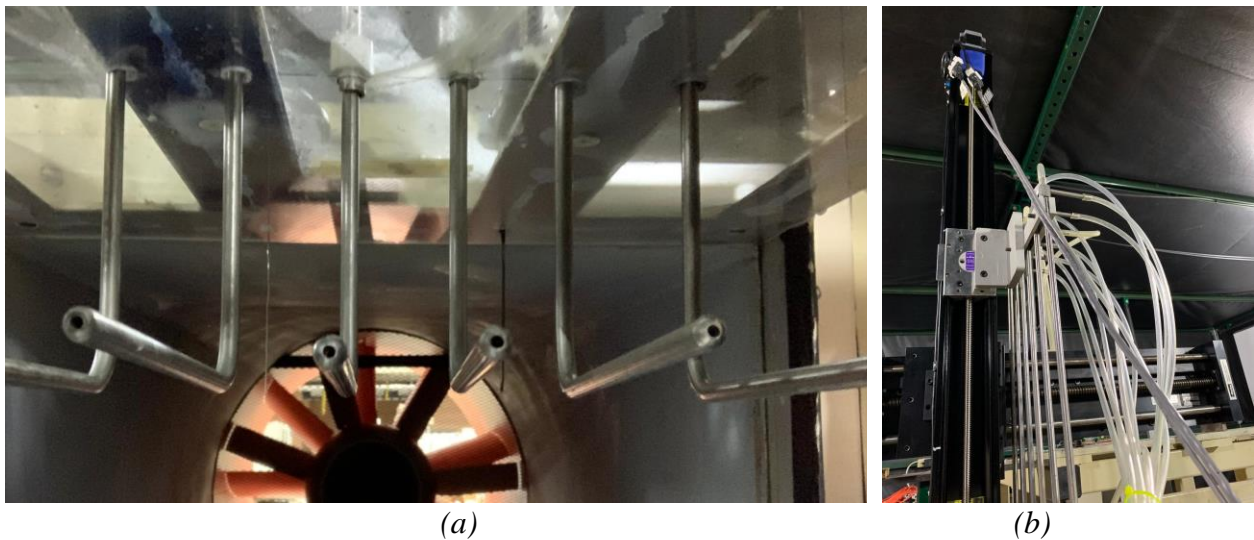


Figure 27. (a) Pitot rake with capacity of six pitot tubes along the width of wind tunnel test section driven by (b) VELMEX bi-slide



Figure 28. (a) Display of test section conditions and (b) linear power supply (LPS) 304

The OMEGA PX459 pressure transducers are connected to process meters that display the immediate pressure measurements inside the wind tunnel test sections (Figure 28(a)). The data measured by the pressure transducers is acquired using a National Instruments NI PCI 6143 data acquisition card. The OMEGA PX319 pressure transducer is powered using a linear power supply LPS 304 (Figure 28(b)). The data measured by this transducer is acquired using a National Instruments NI PCI 6150 data acquisition card.

All data is monitored and recorded using LabVIEW in-house data acquisition programs. For data processing, in-house MATLAB programs are used to analyze and present results obtained for this experimental study.



Figure 29. OMEGA K-type thermocouple

Uncertainty in Velocity Measurements. Following the procedure explained for the force measurements in the previous section, the variability between the tests performed for velocity measurements obtained using the pressure transducers on the pitot rake is also analyzed. Figure 30 shows the velocity obtained for four different runs on different days. The critical points chosen are one in the middle of the wake and two on the upper and lower freestream sections each. There is a significant variation, just as seen for force measurements. However, for pressure measurements, this variation can be partly attributed to the variation in the freestream velocity.

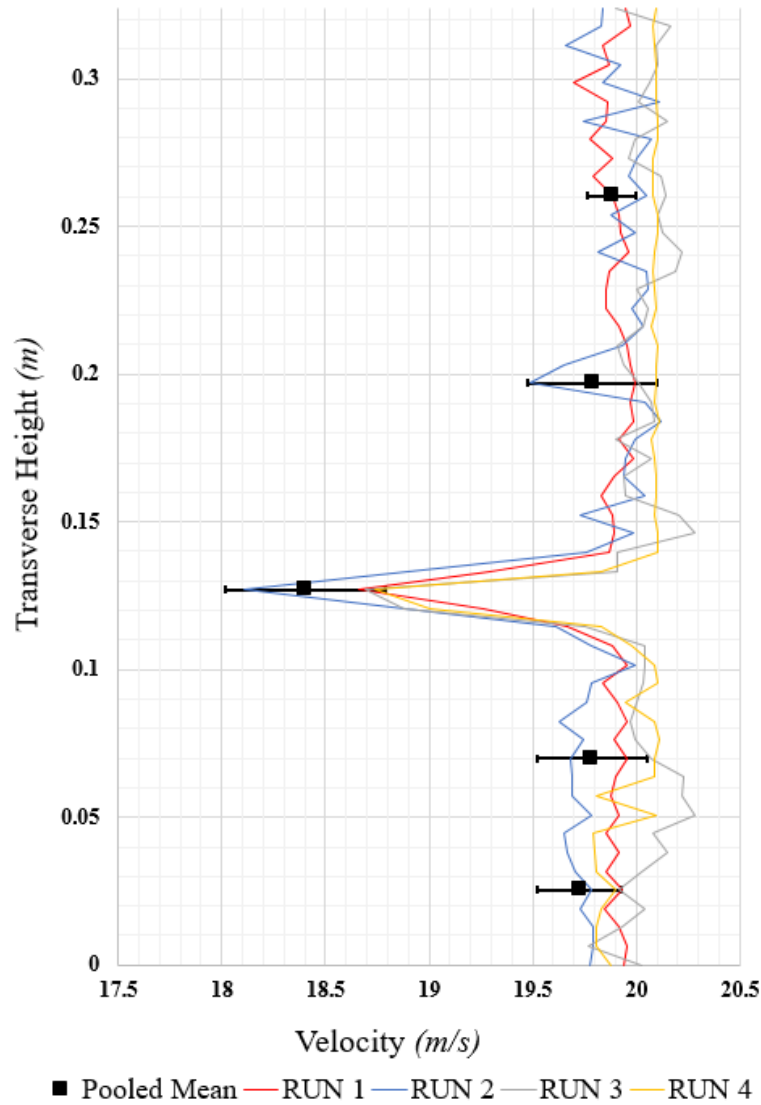


Figure 30. Data set with error bars for critical points

Figure 30 also depicts the pooled mean of the data with bars representing the variation in the true mean range for each critical point in the transverse height. For the critical points in the freestream sections, there are particular cases in which the variation is greater, but in general, the freestream velocity is consistent. For the point taken in the middle of the wake, the greater variation is found. Also, from the results, it is possible to see that one of the runs used for this study experiences the greater variation when compared with the other runs, causing a greater variation overall.

Temperature Measurements

The wind tunnel facility at UTRGV is equipped with an OMEGA K-type thermocouple positioned at inlet of the wind tunnel. The total experimental uncertainty is 2.5°C for a maximum temperature of 300K. Figure 29 shows the OMEGA K-type thermocouple, which is connected to a process meter in order to monitor immediate temperature at the inlet of the wind tunnel. The data obtained from the OMEGA K-type thermocouple is acquired using a National Instruments NI PCI 6143 data acquisition card.



Figure 31. (a) Rotary table and (b) ball bearing fixtures

Angle of Attack Variation

Figure 31(a) shows the VELMEX B4800 Motorized Rotary Table used to properly control the angle of attack of the airfoil. An in-house LabVIEW program is used to specify the angle of attack of the airfoil during experimentation. In order to ensure free rotational motion, the setup required the use of ball bearing fixtures on each end of the wind tunnel. Figure 31(b) shows the two ball bearing fixtures.

Particle Image Velocimetry

For this study, Particle Image Velocimetry is utilized as a flow visualization and velocity measurement technique. The wind tunnel facility at the Aerodynamics and Propulsion Laboratory at UTRGV is equipped with the necessary instrumentation to perform PIV measurements.

The instrumentation utilized for this experimental study is a dual-oscillator 10kHz Nd:YAG laser (DM30-527-DH-PIV Photonics laser) with 30 mJ/pulse (Figure 32). The Nd:YAG laser is used to create a thin laser sheet of about 3mm. Figure 33 shows the laser sheet produced. The laser sheet extends along the chordwise direction and is positioned at the midspan of the airfoils tested.

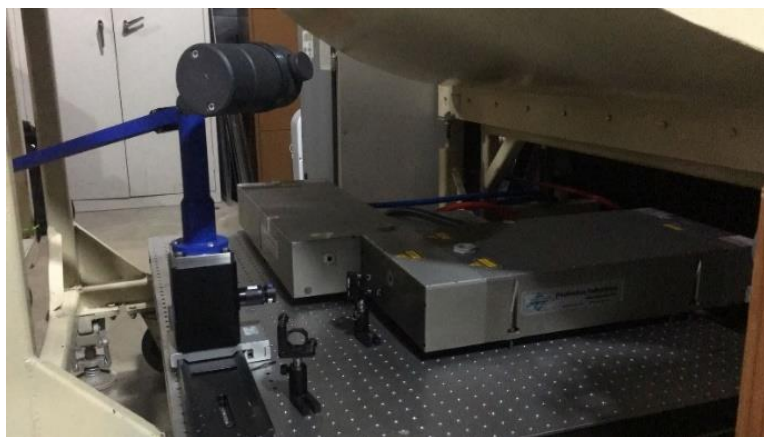


Figure 32. Particle Image Velocimetry setup showing Nd:YAG laser, beam combiner and articulating arm

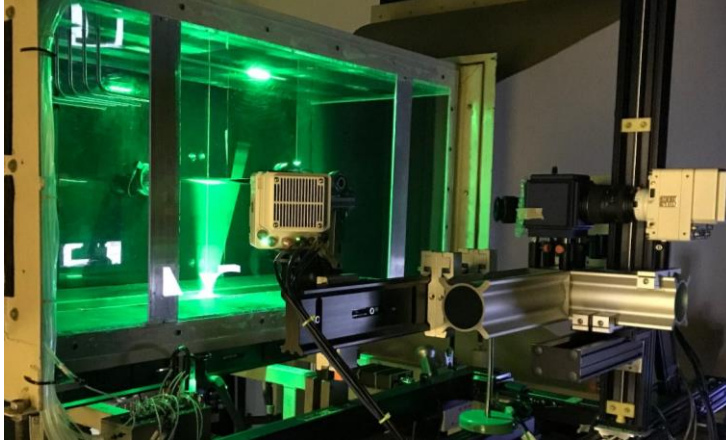


Figure 33. Particle Image Velocimetry setup showing laser sheet and CMOS cameras.

For stereoscopic imaging, two cameras are utilized to capture the particles tracing the fluid. Stereoscopic PIV permits to capture the out-of-plane component of velocity that is neglected in planar PIV. Therefore, in this experimental setup up, there are two CMOS cameras – Phantom VEO 410 L, as seen in Figure 33. These cameras have a resolution of 1280(H) x 800(V) pixels of a size of $20 \times 20 \mu m^2$ and Nikon macro lenses with a focal length of 105mm with a full stop of 2.8. The implementation of a setup structure with a three-degrees of freedom, adjustable position is utilized to aid during the setup, calibration, and execution process of the stereoscopic PIV.

In order to trace the flow, the wind tunnel is seeded with smoke particles with varying diameter from 1 to $10 \mu m$, which are produced using a Rosco fog generator. A total of 1500 image pairs are acquired at the rate of 2.5 kHz with a time delay between two successive images in a pair being $20 \mu s$. For the processing system required for data acquisition and process of data, a computer equipped with LaVision software is utilized specifically for PIV experimentation.

PIV Measurements Data

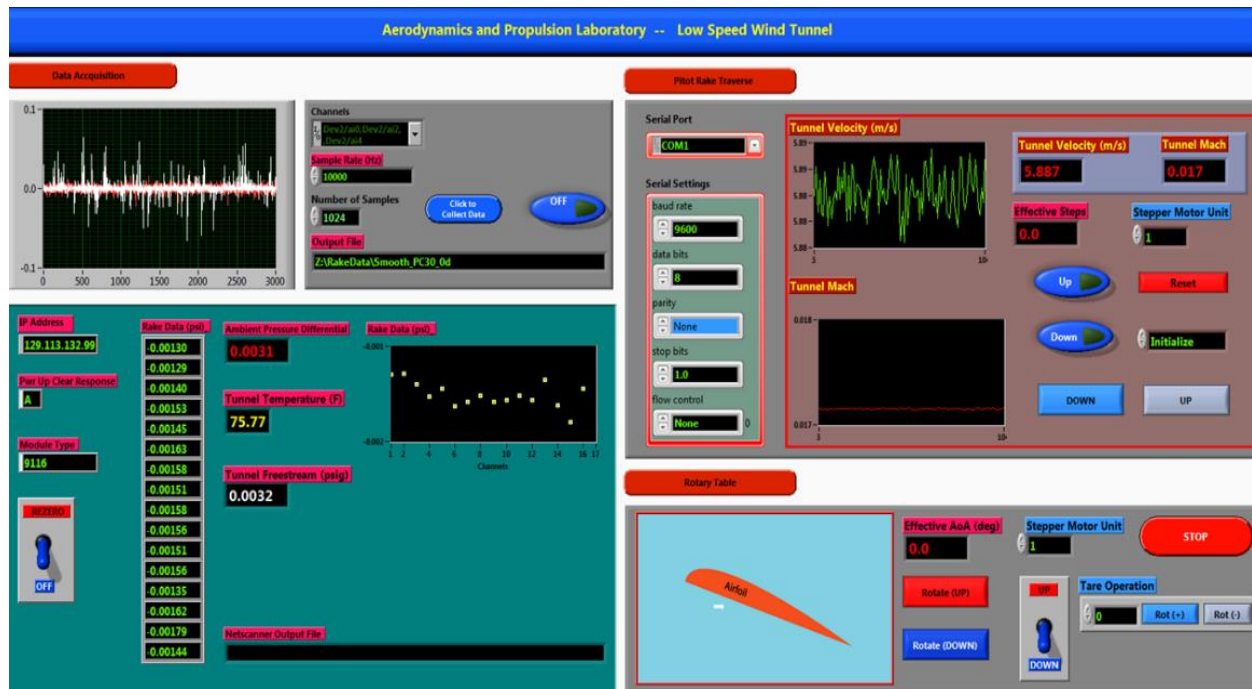
All data captured through the particle image velocimetry experimentations was processed using the commercial LaVision software. Using this program, velocity, vorticity and turbulent kinetic energy contours were obtained.

Data Acquisition

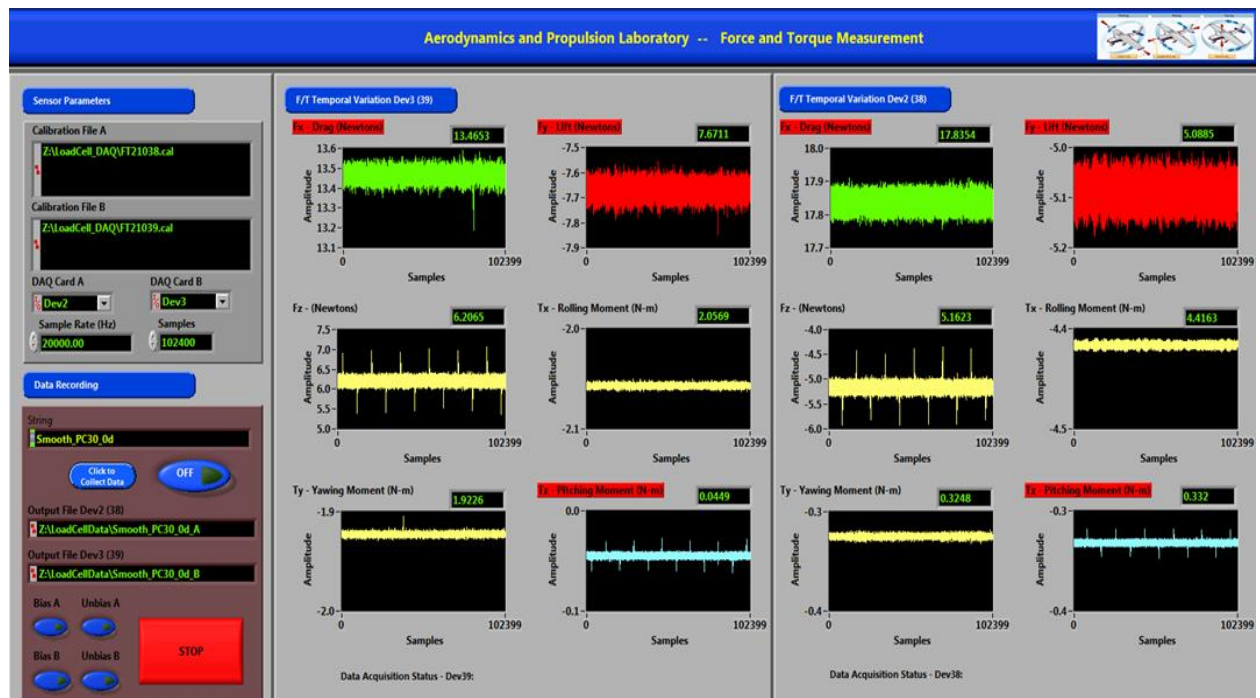
For all experiments performed in this study, two in-house LabVIEW programs are used to acquire data. The first program, pictured in Figure 34(a), used to monitor different parameters such as tunnel velocity and Mach number, ambient pressure differential and tunnel freestream pressure. With this program, the angle of attack of the airfoil is controlled in increments or decrements of two degrees. However, the main purpose of this program is to acquire the data being measured by the pitot rake, freestream pitot tube and thermocouple. By inputting the appropriate name for the file and starting a run, the pitot rake will begin its traverse descend behind the airfoil. Each step is of 0.25 inches. A total of 52 steps is acquired per run in order to better depict the wake behind the airfoil for a total traverse length of 12.75 inches. For each step, 1024 samples are acquired at a sampling frequency of 10,000 Hz. The second program is used to monitor the forces in the x, y, and z direction, as well as their respective moments about the x, y, and z axes. This program is solely used for the acquisition of both ATI force/torque transducers. For each component, 102,400 samples are acquired at a sampling frequency of 20,000 Hz Figure 34(b)).

Experimental Setup

The experimental setup consists of an arrangement of the experimental instrumentation detailed in the previous sections of this chapter. Figure 35(a) shows the schematic of experimental setup utilized for force, pressure, and temperature measurements at the wind tunnel facility. Starting from bottom to top, the airfoil is positioned at the center of the test section. The ATI force/torque transducers are located on each side of the airfoil. There are two ball bearing fixtures to ensure free rotational motion. A VELMEX rotary table is used to control the angle of attach of the airfoil, which is controlled using LabVIEW.

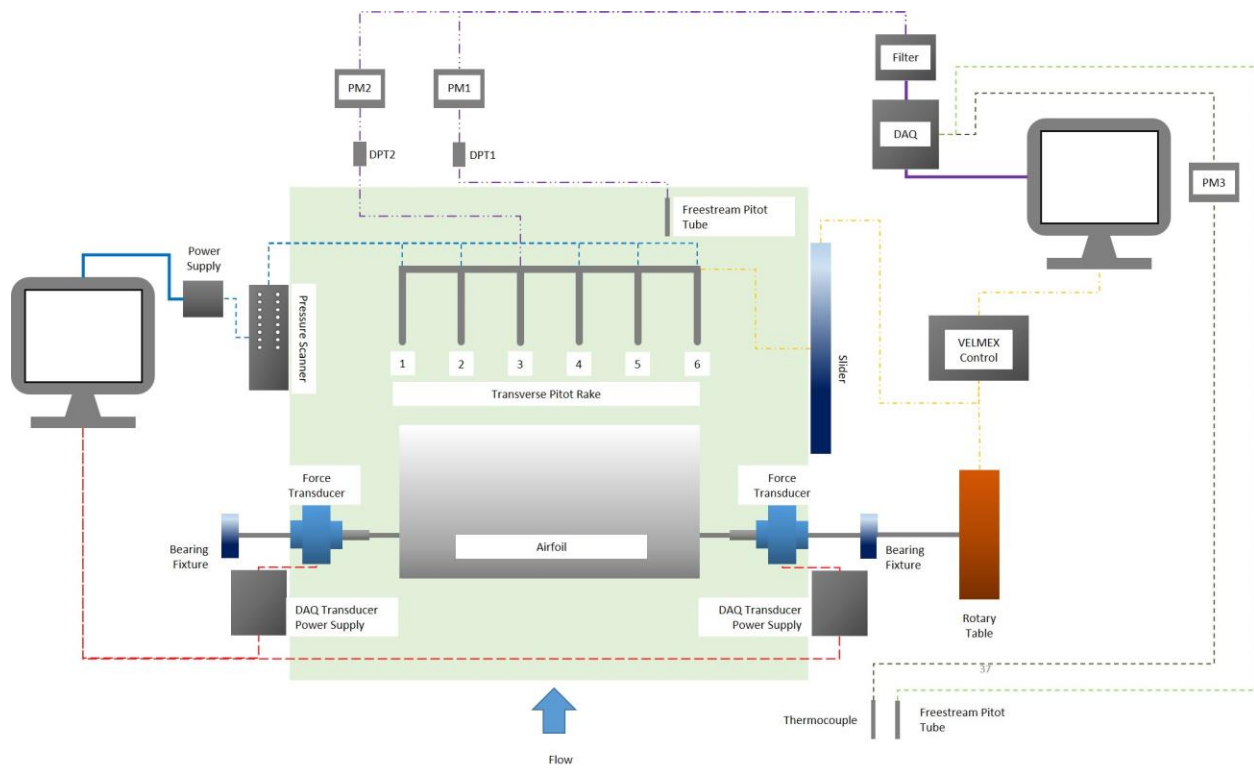


(a)

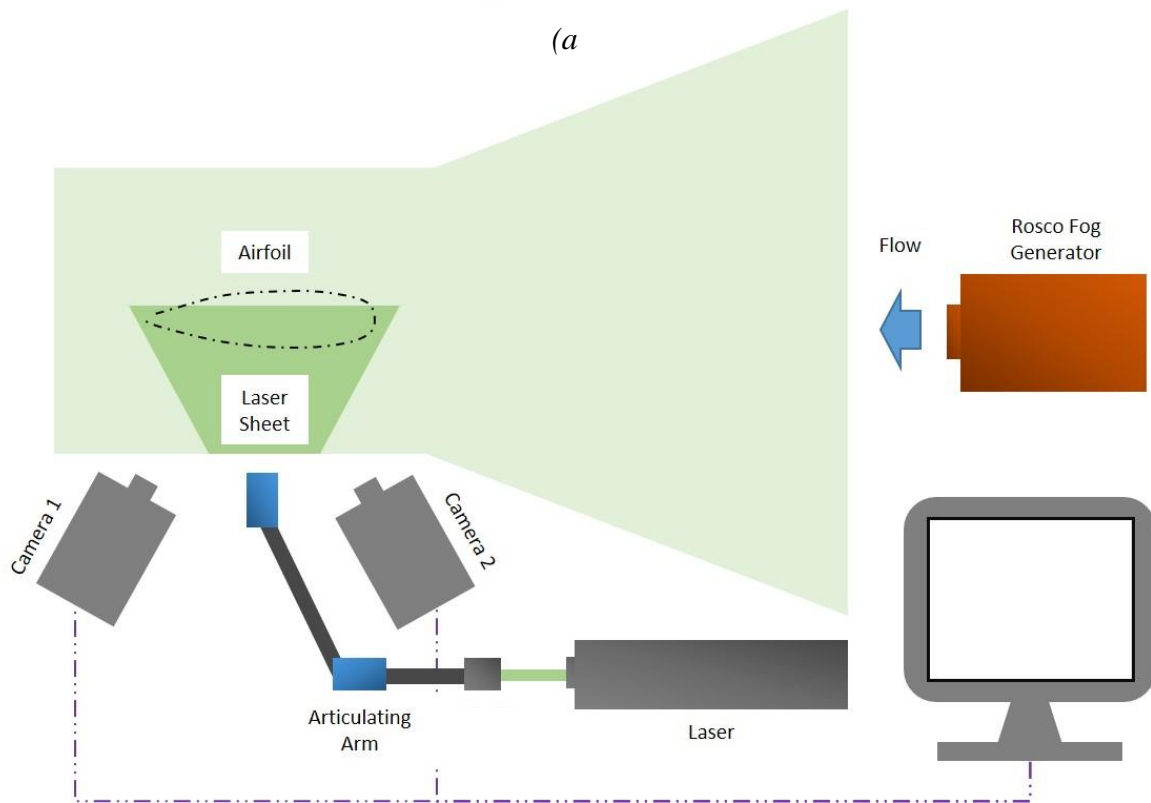


(b)

Figure 34. Data acquisition using LabVIEW – (a) Pressure measurements and (b) force/torque measurements



(a)



(b)

Figure 35. Schematic of (a) pressure, force, and temperature and (b) PIV setup in wind tunnel facility at UTRGV – Edinburg

Behind the airfoil, the pitot rake travels in a traverse motion driven by a VELMEX bi-slide with a 30” traverse. The probes held by the pitot rake are connected to a differential pressure transducer and a pressure scanner. Inside the test section, an OMEGA K-type thermocouple and a pitot tube are positioned to capture freestream parameters, temperature and freestream pressure transducer, respectively. Outside the test section, a gauge pressure transducer is placed to capture total pressure at the wind tunnel facility. Data from all these instruments is acquired using LabVIEW. A display board is part of the experimental setup, where instantaneous measurements are displayed in order to monitor the conditions inside the wind tunnel test section. These process meters also act as power supplies for the pressure transducers.

Figure 35(b) shows the schematic of the PIV setup. Starting from bottom to top, a Nd:YAG laser is used, alongside a beam combiner and an articulating arm to create the appropriate laser sheet inside the wind tunnel’s test section. Two cameras are positioned in front of the test section’s plexiglass wall, facing the side of the airfoil, for stereoscopic imaging for visibility. Information obtained during experimentation is captured and recorded using LaVision. A Rosco fog generator is utilized to see the wind tunnel’s section for particle tracking.

Data Analysis

Lift Coefficient

The lift coefficient is obtained by using the following equation

$$C_L = \frac{L}{\frac{1}{2} \rho V^2 A} \quad (8)$$

where ρ is density, V is freestream velocity, A is planform area, and L is lift force.

The lift force, being the resultant force perpendicular to the direction of the freestream flow, can be obtained from the force measurements. Since the force transducer’s reference frame rotates as the angle of attack is changed, it is necessary to do the proper calculations to obtain the

lift force. Figure 36 illustrates the orientation of the force/torque transducers during experimentation. The force perpendicular to the direction of the freestream flow is calculated with the following equation,

$$F_L = (A_y + B_y) \cos \alpha + (B_x - A_x) \sin \alpha \quad (9)$$

where α is angle of attack, A_x and A_y are the x and y forces recorded by transducer A and B_x , and B_y are the x and y forces recorded by transducer B.

From the calibration process performed in static conditions on the force transducers, the following calibration equation was obtained

$$L = 0.9972F_L - 0.2745 \quad (1)$$

Drag Coefficient

The drag coefficient is calculated using the following equation,

$$C_D = \frac{D}{\frac{1}{2} \rho V^2 A} \quad (10)$$

where ρ is density, V is freestream velocity, A is planform area, and D is drag force. The drag force is the resultant force parallel to the direction of the freestream flow, which can be obtained from the force measurements by the force transducers. However, since force transducers do not capture the momentum deficit due to viscous drag, only the force due to the pressure differential, the drag obtained through this process is called pressure drag. This is one of the subdivisions of total drag. Total drag, on the other hand, can be calculated by integrating the wake velocity profiles. The derivation behind this method is explained below. The drag force obtained through this method will include drag due to flow separation and viscous drag.

Pressure Drag. Similarly to the lift force obtained previously, the pressure drag force is obtained by taking into consideration the rotating reference frame of the transducers. From Figure 36, the force parallel to the direction of the freestream flow can be calculated by

$$F_D = (A_y + B_y) \sin \alpha + (A_x - B_x) \cos \alpha \quad (11)$$

where α is angle of attack, A_x and A_y are the x and y forces recorded by transducer A and B_x , and B_y are the x and y forces recorded by transducer B.

Due to the current setup, the calibration equation obtained in the calibration process of the force transducers pertains only to the lift force. Therefore,

$$D = F_D \quad (12)$$

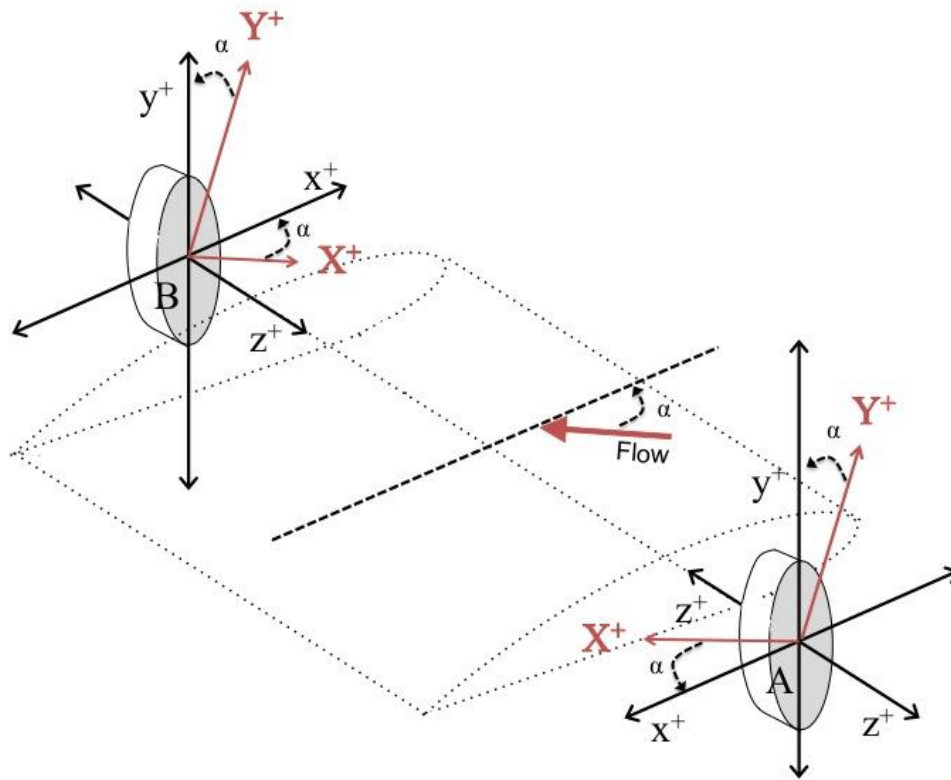


Figure 36. Schematic with local and global axes utilized for force transducers

Total Drag. Total drag is the subdivision of total drag caused by the effects of the boundary layer separation, the wake created behind the object due to this separation and viscous drag. For this experimental study, the integral form of the momentum equation is used to obtain the total drag force per unit acting on the 2D body. A very thorough explanation is found on Anderson's Fundamentals of Aerodynamics (2011), which is the reference used for the following integration.

Considering a two-dimensional body immersed in a fluid, a control volume can be drawn around it. The control volume is bounded by the flow velocities far upstream and downstream of the body and by the streamlines far away from the body, as well as the boundary surrounding the surface of the body.

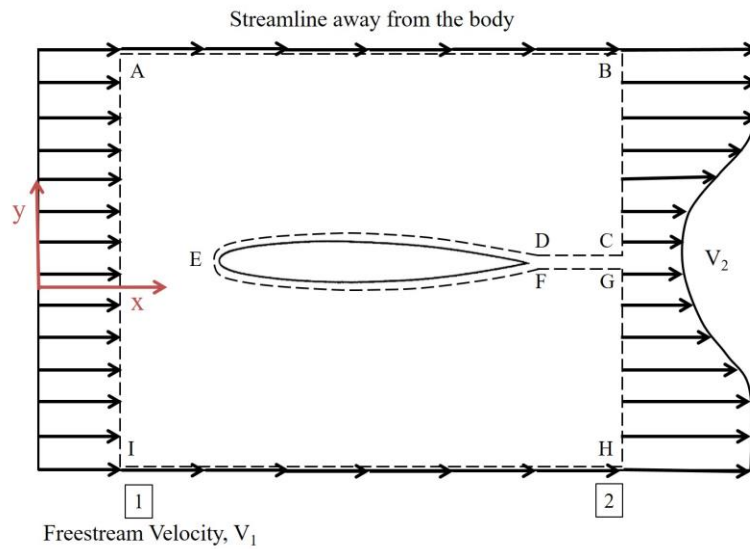


Figure 37. Control volume bounding an airfoil immersed in a fluid flow

Figure 37 represents the control volume ABCDEFGHI. Section 1 corresponds to the inflow conditions; the flow is uniform across the control volume AI with a value of V_1 ($V_1 = \text{constant}$), corresponding to the freestream velocity. On the other hand, section 2 is the outflow conditions; the flow is not uniform across the control volume BH due to the presence of the body in the flow. A wake is created behind the body, and the wake velocity is labeled as V_2 ($V_2 = f(y)$).

In this control volume, the surface forces are due to two sources: the pressure distribution over the surface ABHI and the surface force DEF created by the body's presence in the control volume. For this case, the shear stress distribution on AB and HI is neglected. Also, going back to the control volume in Figure 37, it can be seen that any shear stress or pressure distribution that could arise due to CD and FG, which are equal and opposite, cancel each other.

The aerodynamic forces and moments are created due to two sources, pressure distribution and shear stress distribution over the body surface. As presented in Figure 38, such sources result in the aerodynamic force per unit span R' . According to Newton's third law, the body will exert an equal and opposite force on the control surface DEF.

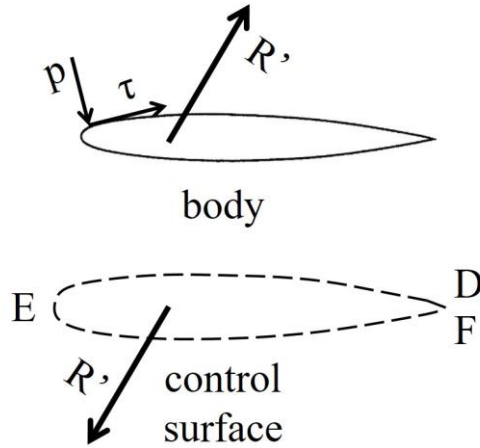


Figure 38. Resultant force on control surface

Therefore,

$$\text{Surface force} = - \iint_{ABHI} p dS - R' \quad (13)$$

where the first term corresponds to the pressure distribution over the surface ABHI and the second term corresponds to the surface force on DEF due to the body.

By taking the momentum equation in integral form

$$\frac{\partial}{\partial t} \iiint_V \rho \mathbf{V} dV + \oint_S (\rho \mathbf{V} \cdot d\mathbf{S}) \mathbf{V} = - \oint_S p d\mathbf{S} + \iiint_V \rho \mathbf{f} dV + \mathbf{F}_{viscous} \quad (14)$$

Since the right-hand side of this equation is the total force experienced by the fluid as it passes through the control volume, it can simply be substituted by the total force obtained in Equation (13) since the volumetric body force is negligible.

Equation (14) becomes

$$\frac{\partial}{\partial t} \iiint_V \rho \mathbf{V} dV + \oint_S (\rho \mathbf{V} \cdot d\mathbf{S}) \mathbf{V} = - \iint_{ABHI} p d\mathbf{S} - \mathbf{R}' \quad (15)$$

If steady flow is assumed, then Equation (15) becomes

$$\mathbf{R}' = - \iint_{ABHI} p d\mathbf{S} - \oint_S (\rho \mathbf{V} \cdot d\mathbf{S}) \mathbf{V} \quad (16)$$

which is a vector equation.

By considering only the x-component of Equation (16) using Figure 37, velocities can be noted as V_1 and V_2 and the force as D' , which is the x-component of force \mathbf{R}' , drag per unit span.

Therefore,

$$D' = - \iint_{ABHI} (pdS)_x - \oint_S (\rho \mathbf{V} \cdot d\mathbf{S}) V_x \quad (17)$$

As was noted before, the control volume ABHI is chosen far away from the body. This is important since it allows us to assume the pressure constant along the boundaries, $p = p_\infty$. This assumption balances the pressure forces. Therefore,

$$\iint_{ABHI} (pdS)_x = 0 \quad (18)$$

Hence, Equation (17) becomes,

$$D' = - \oint\oint_S (\rho \mathbf{V} \cdot d\mathbf{S}) V \quad (19)$$

Now, Equation (19) can be evaluated. Using Figure 37, it is stated that the only contributions to the integral come from sections AI and BH. Therefore,

$$\oint\oint_S (\rho \mathbf{V} \cdot d\mathbf{S}) V = - \int_I^A \rho_1 V_1^2 dy + \int_H^B \rho_2 V_2^2 dy \quad (20)$$

Now, before going any further, let's consider the integral form of the continuity equation for steady flow:

$$\oint\oint_S \rho \mathbf{V} \cdot d\mathbf{S} = 0 \quad (21)$$

Applying this equation to the control volume in Figure 37, Equation (21) becomes,

$$- \int_I^A \rho_1 V_1 dy + \int_H^B \rho_2 V_2 dy = 0 \quad (22)$$

After manipulating, Equation (22) becomes,

$$\int_I^A \rho_1 V_1^2 dy = \int_H^B \rho_2 V_2 V_1 dy \quad (23)$$

Equation (23) can be substituted into Equation (20). Therefore, Equation (20) becomes,

$$\oint\oint_S (\rho \mathbf{V} \cdot d\mathbf{S}) V = - \int_H^B \rho_2 V_2 (V_1 - V_2) dy \quad (24)$$

Further substitution into Equation (19). Equation (19) becomes

$$D' = \int_H^B \rho_2 V_2 (V_1 - V_2) dy \quad (25)$$

For incompressible flow, density is constant. Therefore Equation (25) becomes

$$D' = \rho \int_H^B V_2 (V_1 - V_2) dy \quad (26)$$

where ρ is density, V_1 is freestream velocity, V_2 is velocity behind the airfoil, or the wake velocity.

From this analysis, the wake velocity profiles obtained through the pressure measurements behind the airfoil can be used to calculate the total drag per unit force using Equation (26).

As a consequent step, the total drag per unit span can be multiplied by the span length in order to obtain the total drag force.

CHAPTER III

SOURCE - VORTEX PANEL METHOD

Introduction

The potential flow around a two-dimensional oval shape, which is known as the Rankine oval, results from the superposition of a source and a sink in the x-axis and a uniform flow. From this, it has been demonstrated that it is possible to model the potential flow around a body with the superposition of singularities in the body's interior. However, with this approach, only particular cases can be generated. In order to apply the potential flow theory on arbitrary bodies, such as an airfoil, another approach arises (Cummings *et al.*, 2015; Erikson, 1990)

Developed by Hess and Smith at Douglas Aircraft, panel methods use the distribution of singularities with unknown strength over portions of the surface body, called panels. These numerical methods are specifically used to solve linear, inviscid and irrotational flows over a body. The physical meaning of these conditions is that important flow behaviors such as separation, skin-friction drag, and transonic shocks cannot be predicted solely with panel methods. However, what can be predicted is pressure distribution and lift, two parameters that are of interest for this study (Erikson, 1990).

A classification based on the strength of the singularity gives rise to two categories: lower-order and higher-order panel methods. Lower-order methods use constant-strength singularity distributions over the panel, and higher-order methods use higher order, such as linear or quadratic singularity distributions. Some of the advantages of using lower-order codes are less

amount of computational time that takes to derive the influence coefficient equations, which will be explained in the next section, and coding implementation is simpler than that of higher-order, less arithmetic operation (Hess *et al.*, 1967; Erikson, 1990). For this study, lower-order panel methods are explored due to the simplicity of the geometry of the airfoil.

As mentioned before, the viscous effects are being neglected, which causes the numerical solutions to the equations solved by the panel methods to be non-unique. In order to have a unique solution, a Kutta condition is imposed at the trailing edge. There are different ways in which the Kutta condition can be imposed (Anderson, 2011; Hess *et al.*, 1967; Bertin *et al.*, 2014). For this study, the condition that will be used is forcing the velocity magnitudes at the trailing edge, both upper and lower panels, to approach the same value.

Another condition that has to be satisfied is that of flow tangency, no flow going through the surface of the body. In this condition, boundary conditions are assigned at the control point of each panel in which the normal component of velocity is equal to zero. In this way, the flow is tangent to the surface of the body.

Up to date, there are different panel codes with different features attributed to each of them. There are codes that specifically handle subsonic flows and others that only handle supersonic flows. Some of the subsonic-only panel codes are the lower-order Hess code (or Douglas-Neumann code), MCAERO, SOUSSA, VSAERO, LEV, and the higher-order Hess code (Erikson, 1990).

In the following sections, the source and vortex panel method are explained in detail.. Then, the implementation of the source – vortex panel method using MATLAB is described in detail. The MATLAB code is found in Appendix A. Finally, pressure distribution and lift coefficient results obtained using this computational method are presented.

Procedure

Even though the distribution of only vortices over the panels can be utilized to model lifting flows, in order to properly satisfy all the conditions required to implement the panel method, the distribution of sources and vortices is chosen for this study. The reason behind this decision is explained in the following sections. Consequently, the procedure necessary to solve for non-lifting flows utilizing only distribution of sources is explained first.

Source Panel Method

Starting with non-lifting flows over arbitrary bodies, the source panel method is implemented by superimposing the disturbed flow around the body (by distributing sources over the panels) and the uniform flow in which the body is placed to obtain the total velocity potential,

$$\Phi = Ux + \phi \quad (27)$$

where U is the uniform flow speed and ϕ is disturbance potential.

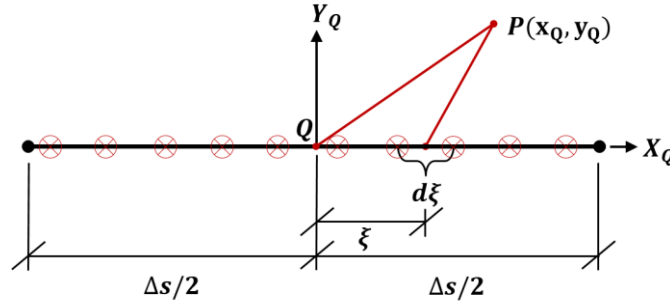


Figure 39. Coordinate system in terms of Q

As mentioned, the disturbance potential can be modeled using a distribution of sources, hence source panel method, over the surface of the body (Houghton *et al.*, 2013). By choosing the source strength per unit length to be represented by σ_Q and the schematic from Figure 39, the velocity potential at P due to sources on the chosen length ds_Q can be represented by

$$\phi_{PQ} = \sigma_Q \ln R_{PQ} ds_Q \quad (28)$$

By integrating Equation (28) over the entire surface of the body, the velocity potential due to all of the sources on the surface is then given by

$$\Phi_P = Ux + \oint \sigma_Q \ln R_{PQ} ds_Q \quad (29)$$

After discretizing the surface of the body, as shown on Figure 40(a), it is necessary to identify all nodes and panels. The collocation points must be chosen accordingly, as well.

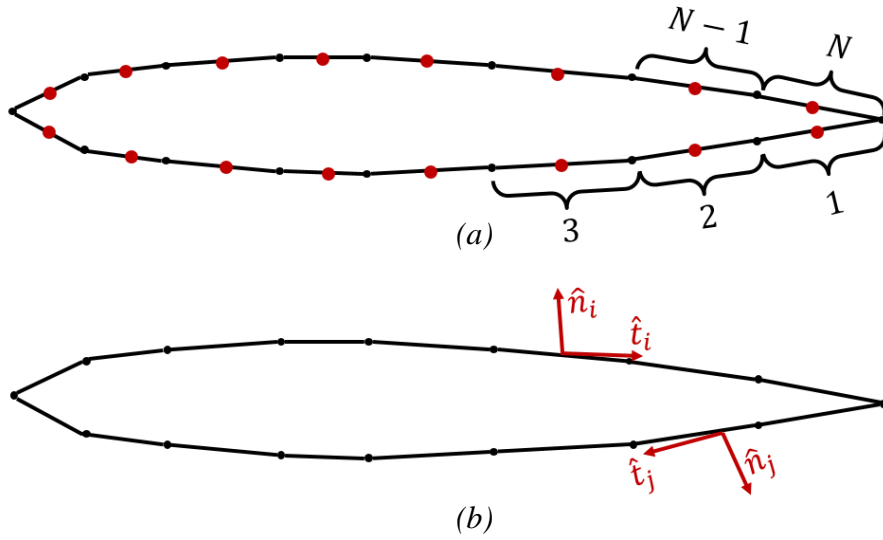


Figure 40. (a) Discretization of airfoil surface into panels and (b) tangent and normal unit vectors

From Figure 40(b), panels i and j can be identified. The sources distributed over panel j induce a velocity at the collocation point of panel i , which is represented by \mathbf{v}_{ij} . The normal and tangential components of \mathbf{v}_{ij} result from the following expressions,

$$\mathbf{v}_{ij} \cdot \hat{n}_i \text{ and } \mathbf{v}_{ij} \cdot \hat{t}_i \quad (30)$$

where \hat{n}_i and \hat{t}_i are the unit normal and tangential vectors, as shown on Figure 40. Equations (30) are established to be proportional to the sources' strength on panel j . Therefore,

$$\mathbf{v}_{ij} \cdot \hat{n}_i = \sigma_j N_{ij} \text{ and } \mathbf{v}_{ij} \cdot \hat{t}_i = \sigma_j T_{ij} \quad (31)$$

where N_{ij} and T_{ij} are the normal and tangential velocities induced due to the panel j at the collocation point of panel i . N_{ij} and T_{ij} are the normal and tangential influence coefficients mentioned earlier. These parameters are the bases of panel methods.

From Figure 39, in a coordinate system (x_Q, y_Q) , N_{ij} and T_{ij} can be obtained by the dot products $N_{ij} = \mathbf{v}_{PQ} \cdot \hat{n}_i$ and $T_{ij} = \mathbf{v}_{PQ} \cdot \hat{t}_i$, respectively, where \mathbf{v}_{PQ} is the velocity induced at point P by sources of unit strength distributed over the panel with a collocation point Q,

$$\mathbf{v}_{PQ} = v_{x_Q} \hat{t}_j + v_{y_Q} \hat{n}_j \quad (32)$$

In order to obtain the components of velocity at P in the specified coordinate system, the disturbance potential comes in handy. The disturbance potential over the entire panel is given by

$$\phi_{PQ} = \int_{-\Delta s/2}^{\Delta s/2} \ln \sqrt{(x_Q - \xi)^2 + y_Q^2} d\xi \quad (33)$$

Therefore,

$$v_{x_Q} = \frac{\delta \phi_{PQ}}{\delta x_Q} = \int_{-\Delta s/2}^{\Delta s/2} \frac{x_Q - \xi}{(x_Q - \xi)^2 + y_Q^2} d\xi = -\frac{1}{2} \ln \left[\frac{(x_Q + \Delta s/2)^2 + y_Q^2}{(x_Q - \Delta s/2)^2 + y_Q^2} \right] \quad (34)$$

$$v_{y_Q} = \frac{\delta \phi_{PQ}}{\delta y_Q} = \int_{-\Delta s/2}^{\Delta s/2} \frac{y_Q}{(x_Q - \xi)^2 + y_Q^2} d\xi = - \left[\tan^{-1} \left(\frac{x_Q + \frac{\Delta s}{2}}{y_Q} \right) - \tan^{-1} \left(\frac{x_Q - \frac{\Delta s}{2}}{y_Q} \right) \right] \quad (35)$$

Now, it is possible to obtain the influence coefficients,

$$N_{ij} = \mathbf{v}_{PQ} \cdot \hat{n}_i = v_{x_Q} \hat{n}_i \cdot \hat{t}_j + v_{y_Q} \hat{n}_i \cdot \hat{n}_j \quad (36)$$

$$T_{ij} = \mathbf{v}_{PQ} \cdot \hat{t}_i = v_{x_Q} \hat{t}_i \cdot \hat{t}_j + v_{y_Q} \hat{t}_i \cdot \hat{n}_j \quad (37)$$

In order to obtain the total velocity normal to the surface at collocation point i , it is necessary to sum the induced normal velocities due to each of the N panels and the freestream at

collocation point i . The total velocity tangential to the surface at collocation point i is found similarly. The total velocity normal and tangential to the surface at collocation point i are

$$v_{n_i} = \sum_{j=1}^N \sigma_j N_{ij} + \vec{U} \cdot \hat{n}_i \quad (38)$$

and

$$v_{s_i} = \sum_{j=1}^N \sigma_j T_{ij} + \vec{U} \cdot \hat{t}_i, \quad (39)$$

respectively.

Referring back to the boundary conditions necessary for the panel method, it is specified that the total normal velocity at each collocation point must equal to zero, $v_{n_i} = 0$ (the body contour is a streamline of the flow).

Therefore,

$$\sum_{j=1}^N \sigma_j N_{ij} = -\vec{U} \cdot \hat{n}_i \quad (i = 1, 2, \dots, N) \quad (40)$$

Equation (40) is a system of linear algebraic equations with N unknowns, the source strengths, $\sigma_i (i = 1, 2, \dots, N)$, of the form

$$\mathbf{N}\sigma = \mathbf{b} \quad (41)$$

Once the elements for \mathbf{N} and \mathbf{b} have been calculated, the system of equations can be solved to obtain the source strengths σ . Then, after calculating the elements for T_{ij} , the known source strengths σ can be used to obtain the total tangential velocity, Equation (39). Finally, Bernoulli's equation can then be used to calculate the pressure distribution acting on the surface of the arbitrary body. The pressure coefficient equation is then,

$$C_{p_i} = 1 - \left(\frac{v_{s_i}}{U} \right)^2 \quad (42)$$

Source - Vortex Panel Method

In order to extend the previous analysis to lifting flows over arbitrary bodies, vortices are distributed along the panels to introduce the vorticity necessary to generate circulation for the production of lift. The vortex distribution over the panels gives each of the N panels a vortex with uniform strength per unit length $\gamma_i (i = 1, 2, \dots, N)$, which varies from one panel to another.

The two necessary conditions to properly model the flow over the NACA 0010 utilizing panel methods are imposed. The first one is flow tangency. As for the source method, this condition is imposed at the collocation points by establishing that $v_{n_i} = 0$. This results in N conditions. Then, the Kutta condition must also be satisfied, which will give us uniqueness in the solution.

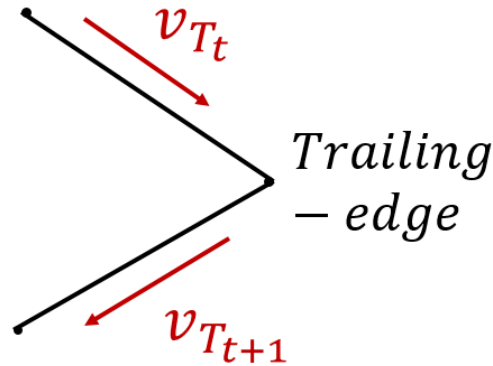


Figure 41. Velocities on the upper and lower surface at the trailing edge

As it was mentioned before, there are various ways in which the Kutta condition can be satisfied. For this study, the condition that is implemented is that of establishing that the magnitudes on the upper and lower surfaces to approach the same value, as shown in Figure 41. This condition requires that

$$\gamma_t = -\gamma_{t+1} \quad (43)$$

Once the Kutta condition has been established, it is possible to notice that the system of linear algebraic equations becomes overdetermined since there are now $N + 1$ conditions to be satisfied with only N unknowns due to only vortices of unknown strength γ being distributed over the N panels. In order to solve this issue, a rather direct solution is to ignore the condition that required the normal velocity to be equal to zero for one of the collocation points. This approach is used widely. However, it is important to take into account that there is no real understanding as of which panel should be ignored for this approach. Ignoring different panels results in different solutions (Bertin *et al.*, 2014; Houghton *et al.*, 2013; Kuethe *et al.*, 1998).

An alternative approach, which is utilized for this study, is to distribute both sources and vortices over each of the panels. In this case, the sources strength σ is chosen so it varies from panel to panel $\sigma_i (i = 1, 2, \dots, N)$, and the vortex strength is chosen so it does not vary now from panel to panel $\gamma_i = \gamma (i = 1, 2, \dots, N)$. By distributing sources and vortices to each of the panels, this approach results in $N + 1$ unknown singularity strengths to match the $N + 1$ conditions that were mentioned before.

In order to find the strength of the sources, the same procedure is followed as it was mentioned previously for non-lifting flows to obtain the influence coefficients N_{ij} and T_{ij} . This results in a $N \times N$ matrix.

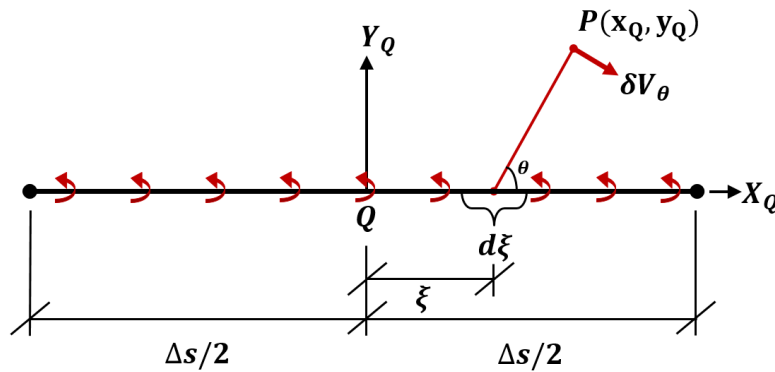


Figure 42. Coordinate system in terms of Q

For the strength of the vortices, since it was specified that the vortex strength does not vary from panel to panel, a $N + 1$ column is added to the influence coefficient matrices that contains the normal and tangential components of velocity induced due to vortex distributions on all of the panels at collocation point i . Hence,

$$N_{i,N+1} = \sum_{j=1}^N N'_{ij} \quad (44)$$

$$T_{i,N+1} = \sum_{j=1}^N T'_{ij} \quad (45)$$

N'_{ij} and T'_{ij} are the influence coefficients for the vortex panel method. In terms of the coordinate system (x_Q, y_Q) shown in Figure 42, the influence coefficients are obtained as follows by the dot products $N'_{ij} = \mathbf{V}_{PQ} \cdot \hat{n}_i$ and $T'_{ij} = \mathbf{V}_{PQ} \cdot \hat{t}_i$, respectively. \mathbf{V}_{PQ} is the velocity induced at point P by sources of unit strength distributed over the panel with a collocation point Q.

Similarly, as presented in Equation (32),

$$\mathbf{V}_{PQ} = V_{x_Q} \hat{t}_j + V_{y_Q} \hat{n}_j \quad (46)$$

Figure 42 shows the distribution of vortices on an element of length $\delta\xi$. The velocity due to such vortices at point P is given by

$$\delta V_\theta = \frac{\gamma}{R} d\xi \quad (47)$$

where R is the distance from P to Q . Hence, from Figure 42, R is calculated as follows,

$$R = \sqrt{(x_Q - \xi)^2 + y_Q^2} \quad (48)$$

The velocity components of δV_θ in a coordinate system (x_Q, y_Q) are found by,

$$\delta V_{x_Q} = \delta V_\theta \sin \theta = \frac{\gamma y_Q}{(x_Q - \xi)^2 + y_Q^2} \delta \xi \quad (49)$$

$$\delta V_{y_Q} = -\delta V_\theta \cos \theta = -\frac{\gamma(x_Q - \xi)}{(x_Q - \xi)^2 + y_Q^2} d\xi \quad (50)$$

The velocity components at P due to the distribution of vortices on a panel of length S is found by integrating along the panel is

$$V_{x_Q} = \gamma \int_{-\Delta s/2}^{\Delta s/2} \frac{y_Q}{(x_Q - \xi)^2 + y_Q^2} d\xi = -\gamma \left[\tan^{-1} \left(\frac{x_Q + \frac{\Delta s}{2}}{y_Q} \right) - \tan^{-1} \left(\frac{x_Q - \frac{\Delta s}{2}}{y_Q} \right) \right] \quad (51)$$

$$V_{y_Q} = -\gamma \int_{-\frac{\Delta s}{2}}^{\frac{\Delta s}{2}} \frac{x_Q - \xi}{(x_Q - \xi)^2 + y_Q^2} d\xi = \frac{\gamma}{2} \ln \left[\frac{(x_Q + \Delta s/2)^2 + y_Q^2}{(x_Q - \Delta s/2)^2 + y_Q^2} \right] \quad (52)$$

By setting $\gamma = 1$, the influence coefficients N'_{ij} and T'_{ij} are then given by

$$N'_{ij} = \mathbf{V}_{PQ} \cdot \hat{\mathbf{n}}_i = V_{x_Q} \hat{\mathbf{n}}_i \cdot \hat{\mathbf{t}}_j + V_{y_Q} \hat{\mathbf{n}}_i \cdot \hat{\mathbf{n}}_j \quad (53)$$

$$T'_{ij} = \mathbf{V}_{PQ} \cdot \hat{\mathbf{t}}_i = V_{x_Q} \hat{\mathbf{t}}_i \cdot \hat{\mathbf{t}}_j + V_{y_Q} \hat{\mathbf{t}}_i \cdot \hat{\mathbf{n}}_j \quad (54)$$

For ease of calculation, it can be noted that Equation (34) and Equation (35) from the source panel method and Equations (51) and Equation (52) from the vortex panel method can be compared as follows,

$$V_{x_Q} = v_{y_Q} \text{ and } V_{y_Q} = -v_{x_Q} \quad (55)$$

The influence coefficients N'_{ij} and T'_{ij} can be expressed in terms of N_{ij} and T_{ij} as,

$$N'_{ij} = v_{y_Q} \hat{\mathbf{n}}_i \cdot \hat{\mathbf{t}}_j - v_{x_Q} \hat{\mathbf{n}}_i \cdot \hat{\mathbf{n}}_j \quad (56)$$

$$T'_{ij} = v_{y_Q} \hat{\mathbf{t}}_i \cdot \hat{\mathbf{t}}_j - v_{x_Q} \hat{\mathbf{t}}_i \cdot \hat{\mathbf{n}}_j \quad (57)$$

Therefore, Equation (44) and Equation (45) can be written as

$$N_{i,N+1} = \sum_{j=1}^N (v_{y_Q} \hat{n}_i \cdot \hat{t}_j - v_{x_Q} \hat{n}_i \cdot \hat{n}_j) \quad (58)$$

$$T_{i,N+1} = \sum_{j=1}^N (v_{y_Q} \hat{t}_i \cdot \hat{t}_j - v_{x_Q} \hat{t}_i \cdot \hat{n}_j) \quad (59)$$

Similarly as in the source panel method, the total velocity normal and tangential to the surface at collocation point i are

$$V_{n_i} = \sum_{j=1}^N \sigma_j N_{ij} + \gamma N_{i,N+1} + \vec{U} \cdot \hat{n}_i \quad (60)$$

$$V_{s_i} = \sum_{j=1}^N \sigma_j T_{ij} + \gamma T_{i,N+1} + \vec{U} \cdot \hat{t}_i, \quad (61)$$

Then, as described by the boundary conditions, the total velocity normal to the surface at each collocation point i must be equal to zero.

Therefore,

$$\sum_{j=1}^N \sigma_j N_{ij} + \gamma N_{i,N+1} = -\vec{U} \cdot \hat{n}_i \quad (62)$$

The following step is to implement the Kutta condition described earlier. Taking into consideration the direction of the unit tangent vectors \hat{t}_t and $\widehat{t_{t+1}}$, Figure 40, the magnitudes of the tangential velocities at the trailing edge panels can be equated to satisfy the Kutta condition.

This can be expressed as follows,

$$\sum_{j=1}^N \sigma_j T_{t,j} + \gamma T_{t,N+1} + \vec{U} \cdot \hat{t}_t = - \left(\sum_{j=1}^N \sigma_j T_{t+1,j} + \gamma T_{t+1,N+1} + \vec{U} \cdot \hat{t}_{t+1} \right) \quad (63)$$

Equation (63) can be further expressed as,

$$\sum_{j=1}^N \sigma_j (T_{t,j} + T_{t+1,j}) + \gamma (T_{t,N+1} + T_{t+1,N+1}) = -\vec{U} \cdot (\hat{t}_t + \hat{t}_{t+1}) \quad (64)$$

Equation (62) and Equation (64) form a system of linear algebraic equations of the form

$$\mathbf{M}a = \mathbf{b} \quad (65)$$

By solving for a , the strength of the sources and vortices can be found. Then, after calculating T_{ij} with the known strengths, the tangential velocity V_{S_i} can be obtained with Equation (61). The pressure coefficient can be then obtained using,

$$C_{p_i} = 1 - \left(\frac{V_{S_i}}{U} \right)^2 \quad (66)$$

The lift coefficient is given by Equation (8),

$$C_L = \frac{L}{\frac{1}{2} \rho_\infty V_\infty^2 A} \quad (8)$$

where L is lift force, ρ_∞ is freestream density, V_∞ is freestream velocity, and A is planform area.

The lift force per unit span is obtained by the Kutta-Joukowski theorem,

$$L' = \rho_\infty V_\infty \Gamma \quad (67)$$

where Γ is total circulation. The total circulation due to all the panels is given by $\Gamma = \sum_{j=1}^N \gamma s_j$.

Therefore,

$$L' = \rho_\infty V_\infty \sum_{j=1}^N \gamma s_j \quad (68)$$

where γ is the vortex strength and s_j is the length of the panel. As a final step, the lift coefficient per unit span is multiplied by the span length in order to obtain the lift force (Houghton *et al.*, 2013).

Implementation of Source – Vortex Panel Method Using MATLAB

The procedure for this approach is presented as a list of steps necessary to implement this computational method in MATLAB. Aside from initializing the necessary parameters, chord length c , span s , freestream velocity V_∞ , angle of attack α , etc., the procedure is as follows,

Discretization of Geometry and Grid Generation

For a NACA 4-digit airfoil, using the NACA 0010 symmetrical airfoil as an example, the first digit corresponds to the maximum camber as percentage of the chord ($m = 0\%$), the second digit corresponds to the distance of maximum camber from the airfoil leading edge by multiplying by 10 as percentage of the chord ($p = 0\%$), and the last two digits correspond to the maximum thickness of the airfoil as percentage of the chord.

First, in order to discretize the geometry, the appropriate spacing is chosen. For this study, cosine spacing is chosen as the best fit since it assigns smaller, and therefore a greater quantity, panels to the leading-edge and trailing-edge, which are the areas of high importance for an airfoil. By doing uniform spacing, the leading and trailing edge could not be taken appropriately, causing the program to miss information in these areas of interest.

$$\frac{x}{c} = \frac{1}{2}(1 - \cos(b)), (0 \leq b \leq \pi) \quad (69)$$

The establishment of the airfoil geometry is given by using the formulas to generate the shape of the NACA 4-digit airfoil (Anderson, 2011).

For the camber line of the airfoil,

$$y_c = \frac{m}{p^2}(2px - x^2), x < p \quad (70)$$

$$y_c = \frac{m}{(1 - p^2)}((1 - 2p) + 2px - x^2), x > p \quad (71)$$

The airfoil thickness is given by,

$$y_t = \frac{t}{0.2} (0.2969\sqrt{x} - 0.126x - 0.3516x^2 + 0.2843x^3 - 0.1015x^4) \quad (72)$$

If a closed trailing edge is desired, then Equation (72) becomes

$$y_t = \frac{t}{0.2} (0.2969\sqrt{x} - 0.126x - 0.3516x^2 + 0.2843x^3 - 0.1036x^4) \quad (73)$$

In order to obtain the coordinates for the upper and lower surface,

$$x_U = x - y_t \sin \theta \quad (74)$$

$$x_L = x + y_t \sin \theta \quad (75)$$

$$y_U = y_c + y_t \cos \theta \quad (76)$$

$$y_L = y_c - y_t \cos \theta \quad (77)$$

where

$$\theta = \arctan \left(\frac{dy_c}{dx} \right) \quad (78)$$

After obtaining the boundary points $[X, Y]$, it is necessary to obtain the collocation points $[XC, YC]$. At these points, the boundary conditions are later to be evaluated. During this step of the process, other parameters are calculated such as length of the panel S and normal and tangent unit vectors \hat{t} and \hat{n} .

Figure 43 shows the NACA 0010 airfoil generated using 26 panels ($N = 26$), as an example. However, this computational program allows for the number of panels to be modified, as observed in Figure 43. A comparison of the results depending on the number of panels is presented with the results. The collocation points are marked with a red dot, positioned at the center of each of the panels. The implementation of cosine spacing is also observed on this figures, whit a higher concentration of points at the leading edge and trailing edge.

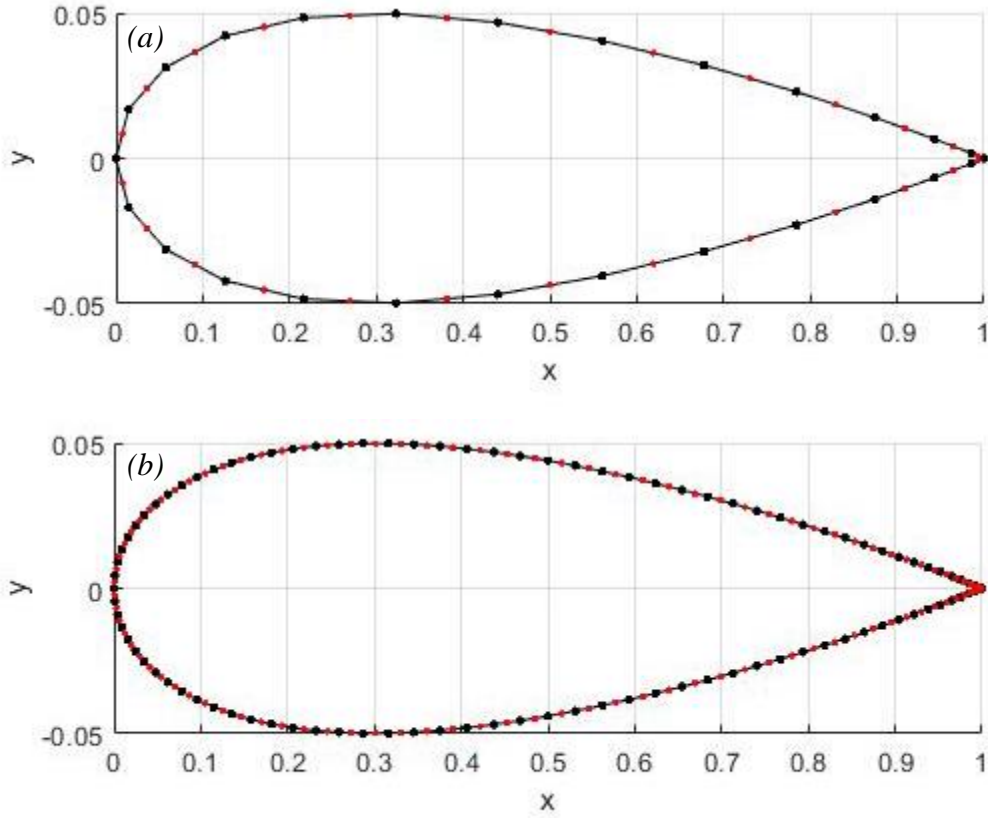


Figure 43. Discretization of NACA 0010 airfoil with (a) 26 and (b) 100 panels

Influence Coefficients in Matrix Form

Referring to the source – vortex panel method procedure section above, to calculate the influence coefficients for both the source and vortex, the following expressions are used,

$$N_{ij} = v_{x_Q} \hat{n}_i \cdot \hat{t}_j + v_{y_Q} \hat{n}_i \cdot \hat{n}_j, (i = 1, 2, \dots, N \text{ and } j = 1, 2, \dots, N) \quad (36)$$

$$T_{ij} = v_{x_Q} \hat{t}_i \cdot \hat{t}_j + v_{y_Q} \hat{t}_i \cdot \hat{n}_j, (i = 1, 2, \dots, N \text{ and } j = 1, 2, \dots, N) \quad (37)$$

$$N_{i,N+1} = \sum_{j=1}^N (v_{y_Q} \hat{n}_i \cdot \hat{t}_j - v_{x_Q} \hat{n}_i \cdot \hat{n}_j), (i = 1, 2, \dots, N) \quad (58)$$

$$T_{i,N+1} = \sum_{j=1}^N (v_{y_Q} \hat{t}_i \cdot \hat{t}_j - v_{x_Q} \hat{t}_i \cdot \hat{n}_j), (i = 1, 2, \dots, N) \quad (59)$$

$$N_{N+1,j} = T_{t,j} + T_{t+1,j}, (j = 1, 2, \dots, N + 1) \quad (79)$$

$$T_{N+1,j} = 0, (j = 1, 2, \dots, N + 1) \quad (80)$$

For ease of calculation, even though only the normal influence coefficient is utilized in the first half of calculations, the normal and tangent influence coefficients are carried out simultaneously in MATLAB for $i=1$ to N and $j=1$ to N . However, there's a case that must be addressed first, that is when $i = j$. For this case, the velocity is being induced on the panel by the singularities distributed on the same panel. At this point, $x_Q = y_Q = 0$.

Therefore, for the sources,

$$v_{x_Q} = 0 \text{ and } v_{y_Q} = \pi$$

Applying the rules of dot product, the influence coefficients are given the value of,

$$N_{ij} = v_{x_Q} \hat{n}_i \cdot \hat{t}_j + v_{y_Q} \hat{n}_i \cdot \hat{n}_j = \pi$$

$$T_{ij} = v_{x_Q} \hat{t}_i \cdot \hat{t}_j + v_{y_Q} \hat{t}_i \cdot \hat{n}_j = 0$$

For the vortices,

$$N'_{ij} = v_{y_Q} \hat{n}_i \cdot \hat{t}_j - v_{x_Q} \hat{n}_i \cdot \hat{n}_j = 0$$

$$T'_{ij} = v_{y_Q} \hat{t}_i \cdot \hat{t}_j - v_{x_Q} \hat{t}_i \cdot \hat{n}_j = \pi$$

As a result, the influence coefficients in matrix form are as follows,

$$\mathbf{M} = \begin{bmatrix} N_{i,j} & N_{i,j+1} & \dots & N_{i,N} & N_{i,N+1} \\ N_{i+1,j} & N_{i+1,j+1} & \dots & N_{i+1,N} & N_{i+1,N+1} \\ \cdot & \cdot & \cdot & \cdot & \cdot \\ \cdot & \cdot & \cdot & \cdot & \cdot \\ \cdot & \cdot & \cdot & \cdot & \cdot \\ N_{N,j} & N_{N,j+1} & \dots & N_{N,N} & N_{N,N+1} \\ N_{N+1,j} & N_{N+1,j+1} & \dots & N_{N+1,N} & N_{N+1,N+1} \end{bmatrix}$$

Establish Right-Hand-Side of Equations in Vector Form

The RHS of Equation (62) and Equation (64) contains the effects of the freestream,

$$\sum_{j=1}^N \sigma_j N_{ij} + \gamma N_{i,N+1} = -\vec{U} \cdot \hat{n}_i \quad (62)$$

$$\sum_{j=1}^N \sigma_j (T_{t,j} + T_{t+1,j}) + \gamma (T_{t,N+1} + T_{t+1,N+1}) = -\vec{U} \cdot (\hat{t}_t + \hat{t}_{t+1}) \quad (64)$$

In matrix form, it is expressed as follows,

$$\mathbf{b} = \begin{bmatrix} -\vec{U} \cdot \hat{n}_i \\ -\vec{U} \cdot \hat{n}_{i+1} \\ \vdots \\ -\vec{U} \cdot \hat{n}_N \\ -\vec{U} \cdot (\hat{t}_t + \hat{t}_{t+1}) \end{bmatrix}$$

Solve System of Linear Algebraic Equations of the Form $\mathbf{Ma} = \mathbf{b}$

Once the influence coefficient in matrix form \mathbf{M} and RHS in vector form \mathbf{b} have been constructed, using built in functions from MATLAB can solve the system of linear algebraic equations directly. The resultant vector results in the strength of the sources and vortices as follows,

$$\mathbf{a} = \begin{bmatrix} \sigma_i \\ \sigma_{i+1} \\ \cdot \\ \cdot \\ \cdot \\ \sigma_N \\ \gamma \end{bmatrix}$$

After obtaining the strength of the singularities, Equation (61) can be used to calculate the tangential velocity to the surface,

$$V_{S_i} = \sum_{j=1}^N \sigma_j T_{ij} + \gamma T_{i,N+1} + \vec{U} \cdot \hat{t}_i, \quad (61)$$

Calculations of Pressure and Loads

The pressure distribution the surface of the airfoil is simply obtained using Equation (66)

$$C_{p_i} = 1 - \left(\frac{V_{S_i}}{U} \right)^2 \quad (66)$$

The lift force per unit span is obtained using Equation (69),

$$L' = p_\infty V_\infty \sum_{j=1}^N \gamma S_j \quad (69)$$

Then, by multiplying the lift per unit span by the span length, the lift coefficient is calculated by Equation (8)

$$C_L = \frac{L}{\frac{1}{2} \rho_\infty V_\infty^2 A} \quad (8)$$

Sources and Vortex Strengths

Solving Equation (65) results in the sources and vortex strength given by vector a .

Recalling that the vortex strength does not vary from panel to panel, a single vortex strength value is found per case (per angle of attack) studied. Figure 44 shows the vortex strength varying with angle of attack. As it is observed, the vortex strength increases as the angle of attack is increased. The increase of the vortex strength has a direct effect on the tangential velocity, pressure coefficient, and hence lift coefficient, which will be calculated afterwards.

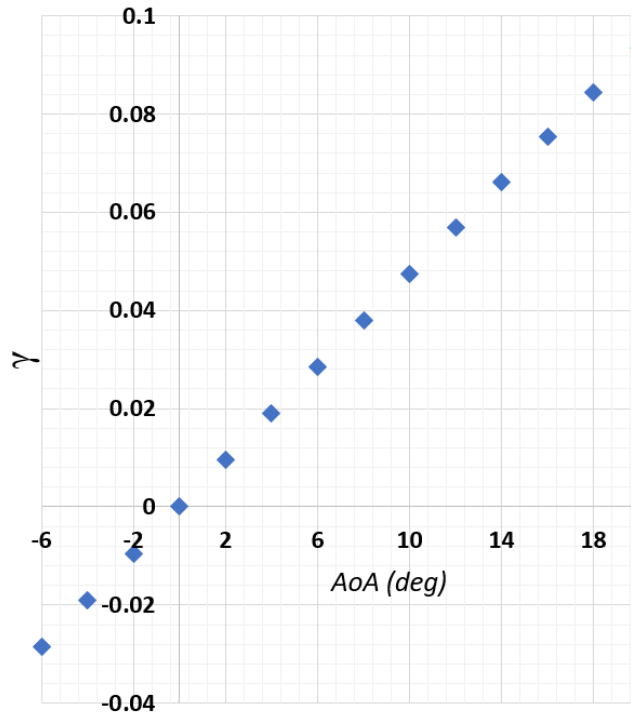


Figure 44. Vortex strength variation with angle of attack

The source strength does vary from panel to panel. Therefore, Figure 45 shows the source strength distribution around the airfoil for various angles of attack studied. Angles of attack 2, 4, 6, and 8 degrees are chosen in order to observe the source strength distribution. As it can be seen, the source strength difference on the upper and lower surface appears to increase as the angle of attack is increased. This in turn has a direct effect on the pressure coefficient.

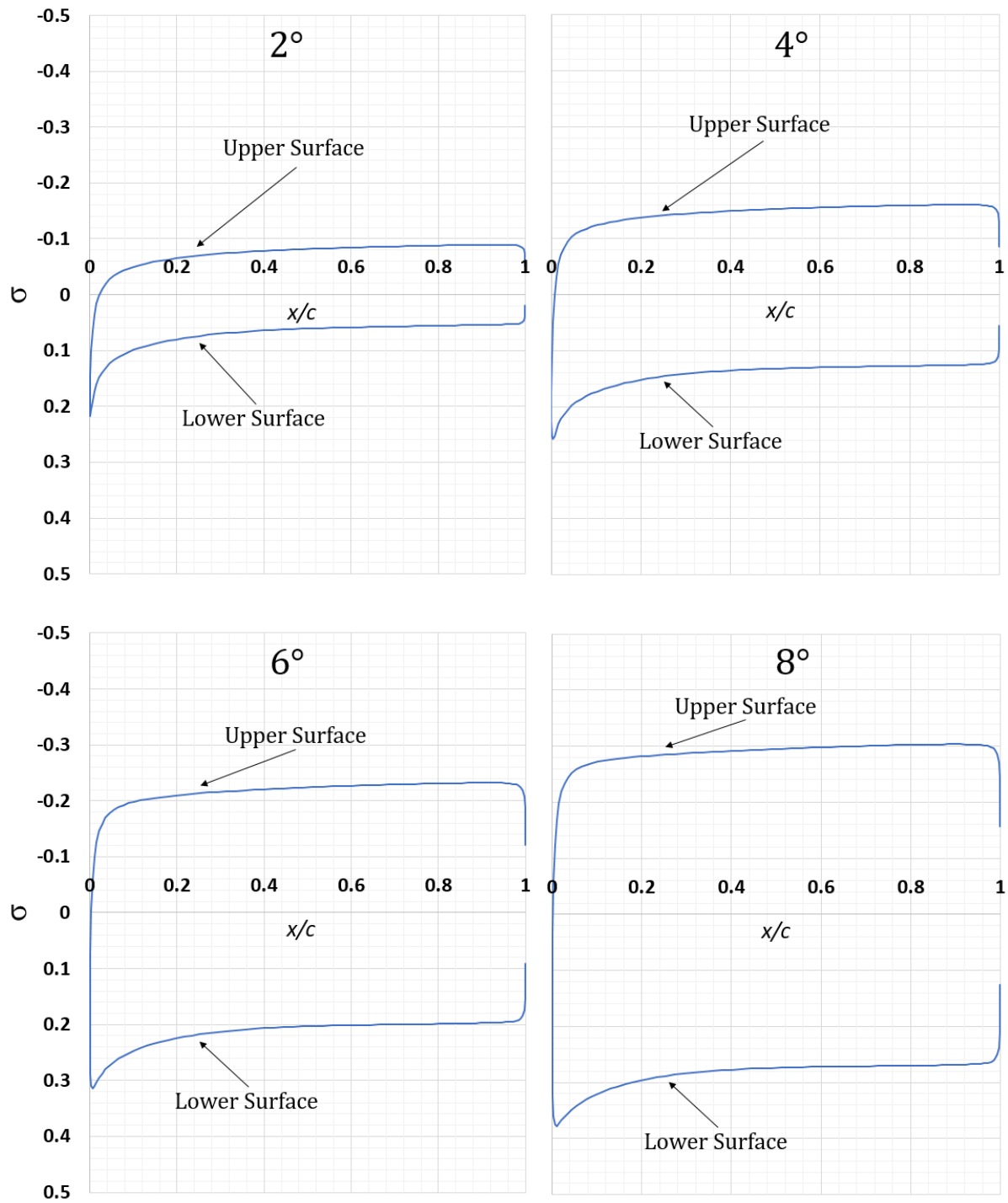


Figure 45. Source strength distribution for NACA 0010 airfoil at various angles of attack

Surface Pressure Distribution

For the surface pressure distribution, the pressure coefficient is obtained with Equation (64), as explained above. In order to validate the results, data from the literature can be compared to current results. Figure 46 shows the comparison of the pressure coefficient results using panel methods for NACA 0010 at an angle of attack of 0 degrees, showing a similar behavior to the data obtained by Mason (2015).

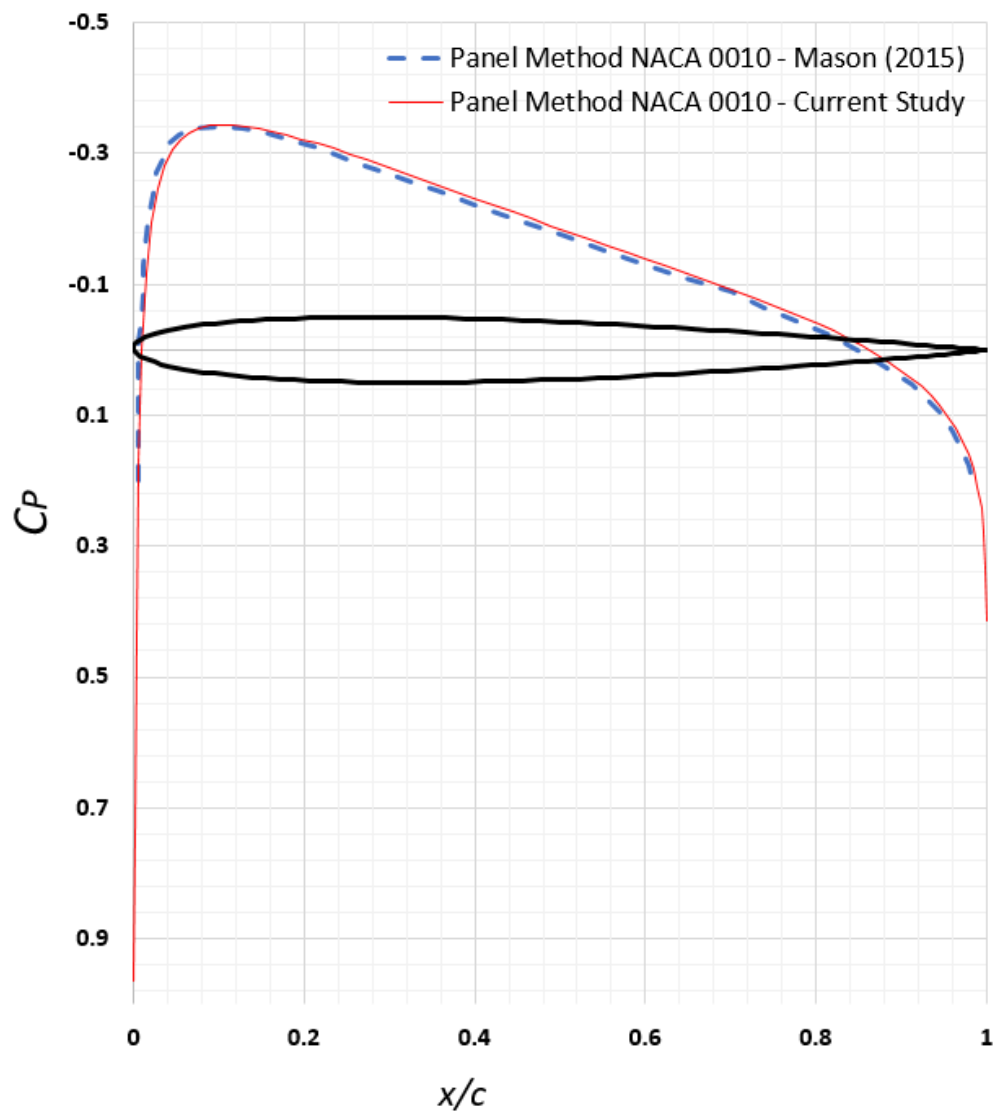


Figure 46. Pressure coefficient distribution on the upper and lower surface for a NACA 0010 airfoil at 0 degrees – Panel method

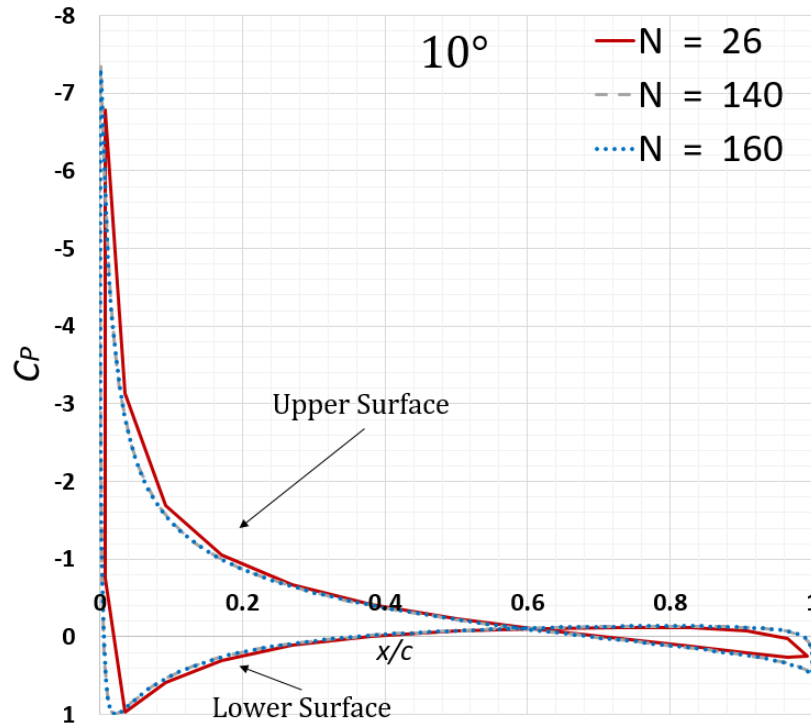


Figure 47. Effect of panel number on accuracy of results

In Figure 46, it can be seen that for an angle of attack of 0 degrees, the pressure coefficient is the same for the upper and lower surface, which agrees with the theory. The following lift coefficient results show how since there's no pressure gradient for this case, lift is zero for angle of attack of zero degrees.

According to the literature, the number of panels can determine the accuracy of the results obtained, the higher the number of panels in which the airfoil is discretized, the higher the accuracy in the results that can be obtained. In order to understand this, pressure coefficient distribution for an angle of attack of 10 degrees is obtained using various numbers of panels.

Figure 47 shows the results using 26, 140, and 160 panels. From the results obtained using 26 and 140, there's a noticeable difference. However, for higher number of panels, there is really no difference after 140 panels. Therefore, the number of panels chosen for this study is 140 panels.

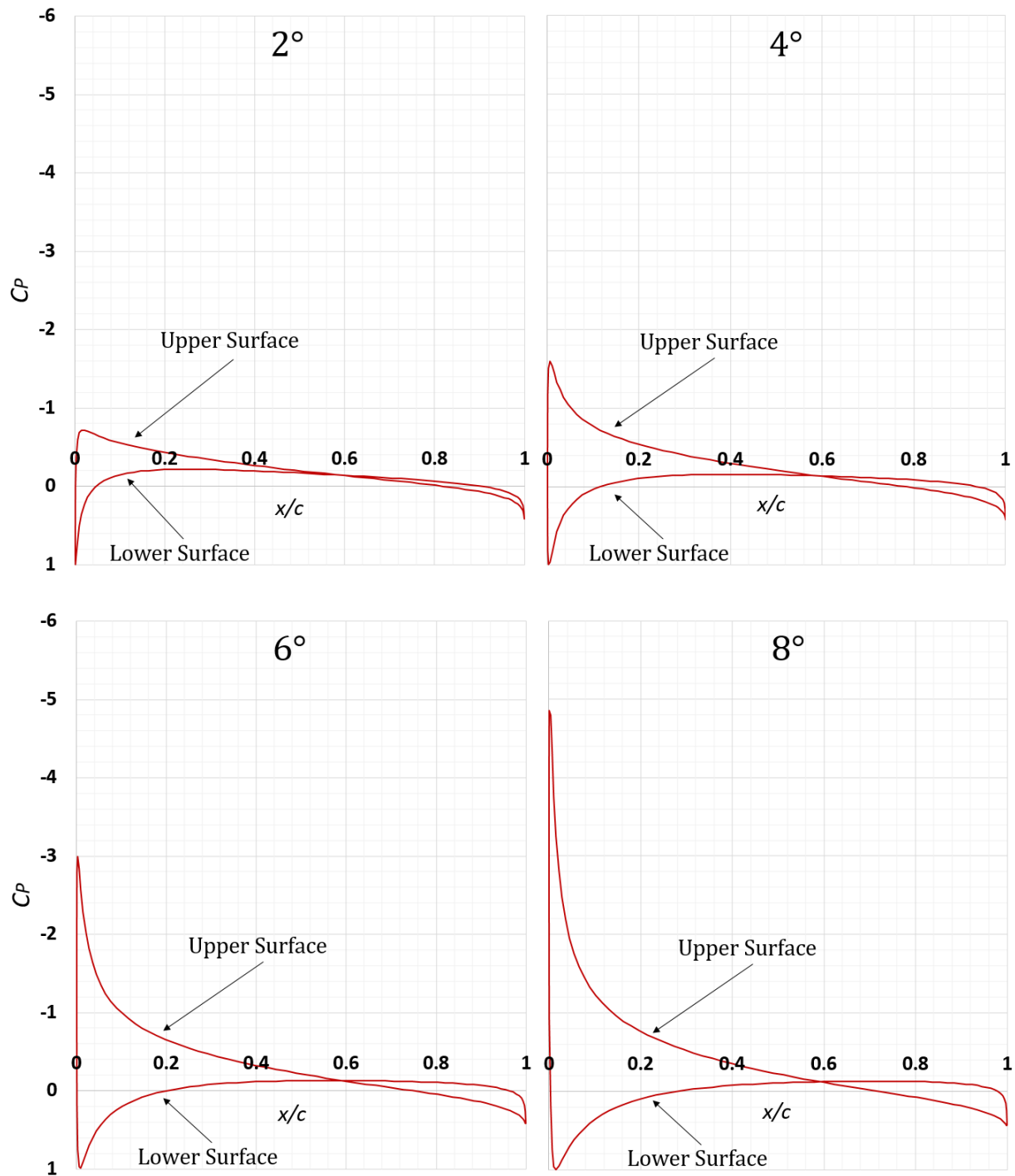


Figure 48. Pressure coefficient distribution for NACA 0010 airfoil at various angles of attack

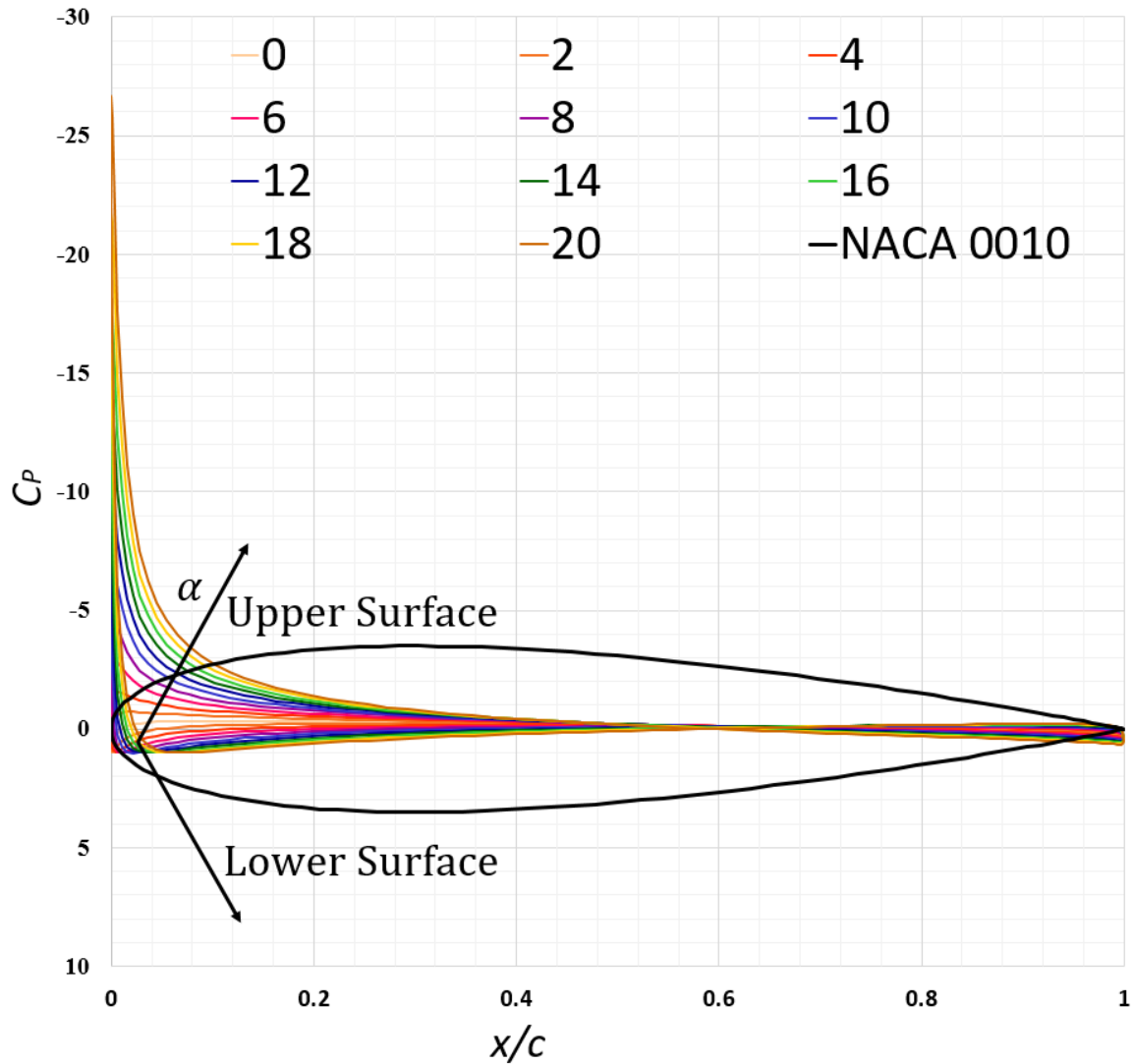


Figure 49. Pressure coefficient distribution for a NACA 0010 airfoil for all angles of attack

The pressure coefficient is calculated for the complete range of angles of attack chosen for this study. Figure 48 illustrates the pressure coefficient distribution for angles of attack varying from 2 to 8 degrees in increments of 2 degrees. As it is expected from the literature, as the angle of attack is increased, the pressure coefficient on the upper surface increases in the negative values, creating a greater pressure gradient. The increase in the pressure gradient results in a greater production of lift force, which is confirmed in the following section.

For more convenience, Figure 49 shows the pressure coefficients for all angles of attack. As it is depicted, the pressure gradient is increasing as the angle of attack is increased.

Lift Prediction

Continuing with the lift coefficient results, the lift coefficient is given by Equation (8).

Lift coefficient is calculated for the entire range of angles of attack chosen for this study. Figure 50 shows the results obtained with panel method, data from the literature and thin airfoil theory. As it is observed, the data obtained is very similar to that of Mason (2015) for NACA 0012. It is unclear which version of the panel method was utilized by Mason (2015).

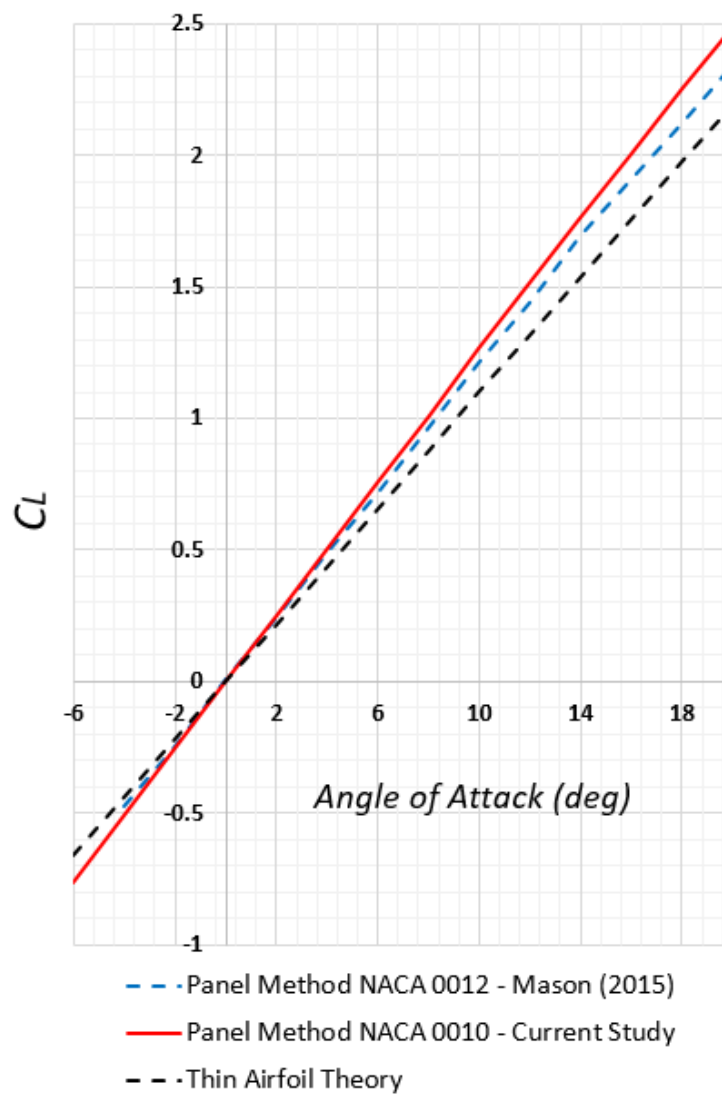


Figure 50. Variation of lift coefficient with angle of attack for a NACA 0010 airfoil – Panel method

However, when comparing thin airfoil theory with panel method, it can be observed that the lift coefficient results for the panel method have a higher lift curve slope. Thin airfoil theory results in a lift curve of 2π . This comes from the assumptions made for thin airfoil theory, which neglects the effect of the thickness of the airfoil by placing the vortex sheet on the mean camber line of the airfoil (in comparison with vortex distribution on the surface of the airfoil, as seen for panel methods) and only considering small angles of attack. For symmetrical airfoils, as is the case for this study, the results found from thin airfoil theory are such as if flow over a flat plate at small angles of attack, also assuming inviscid and incompressible flow.

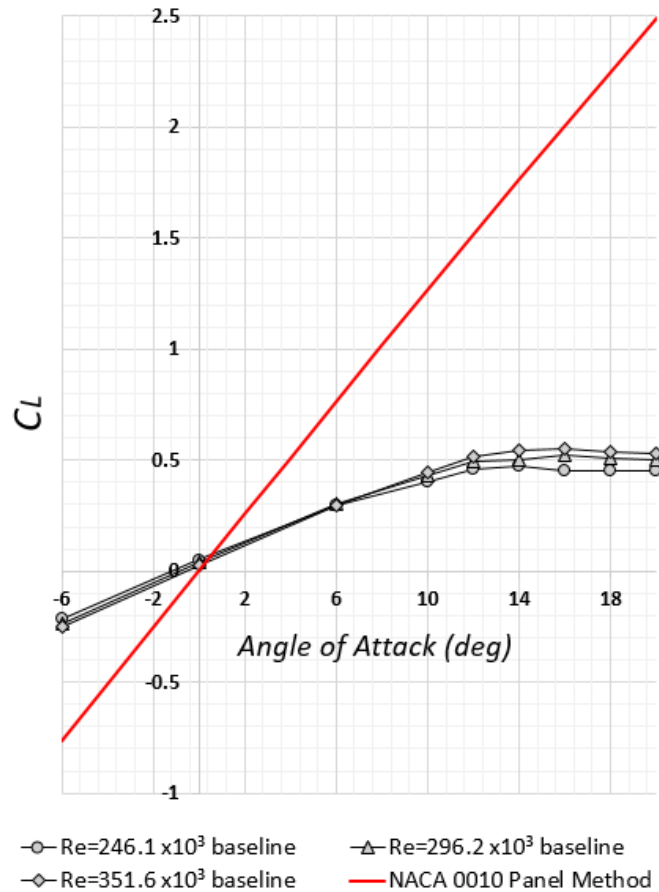


Figure 51. Comparison between calculated and experimental results for NACA 0010 airfoil

From Figure 50, the lift coefficient increases as the angle of attack is increased, which was noted for the pressure distribution before. Recalling that for the panel method inviscid flow is assumed, which would be the conditions outside of the boundary layer, the lift coefficient does not reach stall conditions since this is a consequence of the flow separation, which in turn arises from viscous effects. Therefore, a maximum lift coefficient is not observed for the results. Here, it is only possible to see the linear increase of the lift coefficient for small angles of attack. From this, it can also be justified why the increase in Reynolds number, as introduced in the current panel method developed, posed no change to the results obtained. Considering the statements made above, when comparing the results from the panel method to those of experimental data, only the lift coefficient results for small angles of attack are expected to be predicted by the panel method's results.

Figure 51 shows the comparison between the experimental results obtained for various Reynolds numbers for this study and those obtained for the panel method. As it can be observed, the difference between results is significant, even for small angles of attack. Due to the inviscid assumptions on the panel method, results were expected to be slightly higher for the panel method. Panel methods only show 2D effects for airfoils; however, the experimental data obtained for finite wings take into account 3D effects, which result in a downwash force. The introduction of this force, affects the angle of attack being experienced by the wing, which is called effective angle of attack. Due to the reduction of this angle, the lift coefficient results are smaller for experimental data obtained for finite wings.

Conclusion

In conclusion, panel methods are a strong and helpful tool in the primary steps of the design of airfoils. The results are highly comparable when put side to side with thin airfoil theory. With a proper execution, a wide variety of airfoils can be evaluated at different angles of

attack. For the current study, even though the results obtained seem to be coincident with the literature and theory, there are still improvements that should be performed. For the pressure coefficient results there's an evident miss calculation around 0.6 of the normalized axial length of the airfoil. These results could be due to a condition not being implemented properly or a parameter calculated wrongly. For the lift coefficient, further analysis should be performed on the comparison between experimental data and results obtained from panel method by taking into account 3D effects. This can be performed by utilizing vortex lattice method.

CHAPTER IV

RESULTS AND DISCUSSION

Introduction

In this chapter, results obtained for the various parameters studied are presented, lift measurements, drag measurements, and flow field characteristics. First, the model with 8 tubercles along the span (8T) is studied in comparison with the baseline. In order to understand the effects of tubercles on the aerodynamic performance, the aerodynamics characteristics are studied. Next, the effects of varying the wavelength of the tubercles is studied by comparing the resultant aerodynamic characteristic of the models with various tubercle configurations (4T, 8T, 10T, and 12T) and the baseline. Afterwards, by selecting 8T, the effect of the Reynolds number on the performance of the models is studied by varying the Reynolds number within a selected range and recording the effect on the aerodynamic characteristics. To finalize this chapter, by selecting 8T, the effects of leading-edge tubercles on the flow field characteristics are presented by studying the velocity and vorticity fields and taking turbulence measurements.

Lift Measurements

The forces obtained from the transducers are used to calculate the lift force. Equation (9) relates the x and y-components from both transducers to the lift force,

$$F_L = (A_y + B_y) \cos \theta + (B_x - A_x) \sin \theta \quad (9)$$

Then, Equation (1), corresponding to the calibration of the transducers, is applied to results obtained by Equation (9),

$$L = 0.9972F_L - 0.2745 \quad (1)$$

Once lift forces are calculated, the lift coefficient can be obtained using Equation (8),

$$C_L = \frac{L}{\frac{1}{2}\rho V^2 A} \quad (8)$$

Figure 52 shows the lift coefficient C_L results with varying angle of attack at a Reynolds number of 201,200 marked with a gray circle and black star for the baseline and 8T, respectively. For small angles of attack, the expected behavior of the lift coefficient is met for both models. In this region, the lift coefficient increases linearly with increasing angle of attack.

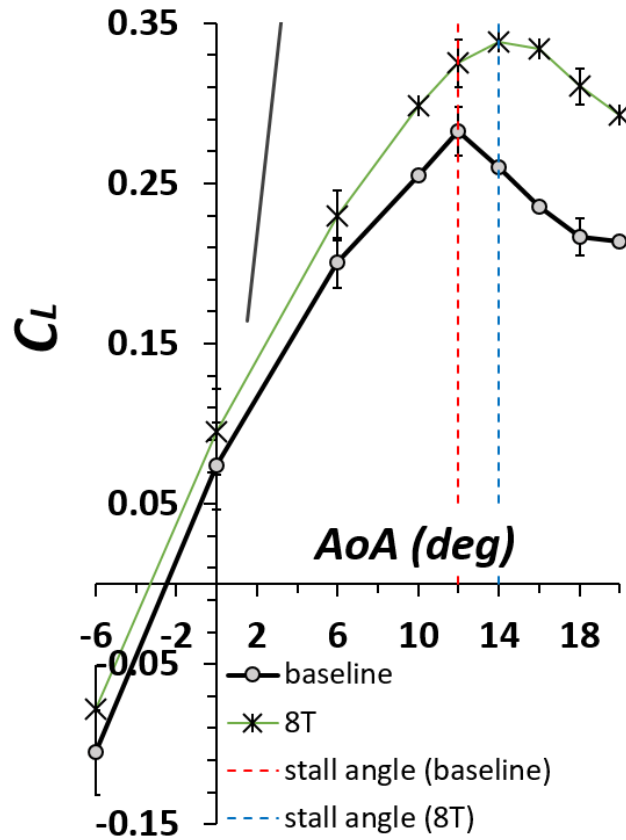


Figure 52. Variation of lift coefficient with angle of attack for 8T and baseline at a Reynolds number of 201,200

Then, stall conditions due to the viscous effects and boundary layer separation result in a maximum lift coefficient $C_{L,max}$. The stall angle is the angle of attack at which this maximum lift coefficient is reached. After that, in the poststall regime, a decrease in the lift coefficient is observed for both models. Depending on the causes of stall (leading-edge or trailing-edge stall), there will be a difference on the rate and behavior at which the lift coefficient is decreasing.

From these results, even though there's a slight shift on the 8T data, it is possible to observe that in the prestall regime, the behavior of the lift coefficient is very similar between the two models. Then in the stall regime, when comparing the baseline and 8T, the baseline stalls at 12 degrees, and 8T stalls at 14, showing an increase in the stall angle. In the poststall regime, it can be pointed out that there is a significant increase in the maximum lift coefficient for 8T in comparison with the baseline of 20%. As mentioned in the literature review, this increase in the delay in stall and maximum lift coefficient, which is also observed in this study, is directly attributed to the generation of streamwise vortices on the surface due to the addition of tubercles on the leading-edge of the model. This statement is also confirmed later in the flow field measurements using PIV. The enhancement of the aerodynamic characteristics for the leading-edge tubercles is confirmed by the increase in two parameters, $C_{L,max}$ and α_{stall} , very similar results than those experienced by lower turbulence intensities.

The next step is to study the variation in the wavelength of the tubercles to understand how this affects the model's performance. The lift coefficient for one model with higher wavelength (4T) and two models with smaller wavelength (10T and 12T) than 8T are obtained and shown in Figure 53.

Figure 53 shows the lift coefficient with varying angles of attack at a Reynolds number of 201,200 for all models marked with a gray circle, an orange square, a black star, a red circle, and

a blue diamond for the baseline, 4T, 8T, 10T, and 12T, respectively. These identification markers and colors are respected throughout this section. Starting in the prestall regime, the lift curve slope serves as an indication of the rate of change of the lift coefficient with angle of attack, meaning how rapidly the lift coefficient increases as the angle of attack is increased. A higher slope would mean a more rapid increase. As it was mentioned in the previous chapter, the theoretical lift curve slope is 2π . For the experimental results, the lift curve slope decreases for finite wings due to the downwash forces and hence the reduction of the effective angle of attack experienced by the wing. A significant smaller slope is observed for this study of about 0.020.

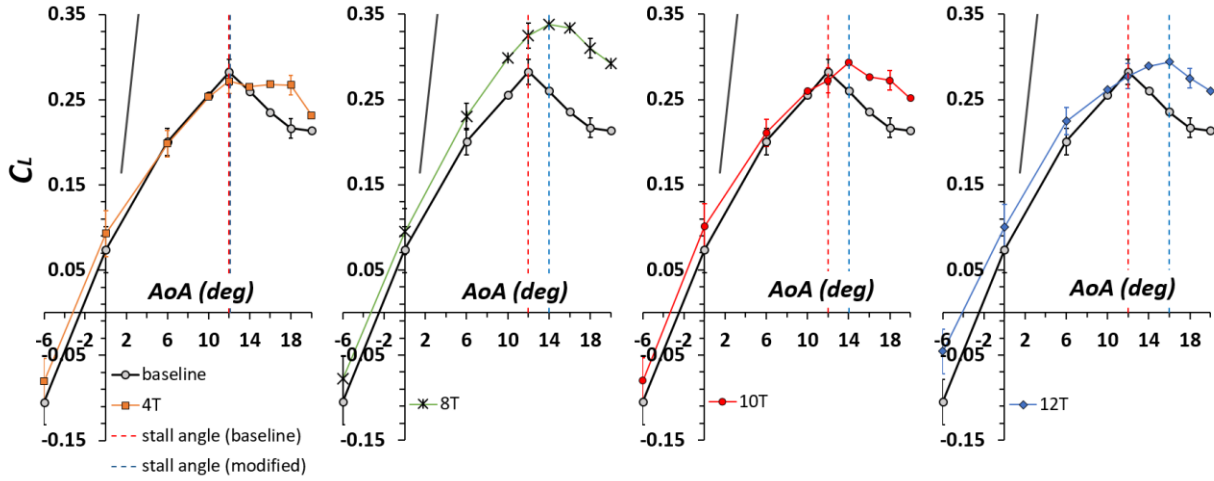


Figure 53. Variation of lift coefficient with angle of attack for all models in comparison with the baseline at a Reynolds number of 201,200

With further increase in angle of attack, the wing starts to reach the stall region. The stall behavior can be studied by observing the results for the stall angle of attack and the maximum lift coefficient. As shown in the first column of Table 3, the stall angle for 4T remains the same as that of the baseline. For 8T and 10T, the stall angle increases from 12 to 14 degrees. For 12T, the stall angle increases from 12 to 16. The latter model shows a greater increase in the stall angle than that from the baseline by approximately 30%.

Table 3. Stall angle and maximum lift coefficient due to variation in number of tubercles along the spanwise direction for a Reynolds number of 201,200

	stall angle (deg)	$C_{L,max}$
baseline	12	0.283
4T	12	0.272
8T	14	0.338
10T	14	0.293
12T	16	0.294

In the poststall regime, the lift coefficient for 4T, 8T, 10T, 12T increases up to 23, 43, 26, and 27%, respectively. However, as shown in the second column of Table 3, only 8T, 10T, and 12T present a higher $C_{L,max}$ than the baseline; the maximum lift coefficient increases 20, 4, 4%, respectively. Model 8T results in a higher $C_{L,max}$ when compared to smaller wavelengths (10T and 12T). For 4T, the maximum lift coefficient decreases slightly than the baseline approximately 4%.

Continuing in the poststall regime, a more gradual loss in lift is observed in all models, especially 8T, 10T and 12T, as seen in Figure 53. This can be confirmed by calculating the L/D ratio, which will be presented in following sections. By measuring the aerodynamic performance in terms of lift coefficient in its entirety, 8T and 12T appear to have the greater performance enhancement in comparison with the baseline due to the significant increase in C_L and α_{stall} , respectively. The greater wavelength, 4T, is the tubercle configuration that have results similar than those of the baseline.

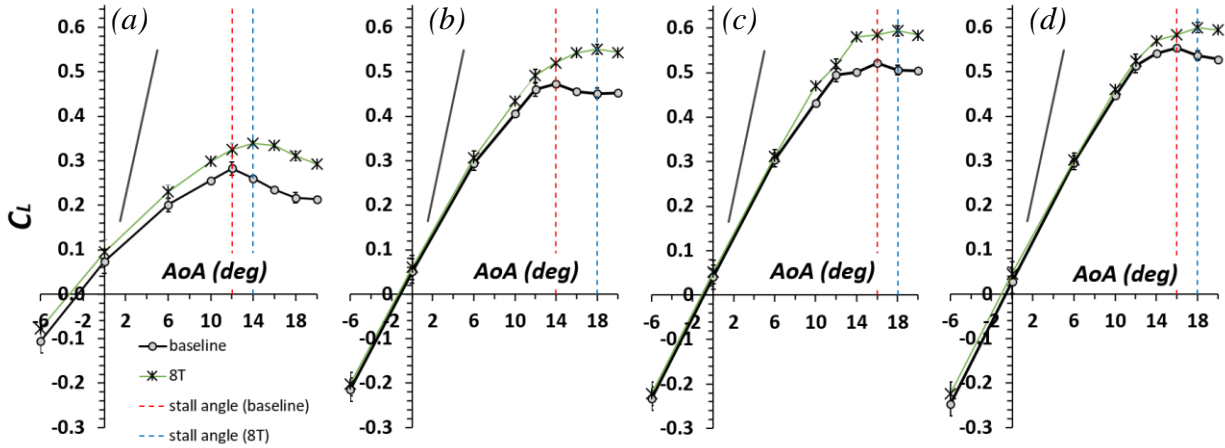


Figure 54. Comparison in the variation of lift coefficient with angle of attack between 8T and the baseline for Reynolds number of (a) 201,200, (b) 246,100, (c) 296,200, and (d) 315,600

Continuing with the needed analysis to understand the effect of Reynolds number on lift coefficient, the lift coefficient for 8T and the baseline at Reynolds number ranging from 201,200 to 351,600 is presented in Figure 54 with varying angle of attack. Starting in the prestall regime, Figure 55(a) shows the lift curve slope for 8T and the baseline for the Reynolds number studied. As it was mentioned, the slope is an indication of the rate of change of lift with angle of attack. For Reynolds numbers 201,200, 246,100, and 296,200, the slope increases for 8T about 12, 6, and 6% in comparison with the baseline. However, for the highest Reynolds number studied, the slope decreases for 8T by about 1%. An increase in lift curve slope has also been noted for lower turbulence intensities by Kim *et al.* (2018).

Continuing with the stall behavior, Figure 55(b) shows the stall angle for all Reynolds number tested. The stall angle for all Reynolds number, except for the lowest Reynolds number of 201,200, is 18 degrees. Even though the stall angle increases for all cases, the greater increase in stall angle is observed for a Reynolds number of 246,100 of about 29%, increasing from 14 to 18 degrees. The highest Reynolds numbers tested, 296,200 and 351,600 have the smallest increase of about 13%. It can be noted that the stall angle for the three highest Reynolds number

remains the same. For lower turbulence intensities, it has been noted by Guerreiro *et al.* (2012) that Reynolds number does not seem to affect the behavior of the modified models when comparing them to other modified models at higher or lower Reynolds number; however, when comparing with the baseline for the same Reynolds number, the addition of leading-edge tubercles does seem to enhance the performance. This behavior is also observed in these results

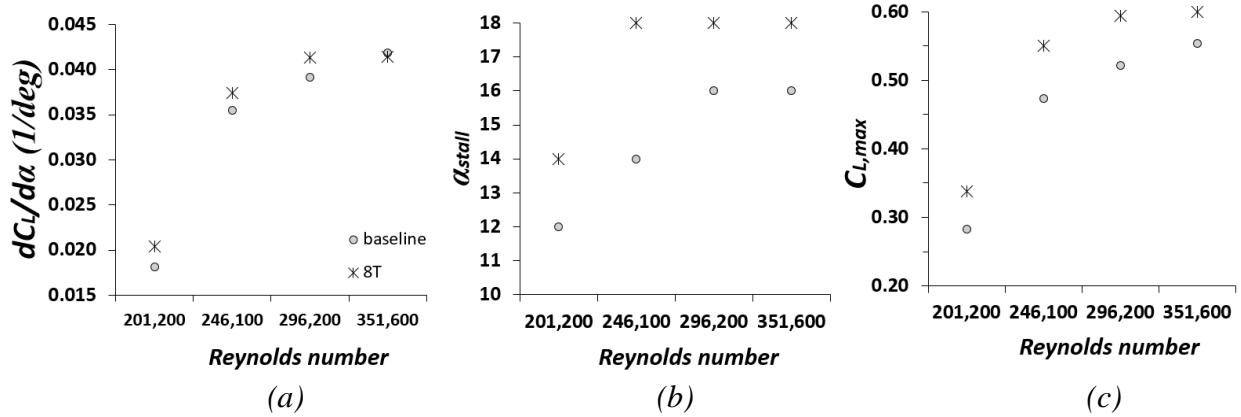


Figure 55. Comparison in the variation of (a) lift coefficient slope, (b) stall angle, and (c) maximum lift coefficient between 8T and the baseline for all Reynolds numbers tested

In the poststall regime, the lift coefficient increases for all models. For Reynolds number of 201,200, 246,100, 296,200, and 351,600, the lift coefficient increases approximately 43, 22, 18, and 13%, respectively. The greater increase in lift coefficient is found to be for Reynolds number of 201,200. Similarly as in the lowest Reynolds number presented previously, for all higher Reynolds number, the maximum lift coefficient increases as well. Figure 55(c) shows the maximum lift coefficient for all Reynolds numbers tested. For Reynolds numbers of 201,200, 246,100, 296,200, and 351,600, $C_{L,max}$ increases about 20, 17, 14, and 9%, respectively. In this parameter, the maximum increase in $C_{L,max}$ is given for the lowest Reynolds number tested. By looking at the results obtained, at higher turbulence intensities, the Reynolds number has a similar effect on lift measurements than those obtained at lower turbulence intensities. Reynolds

number. At the Reynolds number tested, there is evident performance enhancement, increasing or decreasing the Reynolds number does not provide a specific benefit to the implementation of tubercles. However, it can be noted that for the highest Reynolds number tested, the aerodynamic performance of the leading-edge tubercles deteriorates in comparison with the baseline. In the literature, mostly low to moderate Reynolds number are tested due to its similarity to the humpback whale's calculated Reynolds number. It was even noted by Custodio *et al.* (2015) at a lower turbulence intensity that for Reynolds number higher than 360,000, there was little change in lift coefficient, independent from Reynolds number.

Rake Measurements and Total Drag Calculations

As it was explained before, the pressure measurements obtained with the pitot rake are related to velocity by using Bernoulli's equation,

$$V = \sqrt{\frac{2\Delta P}{\rho}} \quad (81)$$

Resulting from this, the wake velocity profile is then integrated to obtain total drag per unit span, which is given by Equation (24),

$$D' = \rho \int_H^B V_2 (V_1 - V_2) dy \quad (24)$$

Equation (24) represents the momentum's deficit in the flow behind the body due to the interaction of the boundary layer with the surface of the model. After multiplying the total drag per unit span by the span length, total drag coefficient can then be obtained using Equation (10).

$$C_D = \frac{D}{\frac{1}{2} \rho V^2 c} \quad (10)$$

Figure 56 shows the wake velocity profiles for the range of angles of attack studied, -6 to 20 degrees, at a Reynolds number of 201,200 marked with a gray circle and a black star for the baseline and 8T, respectively. As it can be observed, as the angle of attack is increased, the size of the wake increases as well. This apparent increase in wake size reflects an increase in the momentum deficit. In the prestall regime, the wake size remains small. At this point, the pressure gradient is not sufficient enough to cause the flow to detach from the surface of the wing. However, in the poststall regime, the adverse pressure gradient results in a velocity inflection; therefore, the flow is prone to separation and recirculation. Consequently, the size of the wake increases significantly for both wings. The appearance of recirculation can be observed in the flow field characteristics shown in following sections. As it can be observed for 8T, for angles of attack up to 6 degrees, the wake remains almost the same size for both wings. However, looking at angles of attack greater than 6, the wake size behind 8T increases in comparison with that of the baseline, in some cases slightly.

After obtaining the total drag force, as explained previously, the drag coefficient is calculated. Figure 57 shows the corresponding drag coefficient results with varying angle of attack for 8T and the baseline at a Reynolds number of 201,200. For the small angles of attack, the drag coefficient behavior for both wings seems to be dominated by the viscous drag, where the flow still remains attached to the surface of the model. As it was explained, the pressure gradient is not yet significant. Up until an angle of attack of 10 degrees, the increase of drag coefficient is rather abrupt. At this point, the drag coefficient is dominated by the pressure drag, which, as its name implies, refers to a greater pressure gradient. Due to the increase in the pressure gradient, the flow is now prone to separation and recirculation.

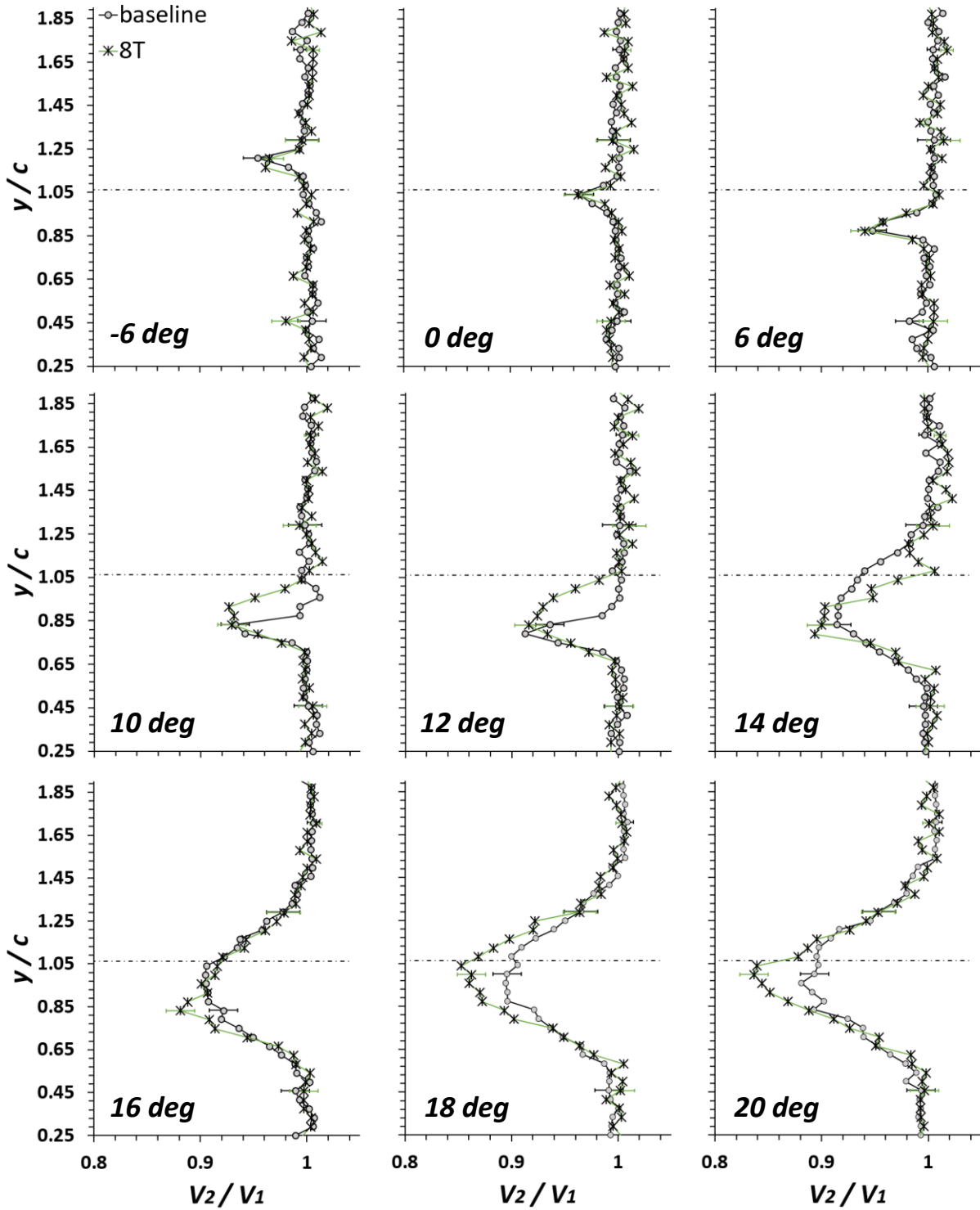


Figure 56. Baseline and 8T comparison of normalized wake velocity profiles for all angles of attack at a Reynolds number of 201,200

In the prestall regime, it can be seen that for lower angles of attack, the drag coefficient for 8T is similar to that of the baseline. The minimum drag coefficient $C_{D,min}$ for the baseline and 8T is shown to be 0.018 and 0.019, respectively, which is a marginal difference. However, for greater angles of attack, the drag coefficient C_D increases for 8T about 87% at 12 degrees. From the literature, it has been mentioned that the addition of tubercles on the leading-edge decreases drag coefficient at lower turbulence intensities. The results for this specific case are not in agreement with such statements, which can be related to the increase of on turbulence intensity. It can also be noted, that overall a more rapid increase in drag is observed for 8T; this was also observed by Custodio *et al.* (2015) at lower turbulence intensity.

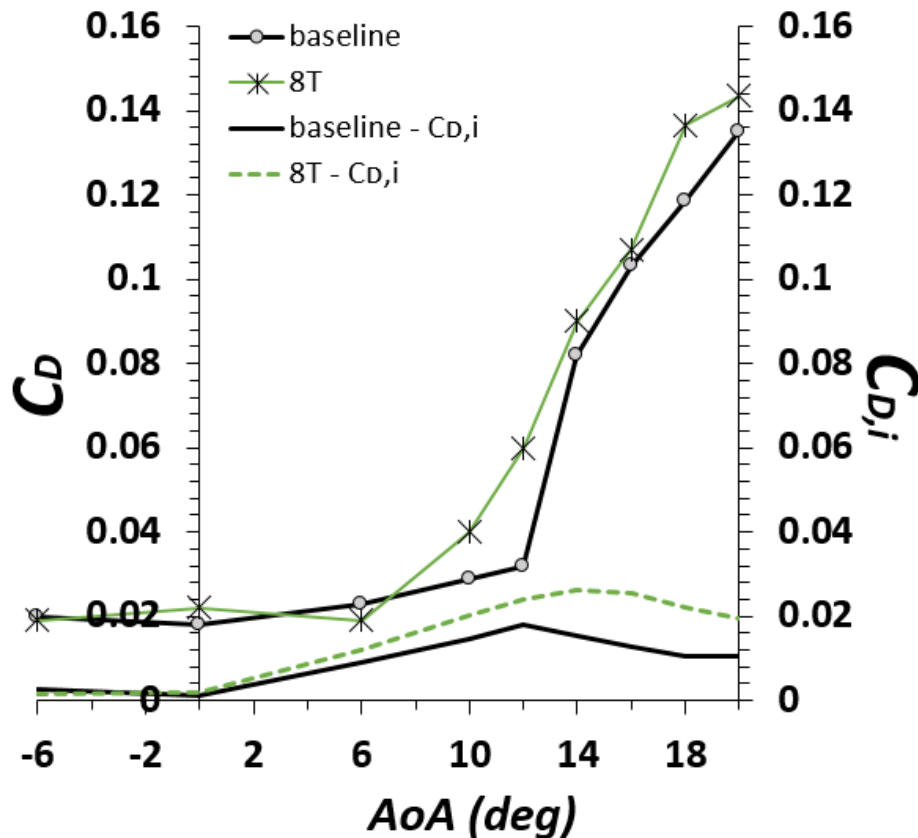


Figure 57. Variation of drag coefficient with angle of attack for 8T and baseline at a Reynolds number of 201,200

Using Prandtl's classical lifting-line theory for a finite wing, Figure 57 also shows the calculated induced drag coefficient, $C_{D,i}$, with black and green dashed-lines for the baseline and 8T, respectively given by

$$C_{D,i} = \frac{C_L^2}{\pi e AR} \quad (82)$$

where e is span efficiency factor and AR is aspect ratio. From the equation, the induced drag coefficient is proportional to the lift coefficient squared. Therefore, as it can be observed for positive angles of attack, the induced drag coefficient increases with increasing angle of attack in a significant and rapid manner, up to a point in which it starts decreasing.

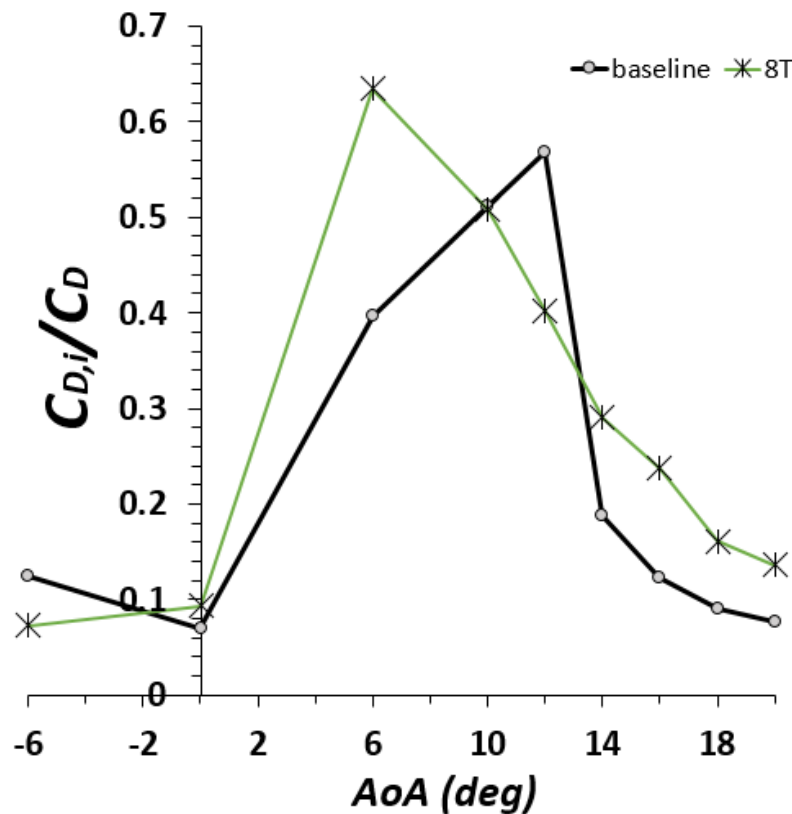


Figure 58. Variation of induced to total drag coefficient ratio with angle of attack for 8T and baseline at a Reynolds number of 201,200

By calculating the $C_{D,i}/C_D$ ratio, the percentage significance of the induced drag in terms of the total drag can be illustrated. Figure 58 shows the ratio's variation with angle of attack for the baseline and 8T at a Reynolds number of 201,200. As it can be seen, for angles of attack greater than 0 degrees, the percentage of induced drag quickly increases for both models. After reaching a certain point in which the ratio decreases almost linearly for the remaining angles of attack. The induced drag coefficient has a greater influence in the angles of attack corresponding to angles in the prestall and stall regime, where lift coefficient is still increasing and only viscous effects are contributing to total drag. However, once the flow starts to separate, and the total drag is influenced greatly by the separation of the boundary layer, lift and hence induced drag start to decrease. At this point, induced drag is contributing less to the total drag. Comparing 8T to the baseline, Figure 58 shows that the $C_{D,i}/C_D$ reaches a maximum for the baseline and 8T of 0.568 and 0.635, respectively.

According to Bertin *et al.* (2014), induced drag coefficient is the second greatest contribution to total drag. Therefore, the possible reduction in induced drag is an important consequence of the modified models reported by the literature for lower turbulence intensities. When comparing both models, it can be seen that for lower angles of attack, the induced drag increases for the modified model. For higher angles of attack, the induced drag $C_{D,i}$ increases with the addition of leading-edge tubercles. Both of these behaviors are an important difference noted between lower and higher turbulence intensities.

Another important parameter to be considered is the lift-to-drag ratio L/D . By calculating this ratio, it is possible to determine the efficiency of the wing. A greater L/D constitutes to a better performance due to greater lift or low drag force. Figure 59 shows the lift-to-drag ratio for the baseline and 8T at a Reynolds number of 201,200. The maximum L/D ratio decreased for 8T

about 15% in comparison with the baseline. However, the angle at which this maximum occurs decreased for the 8T from 12 to 10 degrees. From Figure 59, the more gradual decrease in lift coefficient noted previously can also be observed and confirmed for 8T for angles of attack greater than 12, which is in the poststall regime. The baseline has a more abrupt L/D for angles greater than 10 degrees. In the poststall regime, the lift-to-drag ratio increases marginally for 8T when compared to the baseline. The behavior observed for this modified model in the poststall is very similar than the behavior observed for lower turbulence intensities.

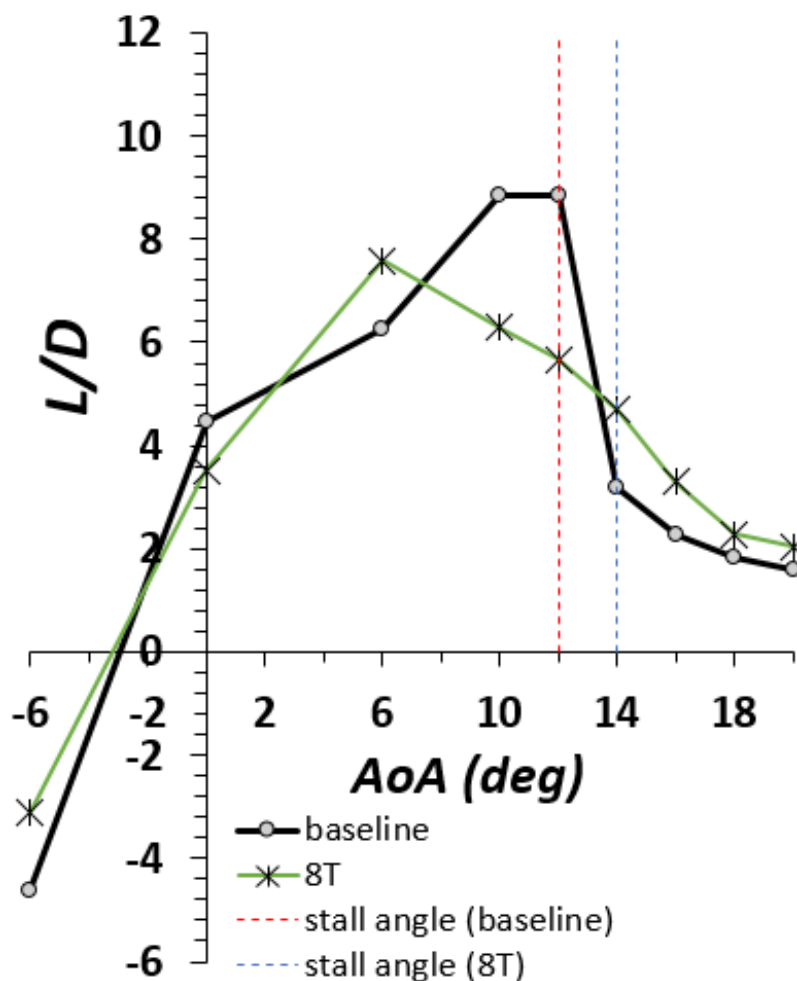


Figure 59. Variation of lift to drag ratio with angle of attack for 8T and baseline at a Reynolds number of 201,200

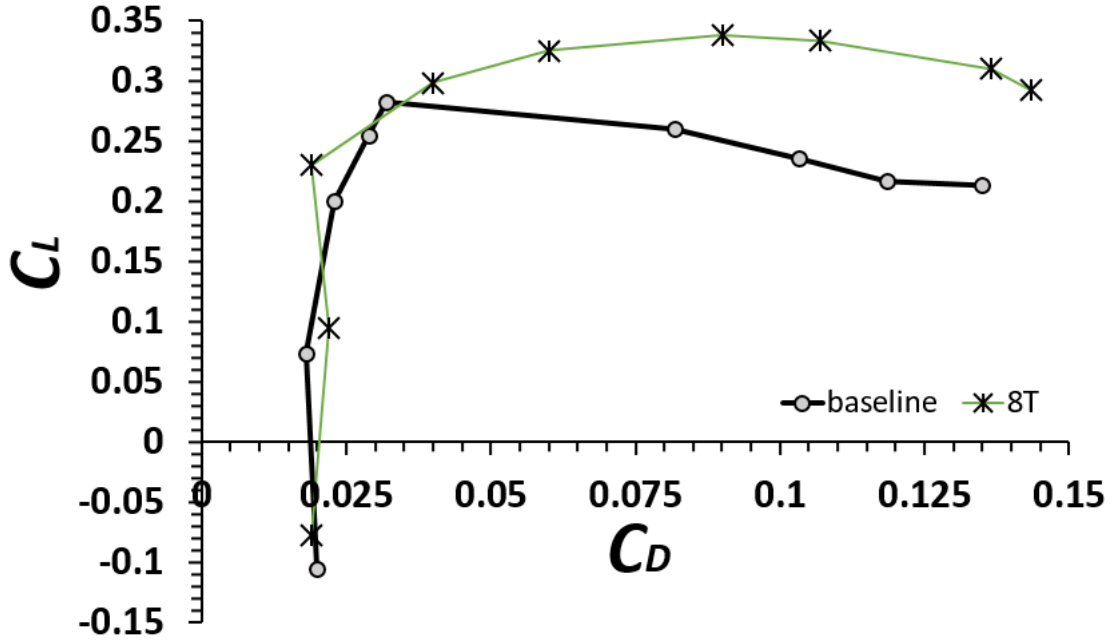


Figure 60. Drag polar for 8T and baseline at a Reynolds number of 201,200.

Another important parameter that can be analyzed to understand the effect of leading-edge tubercles is the drag polar. Figure 60 shows the drag polar for 8T and the baseline at a Reynolds number of 201,200. From the drag polar, the zero-lift drag coefficient can be observed, which is an important parameter during the design stage. For these two models, this value is very similar. Also, from the drag polar, it can be observed for the baseline, that the drag coefficient decreases before increasing with increasing angle of attack. However, for the modified model, this behavior is not observed. The behavior of the baseline is reported for lower turbulence intensities. Whether the resultant behavior observed by 8T is due to an increase in the turbulence intensity should be investigated further.

Next, the effect of tubercle geometry is studied by varying the wavelength of the tubercles while the amplitude is kept constant. The wake velocity profiles are obtained for all models in order to obtain the corresponding drag coefficient results. For these cases, the wake

velocity profiles are calculated at 10 and 18 degrees, angles of attack found in the prestall and poststall regime, respectively, for all models.

Figure 61 shows the wake velocity profiles at an angle of attack of 10 degrees at a Reynolds number of 201,200 for all models marked with a gray circle, an orange square, a star, a red circle, and a blue diamond for the baseline, 4T, 8T, 10T, and 12T, respectively. For this angle of attack, which is still in the prestall regime for all models, starting with the highest wavelength, the wake size is slightly smaller for 4T in comparison with the baseline. However, for 8T, 10T, and 12T, the wake size increases noticeably in comparison with the baseline. Again, it should be noted that the increase in the wake size corresponds to a greater momentum loss. By decreasing the wavelength, the momentum loss appears to be greater for the leading-edge tubercles. Figure 62 shows the wake velocity profiles for the second angle of attack, 18 degrees, at a Reynolds number of 201,200 for all models. For this angle of attack in the poststall region, it can be seen that the wake size for 4T, 10T, and 12T remains at almost the same size than the baseline. However, it has increased significantly when compared to the wake observed in Figure 61 possibly due to the flow separation. On the other hand, model 8T shows an increase in the wake size in comparison with the baseline.

Results obtained by integrating the wake velocity profiles are shown in Figure 63. For the different models tested, there were different behaviors observed. Starting with the highest wavelength (4T), the drag coefficient for small angles of attack appears to be lower than that of the baseline, about 10 to 15%. At 10 degrees, the decrease in drag coefficient is about 25% in comparison with the baseline. However, in angles of attack of 12 degrees and higher, the drag coefficient difference with the baseline appears to be negligible.

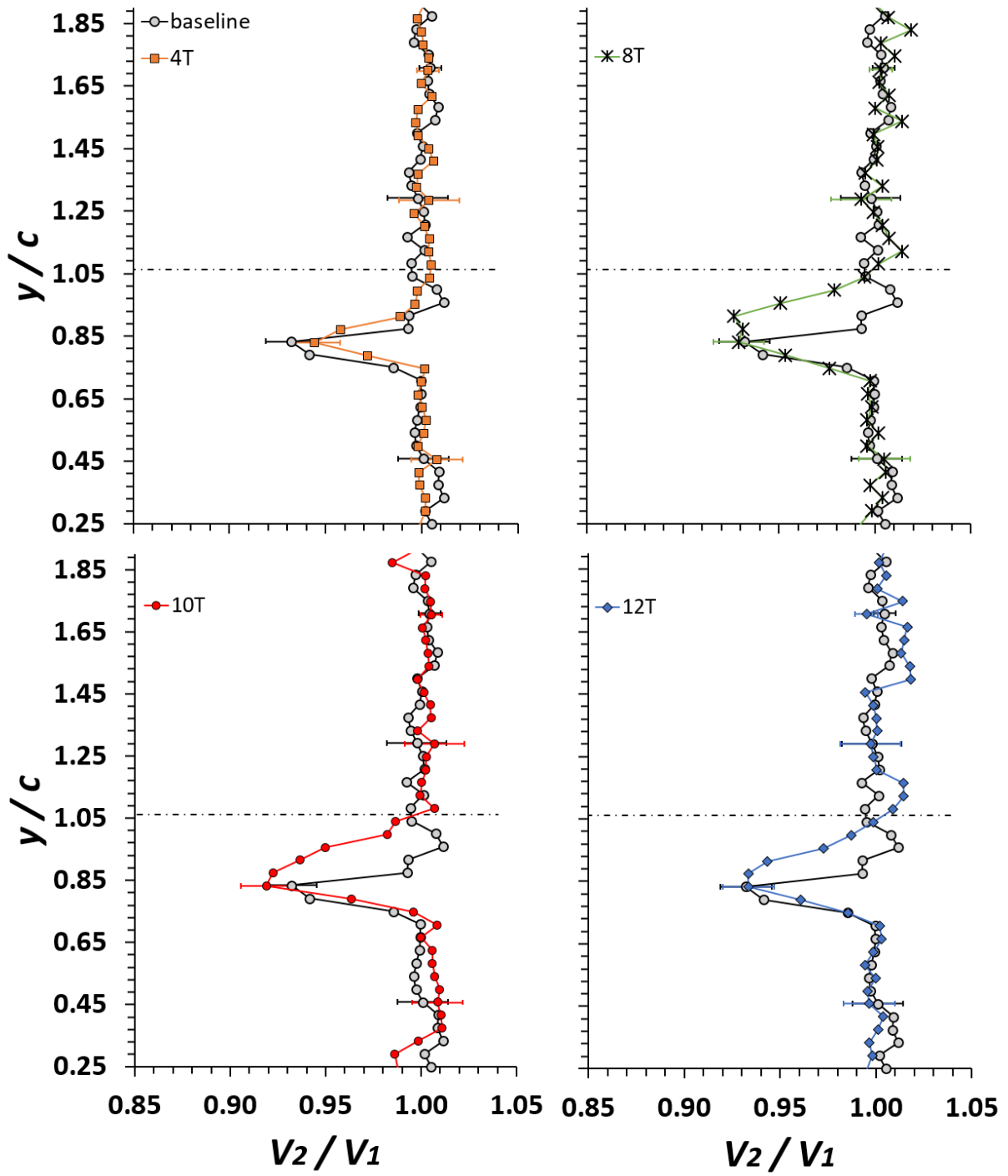


Figure 61. Normalized wake velocity profiles for all models in comparison with the baseline at 10 degrees at a Reynolds number of 201,200

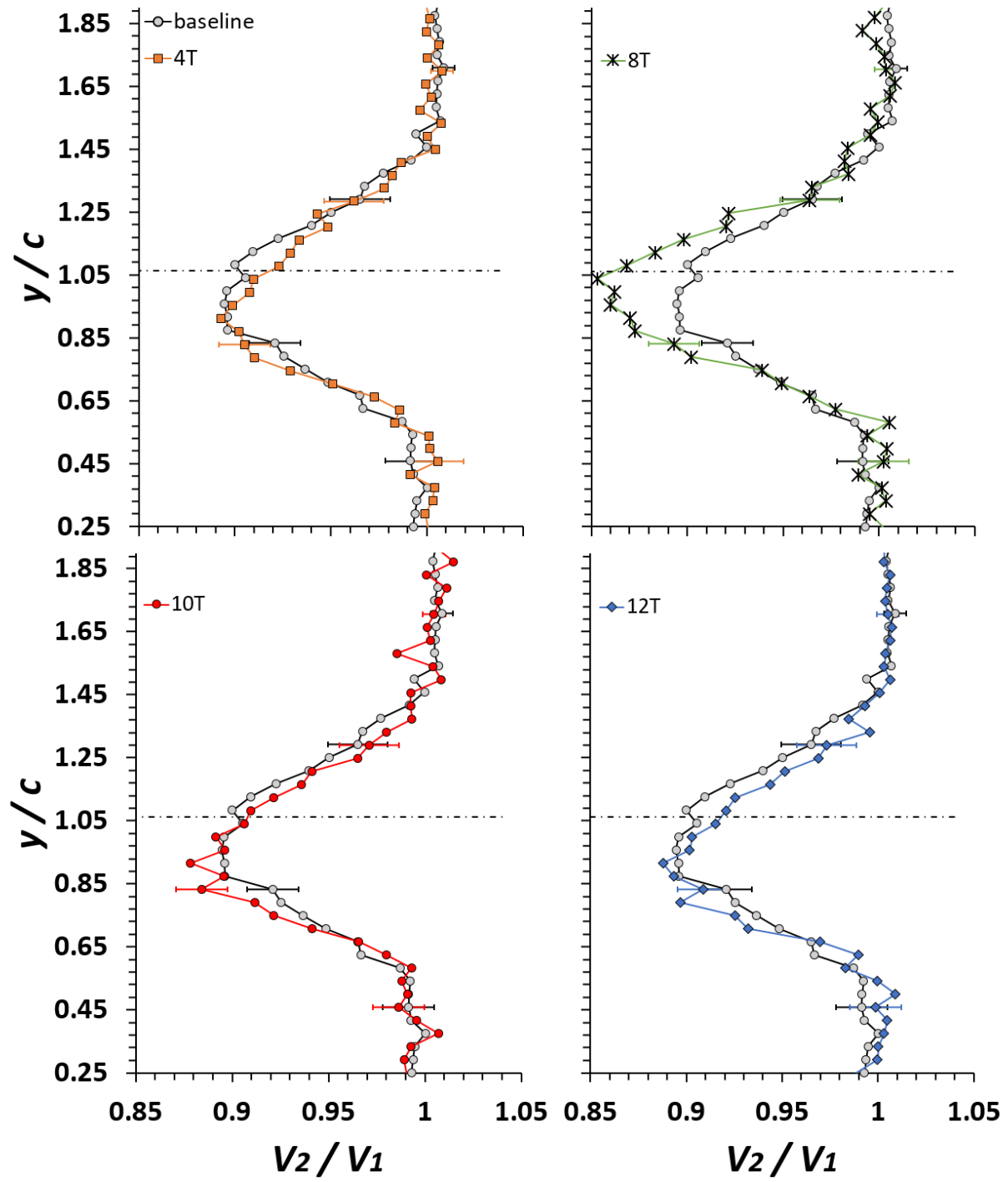


Figure 62. Normalized wake velocity profiles for all models in comparison with the baseline at 18 degrees at a Reynolds number of 201,200

For 8T, the drag coefficient behavior for small angles of attack is similar than that for 4T and the baseline. However, for angles of attack of 10 degrees and higher, the drag coefficient is higher for 8T than the baseline. Models 10T and 12T behave similarly. In smaller angles of attack, the drag coefficient is slightly higher than that of the baseline, 4T, and 8T. The increase in drag coefficient for these models at these angles of attack can reach up to 13 to 55% higher for some cases. However, for angles of attack higher than 14 degrees, the drag coefficient is very similar than that of the baseline and 4T. Among all models tested, 4T appears to be the model that behaves more like the baseline in terms of drag coefficient. For 8T, 10T, and 12T, no evident performance enhancement due to the addition of tubercles at the leading-edge is recorded. On the contrary, for small angles of attack, there seems to be a detrimental behavior in the drag coefficient for 10T and 12T. On the other hand, for higher angles of attack, the detrimental behavior is observed on 8T. The increase in drag in some cases, as it was noted for 8T in previous section, is not a result usually attributed to modified models being studied at lower turbulence intensities.

Figure 64 shows the $C_{D,i}/C_D$ ratio for all models at a Reynolds number of 201,200. It is important to recall that this ratio allows to understand the contribution of the induced drag to the total drag. From the figures, starting by the smallest wavelengths (10T and 12T), it is possible to observe that the influence of the induced drag coefficient is smaller than the baseline for angles of attack ranging from 6 to 12 degrees. The maximum ratio for 10T and 12T decreases about 30%, and it's reached at 10 and 6 degrees, respectively for these two models. In comparison with the baseline, where it's reached at 12. As it appears, for the smallest wavelength, the induced drag coefficient is more influential in the poststall regime. For the wing with the largest wavelength (4T), the induced drag coefficient is very similar than that of the baseline. However,

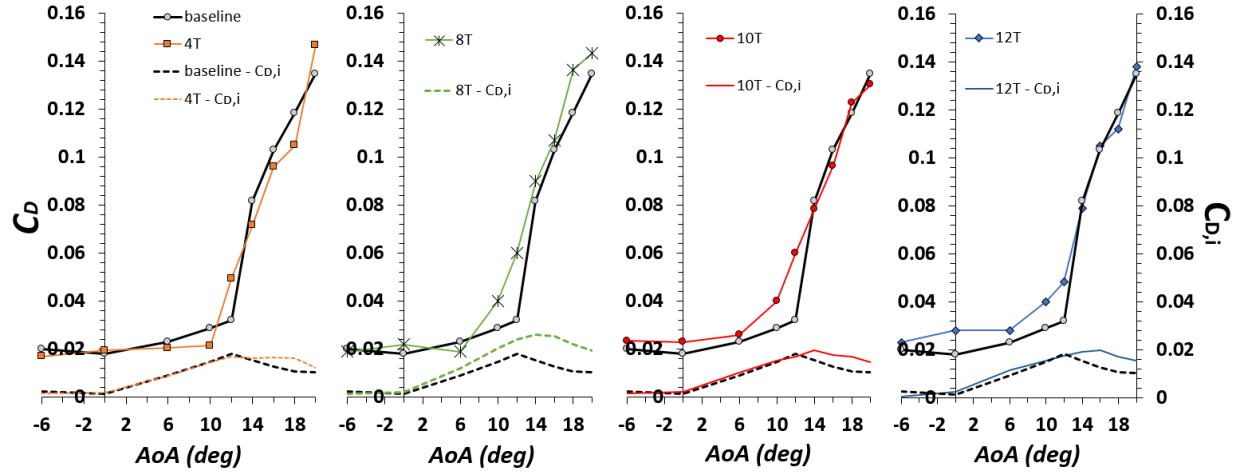


Figure 63. Variation of drag coefficient with angle of attack for all models in comparison with the baseline at a Reynolds number of 201,200

the maximum ratio is increased by almost 20%, and it's reached at significantly lower angle of attack. For angles of attack greater than 12 degrees, the ratio increases for all leading-edge models. From this, it can be expressed that the addition of tubercles increases the induced drag coefficient for high angles of attack in comparison with the baseline. This behavior was pointed out for 8T, which is not in agreement with the results found by Bolzon *et al.* (2016) at low turbulence intensity. However, it can be also observed for all models. An importance difference observed for a higher turbulence intensity.

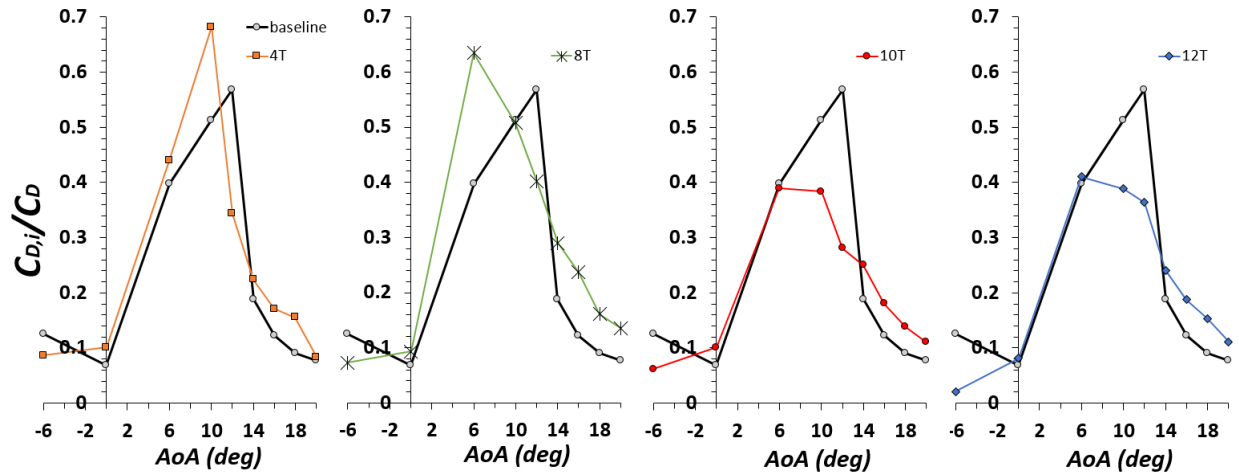


Figure 64. Variation of induced to total drag coefficient ratio with angle of attack for all models in comparison with the baseline at a Reynolds number of 201,200

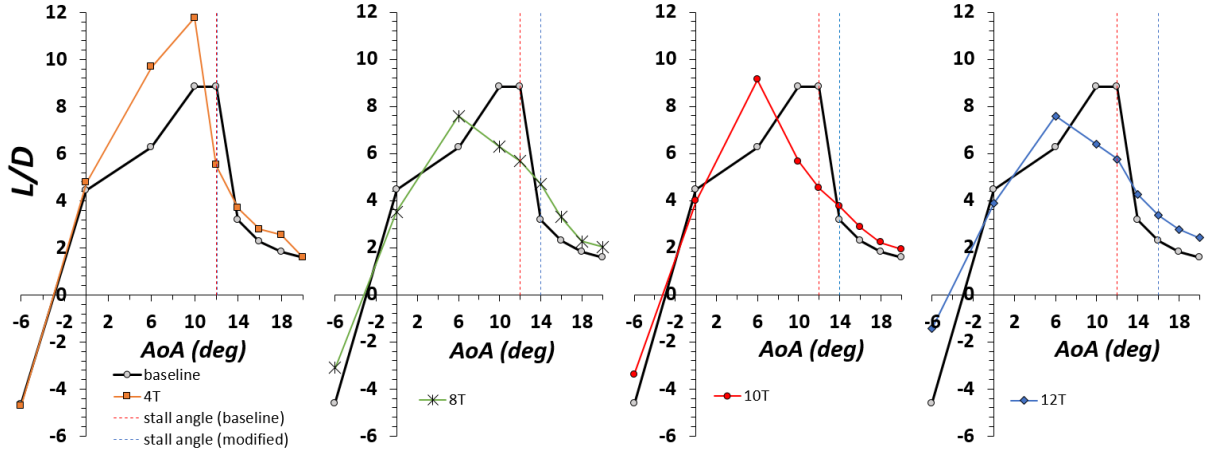


Figure 65. Variation of lift-to-drag ratio with angle of attack for all models in comparison with the baseline at a Reynolds number of 201,200

The L/D is also calculated for all models at a Reynolds number of 201,200, as shown in Figure 65. From this ratio, it is possible to observe the effect of the variation in wavelength in terms of its efficiency. For most models tested, the maximum L/D ratio is decreased or increased however slightly. As shown in Figure 65, the maximum L/D for 4T and 10T increased about 33% and 3%, respectively, in comparison with the baseline. However, for 8T and 12T, the maximum lift-to-drag ratio decreased to approximately 14% for both models. The angle at which the maximum ratio was achieved, however, was decreased by 6 degrees for all cases, with exception of 4T. From Figure 65, as it was noted before, the abrupt loss in lift coefficient is also observed for 4T and the baseline. For models with smaller wavelength, the loss in lift appears to be more gradual, in accordance with the literature. According to these results, the model with the least number of tubercles has the best efficiency when compared to the baseline. However, when looking at the lift coefficient, the performance enhancement is minimal when compared with all other models. For all the models, the L/D increased for higher angles of attack. This behavior observed is very similar to that observed for lower turbulence intensities.

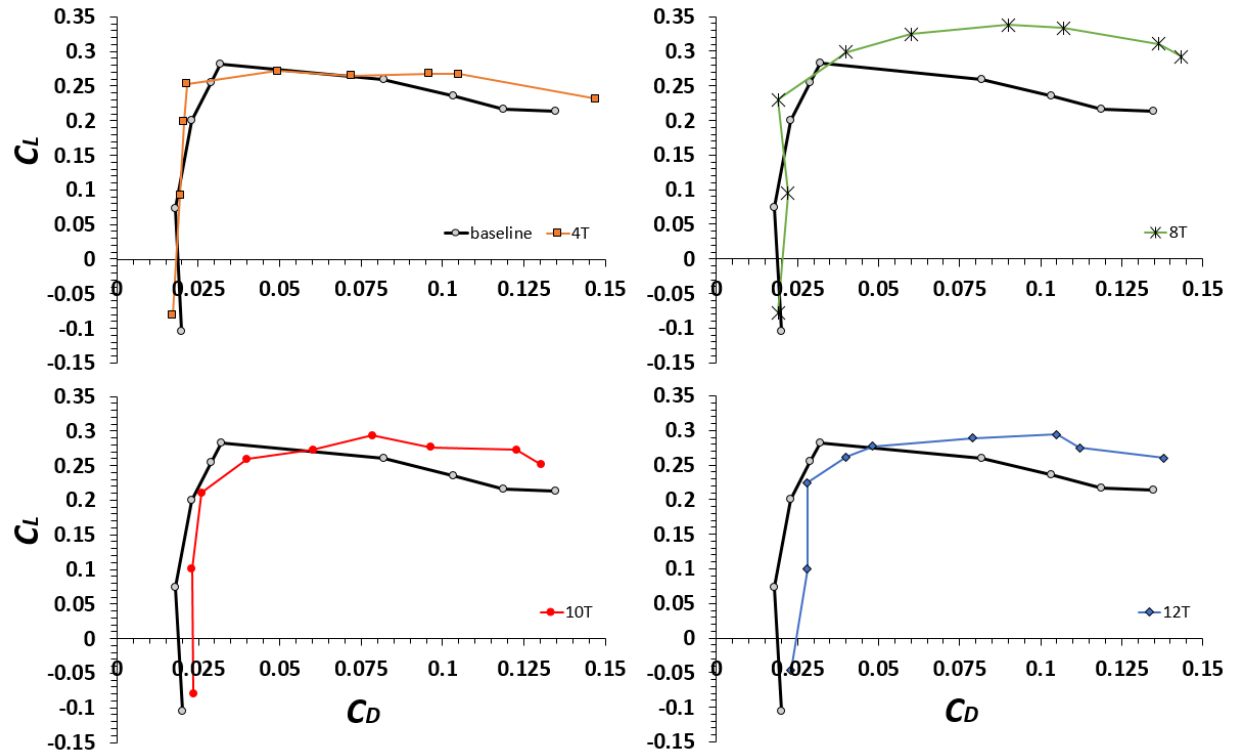


Figure 66. Drag polar for all models at a Reynolds number of 201,200

Figure 66 shows the drag polar for all models at a Reynolds number of 201,200. First, by looking at the zero-lift drag coefficient, 4T showed a similar behavior than 8T. The zero-lift drag coefficient is similar to the baseline. However, when decreasing the wavelength, the zero-lift drag coefficient increases for the modified models 10T and 12T. Another aspect that can be noted from the drag polar is the behavior of the drag coefficient decreasing before increasing with increasing lift coefficient. For all the modified models tested, as it was noted for 8T, this behavior is not observed.

The effect of Reynolds number on the performance of leading-edge tubercles with various configurations is now observed. Selecting 8T, a variation of Reynolds number ranging from 201,200 to 351,600 is studied. Figure 67 presents the results obtained at four different Reynolds numbers, comparing 8T with the baseline. Additionally, data from the literature is included in the cases were possible. The results show that for a Reynolds number of 201,200, as

it was previously mentioned, for small angles of attack, drag coefficient is very similar to that of the baseline. On the other hand, for angles of attack higher than 10 degrees, drag coefficient increases for 8T in comparison with the baseline. Nevertheless, for higher Reynolds number, ranging from 246,100 to 351,600, the drag coefficient exhibits a similar behavior within each other. For angles of attack smaller than 12, the drag coefficient is slightly higher for 8T than for the baseline. For 246,100, 296,200, and 351,600, the drag coefficient increases approximately 56, 54, and 76%, respectively. In comparison with the literature, for higher turbulence intensities, the drag coefficient increased in the prestall with increasing Reynolds number.

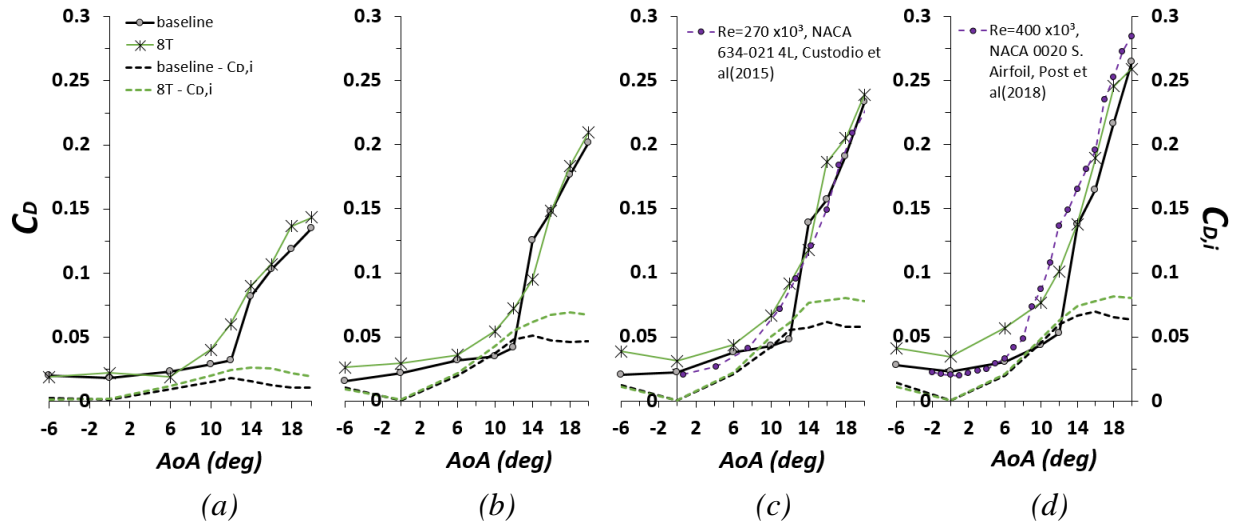


Figure 67. Comparison in the variation of drag coefficient with angle of attack between 8T and the baseline for Reynolds number of (a) 201,200, (b) 246,100, (c) 296,200, and (d) 351,600

Figure 68 shows the minimum drag coefficient. As it can be observed, for these previously discussed Reynolds numbers, the minimum lift coefficient is increased by approximately 50 to 70%, for some specific cases in comparison with the baseline. For angles of attack higher than 12, the drag coefficient difference between 8T and the baseline is negligible for all higher Reynolds number than and including 246,100.

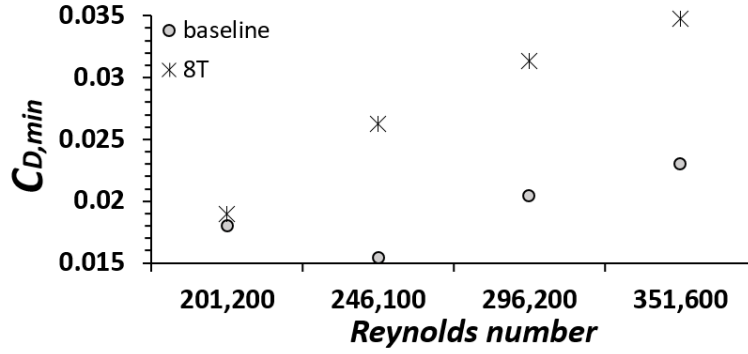


Figure 68. Comparison in the variation of minimum drag coefficient between 8T and the baseline for all Reynolds numbers tested

For all Reynolds numbers tested, L/D ratio is shown in Figure 69. Starting with Reynolds numbers 246,100 and 296,200, the ratio behaves very similar for all angles of attack. The maximum ratio decreases about 27%. For the higher Reynolds number tested, the maximum L/D ratio decreases about 40% for 8T in comparison with the baseline. However, the angle at which this maximum ratio is achieved remains unchanged. For all lower Reynolds number, this angle decreases to 6 degrees. Overall, drag coefficient results for models 8T, 10T and 12T at all Reynolds numbers show that leading-edge tubercles is detrimental for the aerodynamic performance in the prestall regime due to the increase in drag coefficient in comparison with the baseline.

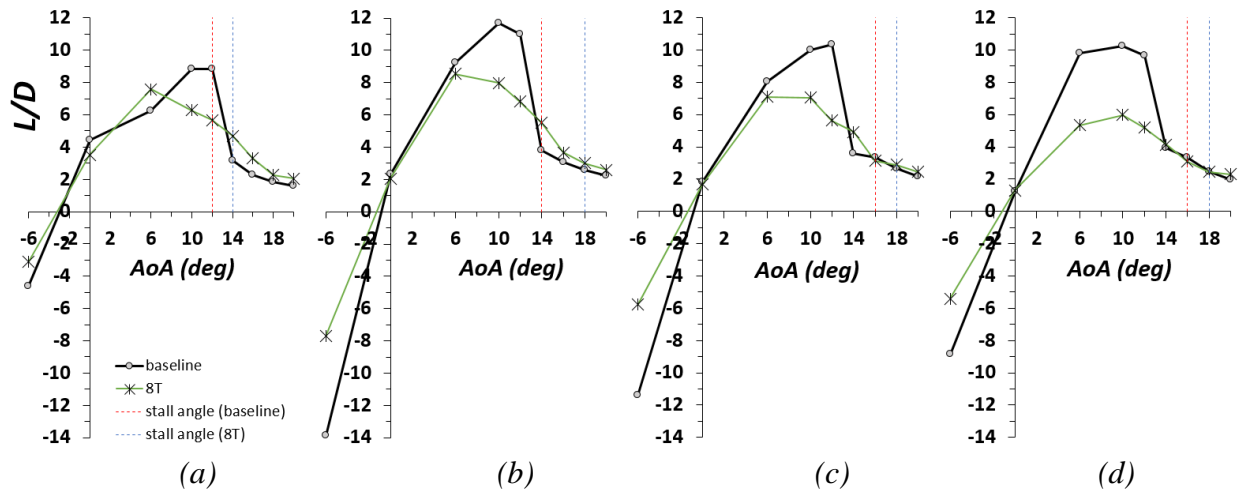


Figure 69. Comparison in the variation of lift-to-drag ratio with angle of attack between 8T and the baseline for Reynolds number of (a)201,200, (b)246,100, (c)296,200, and (d)315,600

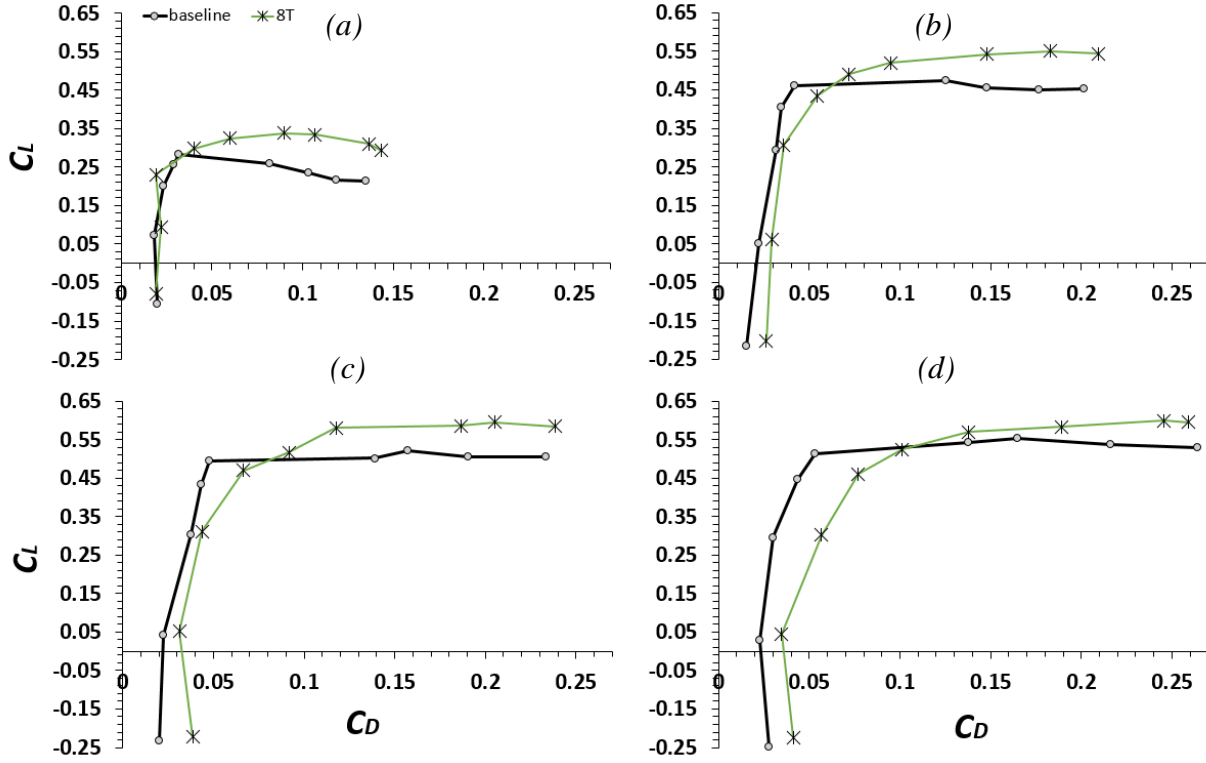


Figure 70. Drag polar comparison between 8T and baseline for Reynolds number of (a) 201,200, (b) 246,100, (c) 296,200, and (d) 315,600

Figure 70 shows the drag polar for all Reynolds number tested. For 8T, at higher Reynolds number, the zero-lift drag coefficient increases for the modified model in comparison with the baseline. Also, the particular behavior observed in all the models with various tubercle configuration is different for the various Reynolds number tested.

Particle Image Velocimetry

With the use of stereoscopic Particle Image Velocimetry, the behavior of the flow can be visualized, the velocity fields can be measured, and turbulent measurements can be performed. At a Reynolds number of 296,200, model 8T is chosen to be compared with the baseline. The following PIV results are chosen at an angle of attack of 18 degrees. This specific angle of attack is within the poststall regime for both models.

Instantaneous PIV Images

Figure 71 shows the instantaneous axial velocity and instantaneous vorticity contours for the baseline and 8T at two different instants, respectively. Each experimental set is composed by 1500 instantaneous velocity fields. As it can be seen in both figures, the instantaneous PIV image varies slightly from one instant to the next. Nevertheless, a similar behavior is present for both instants captured. From the sequence created by the 1500 images, with the known time between images, the spatio-temporal evolution of the velocity and vorticity fields can be obtained.

Time-Averaged Velocity Fields

The mean velocity is calculated by taking the average of the 1500 instantaneous velocity fields. From this, the mean axial and mean transverse velocity contours can be obtained. Figure 72(a) shows the mean axial velocity contours for the baseline and 8T. At the poststall regime, the flow has separated from the surface of the baseline very close to the leading-edge of the model. Flow separation occurs due to the region of adverse pressure gradient in the downstream section of the model, causing the appearance of a large recirculation area for the baseline. For 8T, it can be observed that the flow remains attached up until $x/c = 2$, which is a significant difference when compared to the baseline. Also, the large recirculation area observed for the baseline is noticeably reduced, almost absent for 8T.

Continuing with the velocity fields, Figure 72(b) shows the mean transverse velocity contours for the baseline and 8T. When comparing both models, the baseline shows mostly negative transverse velocities, which confirms the recirculation area observed in the mean axial velocity contour results. For 8T, the transverse velocities are positive for all cases, which similarly confirms that the recirculation area is absent.

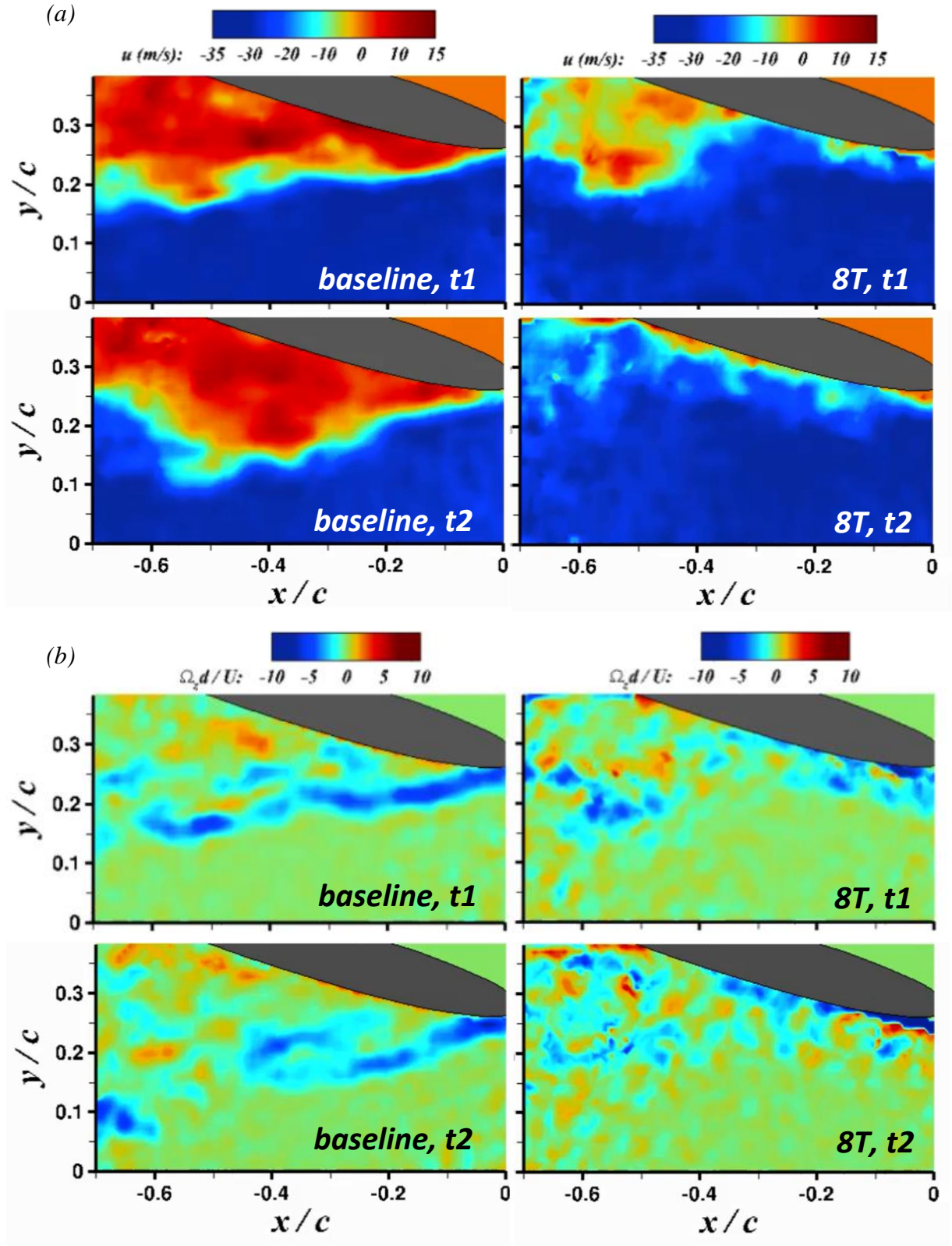


Figure 71. Instantaneous (a)axial velocity and (b)azimuthal vorticity at a Reynolds number of 296,200, 18 degrees angle of attack for the baseline and 8T at two instants

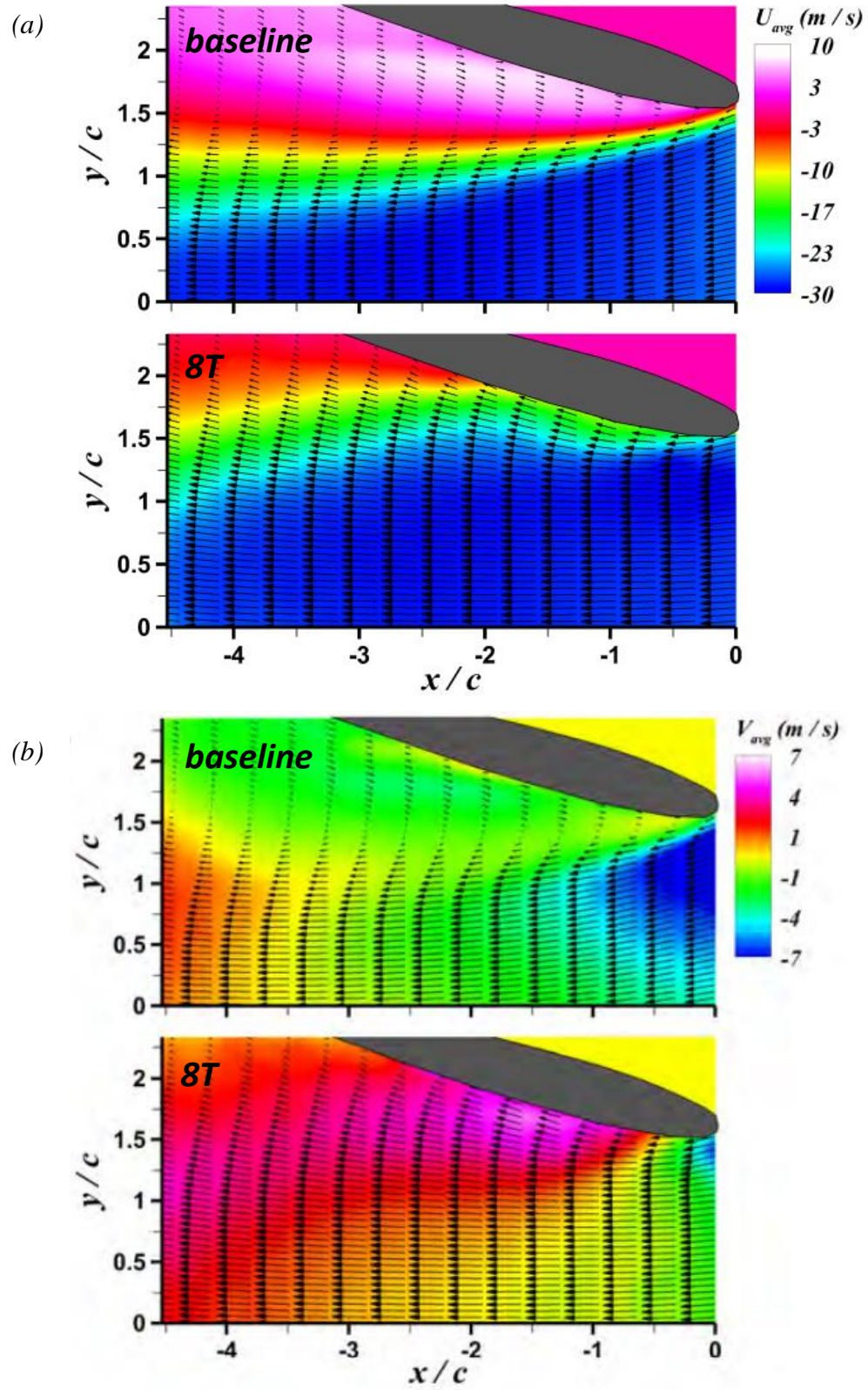


Figure 72. Mean (a)axial and (b)transverse velocity contours at a Reynolds number of 296,200, 18 degrees angle of attack for the baseline and 8T

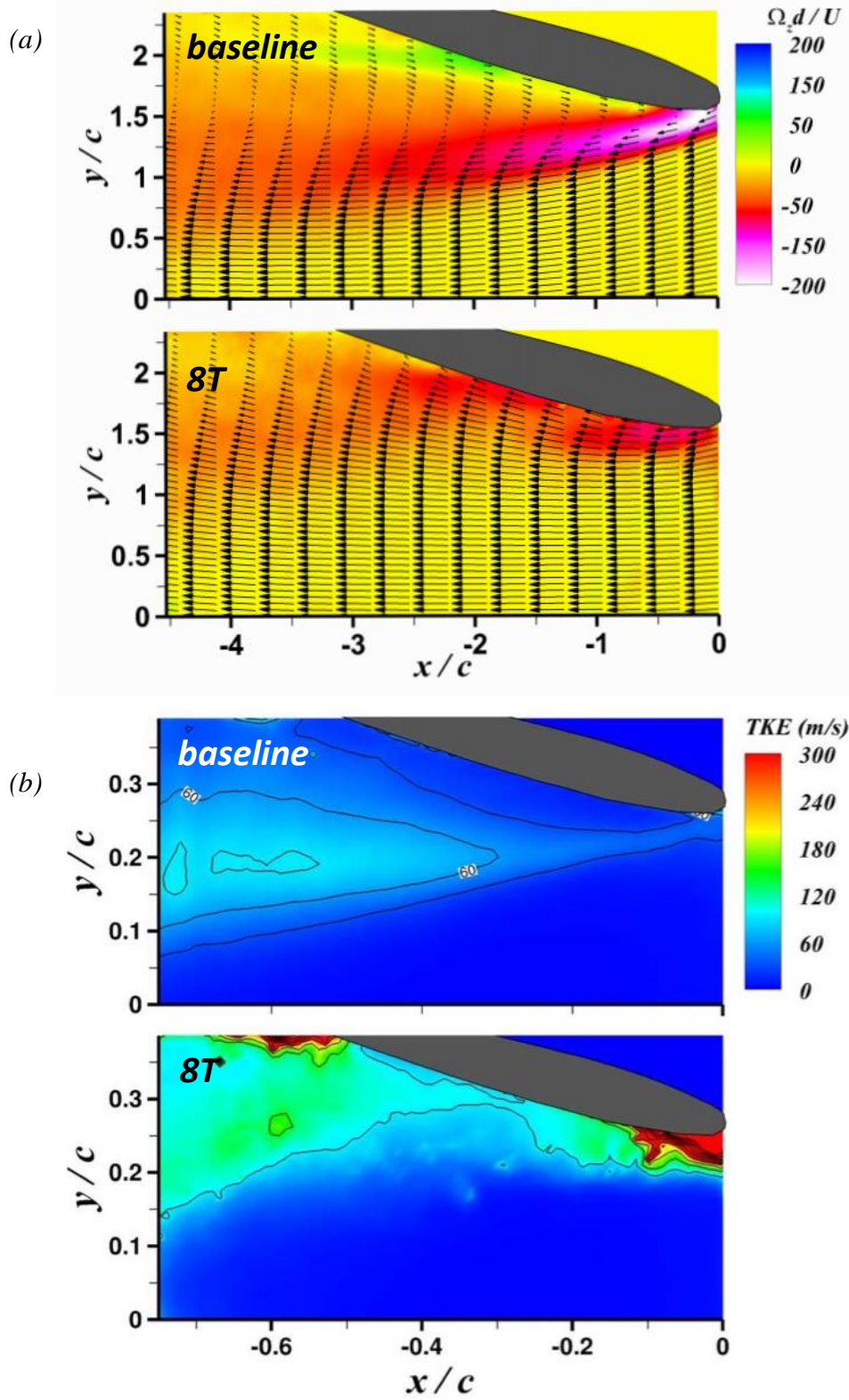


Figure 73. Mean (a)azimuthal vorticity and (b)turbulent kinetic energy contours at a Reynolds number of 296,200, 18 degrees angle of attack for the baseline and 8T

Time-Averaged Vorticity Fields

Figure 73(a) shows the mean vorticity contours for the baseline and 8T. For the baseline, the results show that there's a shedding of vorticity from the leading-edge of the baseline. In comparison with the baseline, 8T shows a concentration of vorticity on the surface of the model up to a distance of $x/c = 2$. In the literature, the presence of streamwise vortices is recorded, which can be directly related to the momentum exchange within the boundary layer and the concentration of vorticity observed. These results can be related to the behavior observed in the velocity fields. The increase of vorticity on the surface of 8T results in the flow separation delay observed for this model.

Turbulence Measurements

Aside from the vorticity fields, the turbulent kinetic energy (TKE) can also be used to explain the behavior observed for the velocity and vorticity fields.

TKE is given by

$$TKE = \frac{1}{2}(u'^2 + v'^2 + w'^2) \quad (81)$$

where u' is axial turbulence intensity, v' is transverse turbulence intensity, and w' is turbulence intensity out-of-plane component of velocity.

Figure 73(b) shows the mean turbulent kinetic energy for the baseline and 8T. For 8T, an indication of the presence of vortices can be observed. The results show a significant amount of turbulent mixing at the leading-edge of the model. On the contrary with the baseline results, where there results for turbulence mixing is not as significant as 8T.

CHAPTER V

CONCLUSION AND FUTURE WORK

Lift Measurements

The aerodynamic characteristics of four models with leading-edge tubercles and a baseline with NACA 0010 underlying profile are studied using force measurements, pressure measurements and flow visualization using PIV. Amplitude is kept constant for all models. Wavelength is varied resulting in 4, 8, 10, and 12 leading-edge tubercles along the spanwise direction. The range of angles of attack studied is -6 to 20 degrees for a range of Reynolds number of 201,200 to 351,600 at a turbulence intensity of 4.3%

In the pre stall, the lift coefficient is very similar for the various models tested with a linear increment in the lift coefficient with angle of attack. The lift curve slope decreases from the theoretical 2π , which is expected. Especially, for finite wings, the generation of trailing vortices due to the pressure gradient at the edges creates a downwash force. Hence, the effective angle of attack experienced by this section is reduced. From this, the lift coefficient experienced by the wing is reduced when compared to airfoils, where only 2D effects are taken into account. For all models, the addition of leading-edge tubercles has marginal effect in the lift coefficient in the pre stall regime.

The stall angle increases for all models, except for the model with the lower number of tubercles. However, for 4T the stall angle remains the same as the baseline, which implies no detrimental performance for the highest wavelength.

In the poststall regime, for all wings, there is performance enhancement observed in various aspects. The lift coefficient increases for all angles of attack for all wings. The maximum lift coefficient increases for all cases, except for 4T. The model with eight tubercles along the spanwise direction exhibits the greater increase in lift coefficient when compared to the baseline. From the literature, the increase in the stall angle and maximum lift coefficient are in common agreement with all studies at lower turbulence intensities. At higher turbulence intensities, the lift measurements also show performance enhancement in the stall and prestall regions.

The optimal number of tubercles (wavelength) cannot be compared to the literature since amplitude is kept constant. For most studies, the optimal wavelength is found by varying the amplitude of the tubercles as well. Furthering this study by varying the tubercle's wavelength can be utilized to examine optimal tubercle configurations for this profile. From the literature, the variation in amplitude is reported to have a greater influence in the performance of various tubercle configurations. However, it is explained that there is no optimal tubercle configuration for all airfoil profiles. The aerodynamic performance seems to be dependent on the airfoil profile. Therefore, these results should be compared to other studies that utilized the NACA 0010 airfoil profile.

Higher turbulence intensities does not seem to affect the behavior of the variation in Reynolds number. There's an increase in the lift curve slope as the Reynolds number increases, the behavior of the modified models is remains very similar as the Reynolds number increases, and $C_{L,max}$ increases as the Reynolds number increases. At lower turbulence intensities, these behaviors have also been noted.

Drag Measurements

From the drag measurement results obtained, all airfoils tested exhibited both a slight enhancement and detrimental effect by the addition of tubercles on the leading-edge based on the total drag and induced drag coefficient. Model 4T had a similar behavior as the baseline, except for small angles of attack where the drag coefficient appears to be lower than that of the baseline. For the airfoil with eight tubercles along the spanwise direction, 8T, the drag coefficient difference is negligible for small angles of attack and is higher in comparison with the baseline for higher angles of attack. Increasing the number of tubercles along the spanwise direction, 10T and 12T, the leading-edge tubercles increase the drag coefficient for small angles in comparison with the baseline.

From the behavior observed with the addition of leading-edge tubercles, it can be concluded that lower number of tubercles (higher wavelength) show performance enhancement up to a certain point. However, for higher number of tubercles (smaller wavelength) the drag generation is greater for all models either in the prestall or poststall regime. These results are in accordance with Hansen *et al.* (2011) and Guerreiro *et al.* (2012), which stated that increasing the wavelength on leading-edge tubercles exhibited a better performance. However, in comparison with results found by Johari *et al.* (2007), the results are not in agreement with those found for this study. Johari *et al.* concluded that a shorter wavelength generates less drag, however minimal (2007). In the literature, the amplitude of the tubercles is also varied. In contrast with the current study, the amplitude is kept constant for all cases. Therefore, to properly assess the effect of tubercle configuration on the drag coefficient, this study should be extended to various amplitudes.

The induced drag, due to the generation of lift, is reported to increase for the leading-edge tubercles, especially for angles of attack in the post stall regime. This is an evident difference caused by the increase of freestream turbulence intensity. At lower turbulence intensity, the induced drag is observed to decreased for higher angles of attack.

By means of the lift-to-drag ratio, it was possible to observe that even though the modified wings have a better performance in terms of lift in the poststall regime, the highest lift-to-drag ratio is experienced by the baseline and 4T. Results obtained for this study are similar than those found by other studies mentioned in the literature review for lower tubulence intensities. From the drag polar, it was possible to observe another difference caused by the increase in the freestream turbulence intensity. The behavior of the drag coefficient with increasing lift coefficient is modified for 8T in comparison with the baseline.

PIV Measurements

PIV measurements, including velocity field, vorticity field and turbulence measurements, allow for a better explanation to the behavior observed for lift and drag measurements. From PIV, in the poststall regime, it can be seen that the addition of leading-edge tubercles creates a generation of streamwise vortices, which in turn increase the vorticity on the surface of the model. As a consequence, the flow remains attached to the surface of the modified model for an extended position downstream. Hence, the recirculation area once seen on the baseline is completely absent on the model with leading-edge tubercles. Consequently, the delay in the flow separation causes the stall angle to increase, increasing lift coefficient in the poststall regime and maximum lift coefficient.

Overall, the addition of tubercles enhances the aerodynamic performance by increasing lift coefficient and stall angle; however, drag coefficient is also increased for the majority of the

cases studied. However, these results are lacking the variation in amplitude in order to perform concluding statements in tubercle configuration and performance. For future work, as it has been mentioned before, the variation of amplitude could play a greater role than that of the wavelength. With these results, a different behavior might be observed for the drag coefficient. Another aspect that should be explored is the utilization of three-dimensional computational methods to understand the behavior of the tubercles such as vortex lattice method. This computational tool can be utilized to discretize a three-dimensional body such as a model with leading-edge protuberances and obtain important parameters such as pressure distribution and lift coefficient.

In regard of flow visualization, for future work, PIV measurements should be obtained for different planes of the models. In the literature, different conclusions have been formulated based on the results observed on the peak-plane and through-plane.

REFERENCES

- Adrian, R. J., & Westerweel, J. (2011). Particle image velocimetry. Cambridge University Press, New York.
- Aftab, S. M. A., Razak, N. A., Mohd Rafi, A. S., & Ahmad, K. A. (2016). Mimicking the humpback whale: An aerodynamic perspective. *Progress in Aerospace Sciences*, 84(2016), 48-69.
- Anderson, J. D. (2011). Fundamentals of aerodynamics, 5th edition. McGraw-Hill, New York.
- Bertin, J. J., & Cummings, R. M. (2014). Aerodynamics for engineers, 6th edition. Pearson, New Jersey.
- Bhushan, B. (2016). Biomimmetics: bioinspired hierarchical-structured surfaces for green science and technology, 2nd edition. Springer International Publishing Switzerland.
- Bolzon, M. D., Kelso, R. M., & Arjomandi, M. (2014). The effects of tubercles on swept wing performance at low angles of attack. Proceedings from 19th Australasian Fluid Mechanics Conference.
- Bolzon, M. D. P., Kelso, R. M., & Arjomandi, M. (2016). Formation of vortices on a tubercled wing, and their effects on drag. *Aerospace Science and Technology*, 56(2016), 46-55.
- Brune, G. W. (1994). Quantitative low-speed wake surveys. *Journal of Aircraft*, 31(2), 249-255.
- Cummings, R. M., Mason, W. H., Morton, S. A., & McDaniel, D. R. (2015). Applied computational aerodynamics. Cambridge University Press, New York.
- Custodio, D., Henoeh, C. W., & Johari, H. (2015). Aerodynamic characteristic of finite span wings with leading-edge protuberances. *AIAA Journal*, 53(7), 1878-1893.
- Erikson, L. L. (1990). Panel methods – An introduction. NASA Technical Paper, California.
- Figliola, R. S., & Beasley, D. E. (2011). Theory and design for mechanical measurements, 5th edition. John Wiley & Sons, New York.
- Fish, F. E., Weber, P. W., Murray, M. M., & Howle, L. E. (2011). The tubercles on humpback whales' flippers: application of bio-inspired technology. *Integrative and Comparative Biology*, 51(1), 203-213.
- Gad-el-Hak, M., Pollard, A., & Bonnet, J. P. (1998). Flow control: fundamentals and practices, 1st edition. Springer-Verlag Berlin Heidelberg, Germany.

- Gleich, A., Pade, C., Petschow, U., & Pissarskoi, E. (2009). Potentials and trends in biomimetics. Springer.
- Guerreiro, J. L. E., & Sousa, J. L. E. (2012). Low-Reynolds-number effects in passive stall control using sinusoidal leading edges. *AIAA Journal*, 50(2), 461-469.
- Hansen, K. L., Kelso, R. M., & Dally, B. B. (2011). Performance variation of leading-edge tubercles for distinct airfoil profiles. *AIAA Journal*, 49(1), 185-194.
- Hansen, K. L. (2012). Effect of leading edge tubercles on airfoil performance. Thesis submitted to School of Mechanical Engineering, The University of Adelaide.
- Helfman Cohen, Y., & Reich, Y. (2016). Biomimetic Design Method for Innovation and Sustainability. Springer International Publishing Switzerland.
- Hess, J. L., & Smith, A. M. O. (1967). Calculation of potential flow about arbitrary bodies. *Progress in Aerospace Sciences*, 8(1967), 1-138.
- Houghton, E. L., Carpenter, P. W., Collicott, S. H., & Valentine, D. T. (2013). Aerodynamics for engineering students, 6th edition. Butterworth-Heinemann.
- Johari, H., Henocho, C., Custodio, D., & Levshin, A. (2007). Effects of leading-edge protuberances on airfoil performance. *AIAA Journal*, 45(11), 2634-2642.
- Katz, J., & Plotkin, A. (2001). Low-speed aerodynamics, 2nd edition. Cambridge University Press, New York.
- Kim, T., Lu, T. J., & Song, S. J. (2016). Application of thermo-fluidic measurement techniques. Butterworth-Heinemann.
- Kim, H., Kim, J., & Choi, H. (2018). Flow structure modifications by leading-edge tubercles on a 3-D wings. *Bioinspiration & Biomimetics*, 13(2018), 1-16.
- Kuethe, A. M., & Chow, C. Y. (1998). Foundations of aerodynamics, 5th edition. John Wiley & Sons, New York.
- Mason, W. H. (2015). Curiosity Number 6. Adventures in Thin Airfoil Theory.
- Méheut, M., & Bailly, D. (2008). Drag-breakdown methods from weak measurements. *AIAA Journal*, 46(4), 847-862.
- Miklosovic, D. S., Murray, M. M., Howle, L. E., & Fish, F. E. (2004). Leading-edge tubercles delay stall on humpback whale (*Megaptera novaeangliae*) flippers. *Physics of Fluids*, 16(5), 39-42.
- Mwenegoha, H. A., & Jabbal, M. (2013) Investigation of passive flow control techniques to enhance the stall characteristics of a microlight aircraft. *International Journal of Flow Control*, 5(3), 215-242.

- Pifer, E. A., & Bramesfeld, G. (2012). Measuring wing profile drag using an integrating wake rake.
- Post, M. L., Decker, R., Sapell, A. R., & Hart, J. S. (2018). Effect of bio-inspired sinusoidal leading-edges on wings. *Aerospace Science and Technology*, 81(2018), 128-140.
- Tropea, C., Yarin, A. L., & Foss, J. F. (2007). Springer handbook of experimental fluid mechanics. Springer-Verlag Berlin Heidelberg.
- van Nierop, E. A., Alben, S., & Brenner, M. P. (2004). How bumps on whale flippers delay stall: an aerodynamic model. *Physical Review Letter*, 100(5), 054502,1-054502-4
- Wei, Z., New, T. H., & Cui, Y. D. (2015). An experimental study on flow separation control of hydrofoils with leading-edge tubercles at low Reynolds number. *Ocean Engineering*, 108, 336-349.
- Yagiz, B., Kandil, O., & Volkan Pehlivanoglu, Y. (2012). Drag minimization using active and passive flow control techniques. *Aerospace Science and Technology*, 17(2012), 21-31.
- Zhang, M. M., Wang, G. F., & Xu, J. Z. (2013). Aerodynamic control of low-Reynolds-number airfoil with leading-edge protuberances. *AIAA Journal*, 51(8), 1960-1971.
- Zhang, M. M., Wang, G. F., & Xu, J. Z. (2014). Experimental study of flow separation control on a low-Re airfoil using leading-edge protuberance method. *Exp. Fluids*, 55(1710), 1-13.

APPENDIX A

APPENDIX A

SOURCE – VORTEX PANEL METHOD

Results for the source-vortex panel method utilized in Chapter II are given by,

```
clear all; close all; clc;
%Alexia Martinez Ibarra
%Spring 2020
%% Parameters
chord=6*0.0254; %m
span=12*0.0254; %m
Vinf=50; %freestream velocity, m/s
rhoinf=1.23; %density, kg/m^3
AoA_d=-6:2:20; %angle of attack, deg
% AoA_r=AoA_d*(pi/180); %angle of attack, rads

%% Airfoil Geometry Generator for NACA 4-digit Series
d1=0;
d2=0;
d3_4=10;
m=d1/100; %Cmax
p=(d2*10)/100; %Xcmax
t=d3_4/100; %tmax

%% Desired Grid Points
N=140; %number of panels
n=(N/2)+1; %half of panels_n lower, half of panels_n upper.
gridpoints=1:n;

%% Non-uniform Panels (cosine spacing)
b=linspace(0,pi,n);
c=0.5*(1-cos(b)); %chord length

%% Mean Camber Line
for i=1:numel(c)
    if c(i)>=0 && c(i)<p
        yc(i)=(m/p^2)*((2*p*c(i))-(c(i))^2);
        dyc_dx(i)=((2*m)/p^2)*(p-c(i));
    elseif c(i)>=p && c(i)<=c(end)
        yc(i)=(m/(1-p)^2)*((1-2*p)+(2*p*c(i))-(c(i))^2);
        dyc_dx(i)=((2*m)/(1-p)^2)*(p-c(i));
    end
end
end
```



```

%% Thickness Distribution
for i=1:numel(c)
    %open trailing edge%
    %yt(i)=(5*t)*(0.2969*sqrt(c(i))-0.1260*c(i)-0.3516*(c(i)^2)...
    %+0.2843*(c(i)^3)-0.1015*(c(i)^4));
    %closed trailing edge
    yt(i)=(5*t)*(0.2969*sqrt(c(i))-0.1260*c(i)-0.3516*(c(i)^2)+...
        0.2843*(c(i)^3)-0.1036*(c(i)^4));
end
tu=yt;
tl=-yt;

%% Airfoil Section - Upper and Lower Surface
for i=1:numel(c)
    theta_yc(i)=atan(dyc_dx(i)); %theta angle, rads
    xu(i)=c(i)-yt(i)*sin(theta_yc(i));
    yu(i)=yc(i)+yt(i)*cos(theta_yc(i));
    xl(i)=c(i)+yt(i)*sin(theta_yc(i));
    yl(i)=yc(i)-yt(i)*cos(theta_yc(i));
end
XL(1)=xl(end); YL(1)=yl(end);
for i=1:numel(xl)-1 %rearrange lower coordinates, TE to LE
    XL(i+1)=xl(end-i);
    YL(i+1)=yl(end-i);
end
XU=xu; YU=yu; %upper coordinates remain, LE to TE
X=[XL';XU(2:end)'];
Y=[YL';YU(2:end)'];

%% Influence Coefficients and Linear Algebraic Equations
for i=1:numel(X)-1
    S(i)=sqrt((X(i+1)-X(i))^2+(Y(i+1)-Y(i))^2); %length of the panel
    line([X(i) X(i+1)], [Y(i) Y(i+1)], 'Color', 'blue', 'LineStyle', '-')
%plotting pannels
    XC(i)=0.5*(X(i)+X(i+1)); %collocation point, x-coordinates
    YC(i)=0.5*(Y(i)+Y(i+1)); %collocation point, y-coordinates
    TJX(i)=(X(i+1)-X(i))/S(i); %unit vector, tangent, x-component
    TJY(i)=(Y(i+1)-Y(i))/S(i); %unit vector, tangent, y-component
    NJX(i)=-(Y(i+1)-Y(i))/S(i); %unit vector, normal, x-component
    NJY(i)=(X(i+1)-X(i))/S(i); %unit vector, normal, y-component
end
figure(1); hold on; grid on; plot(XC,YC,'r. ');
pbaspect([3 1 1]); xlabel('x/c'); ylabel('y/c');

Np1=N+1;
for i=1:N
    Nij(i,Np1)=0;
    Tij(i,Np1)=0;
    for j=1:N
        if i==j
            Nij(i,j)=pi;
            Tij(i,j)=0;
        else
            dx=(XC(j)-XC(i));
            dy=(YC(j)-YC(i));
            XQ=dx*TJX(j) + dy*TJY(j);

```

```

YQ=dx*NJX(j) + dy*NJY(j);
VxQ=-(1/2)*(log((XQ+S(j)/2)^2+YQ^2)-log((XQ-S(j)/2)^2+YQ^2));
VyQ=-(atan2((XQ+S(j)/2),YQ)-atan2((XQ-S(j)/2),YQ));

Nij(i, j)=VxQ*(NJX(i)*TJX(j)+NJY(i)*TJY(j)) + ...
VyQ*(NJX(i)*NJX(j)+NJY(i)*NJY(j)); %Nij sources
Tij(i, j)=VxQ*(TJX(i)*TJX(j)+TJY(i)*TJY(j)) + ...
VyQ*(TJX(i)*NJX(j)+TJY(i)*NJY(j)); %Tij sources
Nij(i,Np1)=VyQ*(NJX(i)*TJX(j)+NJY(i)*TJY(j)) - ...
VxQ*(NJX(i)*NJX(j)+NJY(i)*NJY(j)) + Nij(i,Np1); %Ni,n+1
vortex
Tij(i,Np1)=VyQ*(TJX(i)*TJX(j)+TJY(i)*TJY(j)) - ...
VxQ*(TJX(i)*NJX(j)+TJY(i)*NJY(j)) + Tij(i,Np1); %Ti,n+1
vortex
end
end
end

T=N; Tp1=1;
for j=1:Np1
    Nij(Np1,j)=(Tij(T,j)+Tij(Tp1,j)); %Nij Kutta condition
    Tij(Np1,j)=0; %Tij Kutta condition
end

Tij(Np1,Np1)=pi;

for D=1:numel(AoA_d)
    AoA_r=AoA_d(D)*(pi/180); %angle of attack, rads
    b=[];
    for i=1:N
        b(i)=-Vinf*(cos(AoA_r)*NJX(i)+sin(AoA_r)*NJY(i));
    end
    b(Np1)=-Vinf*(cos(AoA_r)*(TJX(T)+TJX(Tp1)) +
sin(AoA_r)*(TJY(T)+TJY(Tp1)));

    b=b';
    %% Solving System of Linear Algebraic Equations
    a=linsolve(Nij,b);

    %% Finding Tangential Velocity vt
    TJX(N+1) = 0; TJY(N+1) = 0;
    vt=Tij*a + Vinf*(cos(AoA_r)*TJX' + sin(AoA_r)*TJY');

    %% Calculating Cp
    cp=1-(vt/Vinf).^2;

    figure(D+1); hold on; grid on; plot(XC,cp(1:end-1),'k');
    set(gca, 'Ydir', 'reverse'); xlabel('x/c'); ylabel('Cp');
    title('Pressure Coefficient Distribution');

    %% Calculating Circulation \Gamma
    SUM=0;
    for i=1:numel(S)
        SUM=SUM+a(end)*S(i);
    end

```

```

%% Calculating Lift and Lift Coefficient,  $L = \rho_{\infty} V_{\infty} \Gamma$ 
L(D)=Vinf*rhoinf*SUM*span;
Cl(D)=L(D)/(.5*rhoinf*chord*span*Vinf^2);
end

figure(D+2); hold on; grid on; plot(AoA_d,Cl,'r--');
pbaspect([1 1.5 1]); xlabel('Angle of attack, deg'); ylabel('Cl');
title('Effect of Angle of Attack on Lift Coefficient')
xlim([-6 20])

```

APPENDIX B

APPENDIX B

STATE OF THE ART EQUIPMENT AND SOFTWARE

Student Name: Alexia Martinez Ibarra

Thesis Title: Bio-inspired Wings in High Freestream Turbulence: A Numerical and Experimental
Study

Table 4. State-of-the-art equipment

EQUIPMENT	PURPOSE	RESULTS OBTAINED
OMEGA Pressure Transducers	Used to measure change in voltage created by static and total pressure.	Dynamic pressure was calculated in order to calculate velocity using Bernoulli's equation
OMEGA Thermocouple	Used to measure temperature changes in flows	Ambient temperature was measured to obtain experimental density
OMEGA Panel Meters (Displays)	Used to observe any instantaneous changes in pressure/temperature	Amplified signal conditioner for stability
ATI Force Transducer	Used to measure forces and moments acting on the airfoil	Lift and drag forces on modified airfoil were compared to the baseline
Velmex Rotary Table	Used to adjust angle of attack of airfoil	Airfoil was positioned at different angles of attack while running experiments
Velmex Bi-sliders	Used to position pitot rake at desired height behind the airfoil	Pressure was measured at a desired height span to capture the wake behind the airfoil
OMEGA Pressure Scanner	Used to measure pressure for 5 different pitot tubes positioned behind the airfoil	Pressure was measured to capture the wake behind the airfoil
NI Data Acquisition	Used to acquire data from various instrumentations	Results included force, temperature and pressure
LaVision Imager sCMOS Cameras	Used to visualize flow field characteristics by capturing smoke particles in the flow	1500 pairs of images were captured to average the velocity field

Nd: Yag Laser	Used to illuminate smoke particles in the flow field	Flow visualization was captured using CMOs cameras and average velocity field was obtained
Stanford Research Filter	Used to filter pressure transducers response	Noise was eliminated from the signal
Rosco Mini-V Fog Machine	Used to contaminate the purified air with smoke particles in order to visualize the flow field	Flow visualization was captured using CMOs cameras and average velocity field was obtained
Wind Tunnel	Used to test airfoils at different freestream velocities	Lift and drag forces were obtain for several airfoil configurations tested in the wind tunnel

Table 5. State-of-the-art software

SOFTWARE	PURPOSE	RESULTS OBTAINED
NI LABVIEW 2018	Used to acquire, display and save data from several instruments	Results included temperature, force and pressure
MATLAB 2017	Used to process and display data	Results included velocity, Mach, temperature, lift and drag across various experiments
SOLIDWORKS 2018	Used to design and model prototype equipment	Models of set-up and airfoils
MASTERCAM 2017	Used to create tool path to machine specific parts using the CNC	Airfoil, wind tunnel fixtures, instruments fixtures, among other components were machined using the CNC
LaVision DAVIS 8	Used for image processing	Velocity, vorticity and TKE vector fields were obtained
MICROSOFT OFFICE	Used to present results	Results were presented using Microsoft Office suite for the thesis project

BIOGRAPHICAL SKETCH

Alexia Martinez Ibarra was born and raised in Rio Bravo, Tamaulipas, MX on July 27, 1994. In August of 2012, she relocated to Brownsville, TX to pursue her goal of higher education studies at the age of eighteen years old. During her bachelor's career, she started working at the Aerodynamics and Propulsion Laboratory (APL) at the University of Texas Rio Grande Valley (UTRGV) as an undergraduate research assistant due to her interest in the area of fluid dynamics. She completed her studies and obtained her Bachelor of Science in Mechanical Engineering (BSME) from UTRGV in December of 2017. Simultaneously, due to her appreciation for foreign languages, she also obtained a minor in French Language, Literature, and Culture from the same institution. In January of 2018, she decided to continue working towards her master's degree at UTRGV. Ms. Martinez Ibarra continued being a part of the APL research team, now as a graduate research assistant, solidifying her interest in fluid dynamics. During these years, she also worked as a teacher assistant for various undergraduate level courses, such as Numerical Methods, Measurements and Instrumentation, and Manufacturing Processes, extending her interest in academia and research. In May of 2020, Ms. Martinez Ibarra earned her Master of Science in Engineering: Mechanical Engineering from the University of Texas Rio Grande Valley.

Personal email: alexia.mtzibarra@gmail.com